Remote Three-Dimensional Temperature Sensing Using Planar Laser Induced Fluorescence: Development and Applications to Microwave Heated Liquids

by

Timothy M. Finegan

B.S. Physics
The College of William and Mary, 1996

Submitted to the Department of Chemical Engineering in partial fulfillment of the requirements for the degree of

Doctor of Philosophy

at the
Massachusetts Institute of Technology
March, 2004
[June 2004]

Signature of Author: _____
Department of Chemical Engineering
March 8, 2004

Certified by: _____
T. Alan Hatton
Ralph Landau Professor of Chemical Engineering Practice
Thesis Supervisor

Certified by: _____
Paul E. Laibinis
Associate Professor of Chemical Engineering, Rice University
Thesis Supervisor

Accepted by: _____
Daniel Blankschtein
Professor of Chemical Engineering
Chaiman, Committee for Graduate Students

Remote Three-Dimensional Temperature Sensing Using Planar Laser Induced Fluorescence: Development and Applications to Microwave Heated Liquids

by

Timothy M. Finegan

Submitted to the Department of Chemical Engineering on March 8, 2004,
in partial fulfillment of the requirements for the degree of
Doctor of Philosophy in Chemical Engineering

Abstract

Microwave heating is an important technology that has been hampered in application by difficulties in measuring temperatures and temperature distributions during the microwave heating process. This thesis describes the development of a 3D imaging fluorescence thermometry system that was used to examine temporal and spatial variations in temperature within various aqueous solutions during their heating by microwave irradiation. The work provides one of the first experimentally-determined temperature maps for a system undergoing microwave heating.

A 3D thermometry instrument was built based on the principles of Planar Laser Induced Fluorescence (PLIF) imaging. Temperatures were optically determined from ratiometric measurements of the fluorescence from a pair of molecular probes. A Dextran polymer labeled with Rhodamine B was used as a temperature-sensitive probe that operates between 20 and 60 °C. A second temperature-insensitive probe, Rhodamine 110, was used to monitor changes in the laser emission intensity. A dual camera fluorescence detector system was employed to capture a 2D x-y plane at a specified z-axis position. A dichroic mirror and optical filters were used to separate the fluorescence signals from the two probes. The instrument was able to achieve a spatial resolution of 0.2 mm in x-y plane, a 5 mm spatial resolution in z-axis, and a temperature resolution of ±1.6 °C.

The 3D imaging thermometry instrument was modified for investigations into microwave heating. A microwave plasma applicator was adapted for heating experiments with water and salt solutions at concentrations ranging from 0-0.5 M. A viscous solution of 100,000-200,000 MW Dextran at 10% wt was also tested to study microwave heating with reduced convective flows. The dynamics of microwave heating were captured in images with a 0.5 second interval. Microwave heating was observed at node positions in the microwave cavity and varied with the dielectric properties of the heated medium. The experimental results for initial heating were successfully modeled by 2D calculations of the electric field in the microwave cavity. 3D experiments were performed on both pure water sample and on a 0.1 M salt solution. Due to the rapid rate of microwave heating, the 3D experiments were conducted by repeating experiments at different positions in the microwave cavity under the same starting conditions and heating profiles. The simulations of the 2D electric fields in the microwave cavity suggest that the electric field intensity varied little across the z-axis positions. Experiments at different z-axis positions in the cavity had identical profiles within the error of the experiments.

Thesis Supervisor: T. Alan Hatton
Title: Ralph Landau Professor of Chemical Engineering Practice

Thesis Supervisor: Paul E. Laibinis
Title: Associate Professor of Chemical Engineering, Rice University

Acknowledgements

No scientific endeavor prospers in vacuum and though there is only one author in a Ph.D. thesis, this thesis has been the product of many individuals contributing their time and assistance. First, I would like to thank the Lord for the opportunity he has given me to study and work towards a Ph.D. The course of my studies has expanded my horizons and given me a chance to work on understanding a small bit of his creation. I would also like to thank my parents, Michael and Lindy Finegan, for their love and teaching, without which I would never have reached this point in my life.

The road to this Ph.D. thesis has been long and difficult, and at many points seemed doomed to inexplicable problems. I want to thank my thesis advisors, Paul Laibinis and Alan Hatton, who, despite the problems, never gave up hope and always had an encouraging word for me and had the patience to see it through to the end. I also would like to thank my thesis committee members, Bill Green, Klavs Jensen, and Peter So, for lending their time and gracious assistance and help in tackling the many barriers in this work. I would also like to thank Dan Ehrlich for helping me out with a generous loan of optical equipment.

There are many students who contributed time and effort to ensure the success of my thesis. In particular I would like to thank Ji-Jon Sit, Steve Mascaro, and Todd Hastings for their time and assistance in designing the shutter timing electronics. I would like to thank Keith Duggar for many helpful discussions. I would also like to thank my summer intern, Caleb Lo for his work at building the electronics for the cameras and his tireless Matlab programming.

Of course there's the Hatton Group. There isn't another research group on campus which is so fun-loving, helpful, dedicated and honest in their work. I've enjoyed the many years here at MIT, due in no small part to them. There are a few who I would especially like to mention. I want to thank Bain Chin, who was my partner in computer madness and worked with me on the Hatton Group computer systems as well as serving as my sounding board for many years. I also want to acknowledge Geoff Moeser, who always listened and offered helpful suggestions for my research. Finally, I want to thank Lino Gonzalez and Ed Park for letting me borrow their cameras to complete my research.

Then, there is the Graduate Christian Fellowship. My many years at MIT would have seemed long and dark, if not for the friendships and spiritual guidance provided through the fellowship. From the Friday night large group meetings to random gatherings to eat and play games, I have always had fun with the folks at GCF.

Finally, I would like to especially thank my girlfriend, Cynthia Lo, for her wonderful love and kindness towards me. Her support and love from the brightest days of success to the darkest hours of despair have carried me through my time at MIT. I am forever grateful to her for this gift.

Table of Contents

Table of Figures

Chapter 1: Introduction to Microwave Heating

1.1 Introduction

The success of microwave technology is an important development in modern times; our current lifestyle relies heavily each day on its successful application. From the reheated coffee cup in the morning, to cell phones that allow us to connect all over the world, microwaves pervade our lives. As a consumer technology, microwave ovens, in particular, have been enormously successful, penetrating into nearly every American home. Curiously, though, the industrial success of microwave heating technologies has been far more limited, with the majority of industrial microwave heating installations being employed in food processing.[1] The lack of success in deploying microwave heating to the broader chemical industry in particular seems at odds with the commercial success of the microwave oven. Indeed, microwave ovens, in their consumer form, seem to offer advantages of an ideal heat source, able to dispense volumetric heating and provide instant control over a rapidly delivered energy.[2] In the use of this technology, why is there a disparity between the consumer and the chemical industry? The answers lie in the limitations of our understanding of microwave heating; in particular we presently have only a limited knowledge of and ability to measure the temperature distribution within microwave heated samples.[3-5] This question of temperature forms the basis for this thesis: the development of an imaging instrument capable of measuring 2D and 3D temperature fields and their temporal changes within microwave heated systems. While there are a considerable number of simulations which provide theoretical predictions of temperatures in microwave heated targets,[3, 4, 6-16] there is little in the way of experimental verification of their results.

The presence of an applied microwave field adversely affects the use of conventional methods for measuring temperature. Until recently, the measurement of temperature in a microwave field was usually limited to the insertion of fiber optic temperature probes that sampled a bulk temperature via conduction to the probe tip.[5, 17] However, with the development of molecular probes,[18] new methods of temperature sensing became possible as they provide

numerous advantages over macroscopic probes. Molecular probes are molecules that exhibit measurable phenomena, usually a change in optical properties, which can be correlated with temperature and observed remotely without physical connection to the target. Their molecular size not only provides resolution limited only by our ability to discern their thermochromic behavior, but in sufficiently small concentrations, they limit the thermal load of the probe to negligible levels. With careful design, it is possible to use molecular probes to measure 2D and 3D temperature fields and by tailoring their chemical structure, it is possible to make measurements without significantly disturbing the system being measured.

Molecular probes are not limited to applications in temperature measurements. The study of fluid flows and mixing behavior has benefited greatly from the use of such probes as tracers. High resolution imaging of processes such as mixing within a reaction vessel and gas flows in a flame is now possible with molecular probes.[19] In addition, with the development of molecular temperature sensors, information on both fluid flow and temperature could be recovered simultaneously.

1.2 Basics of Microwave Radiation

Microwaves are a subset of the electro-magnetic spectrum spanning frequencies between 100 and 3000 MHz. They have wavelengths from 3 m to 1 mm. Microwave radiation is a very useful band of the EM spectrum and found in many diverse applications such as in communications and heating. Microwave frequencies are used as the carrier signal for the common cell phone as well as satellite radio communication. In both civil and military aviation, microwaves are used for radar. For heating applications, there are two frequency ranges allocated in the US for unlicensed use: 915 MHz (±13 MHz) and 2450 MHz (±50 MHz). These two bands are used for personal electronics, such as phones, wireless computer networking, microwave ovens, and in large-scale industrial heating.

Microwaves radiation is typically generated by magnetrons, which use a heated filament as an electron source and a spiral magnetic field to accelerate the produced electrons. The wavelength of the microwaves generated is determined by the size of the magnetron, with

smaller cavities for shorter wavelengths. For industrial microwave heating, the majority of generators us the 915 MHz frequency range. Magnetrons generate waste heat from their operation and because a 915 MHz magnetron is physically larger than a 2.45 GHz magnetron it has a greater surface area available for cooling, and thus can run at higher power levels. To date, most of the microwave systems for heating applications have focused on food applications and industrial drying of wood and paper.[20] New applications have been proposed in epoxy curing,[21-23] susceptor assisted heating,[24] organic and inorganic synthesis,[20, 25, 26] and ceramic materials processing, including melting, sintering and joining.[12, 14]

1.3 Microwave Heating

Microwaves are electromagnetic waves and consist of a series of oscillating magnetic and electric fields. Microwave radiation heats materials by dielectric polarization. When a polar molecule is acted on by an electric field, the molecule's dipole will align along the direction of the applied electric field. However, in an oscillating field, the electric field lines reverse direction, and the molecule must rotate to maintain its alignment with the field. If the oscillation is slow, the dipole will follow the changes in the field, but if the oscillation is extremely fast, the molecule will not have sufficient time to respond to the field changes and will not be able to follow the changes in the field. However, if the oscillation frequency is in the range of the dipolar response time, dielectric heating can occur. In this case, the molecule attempts to align with the field, but, because the field oscillation is faster than the response time of the molecule, the molecule will lag behind the field direction. Since the molecule cannot dissipate the energy from the force that causes it to align with the field, the molecule must absorb the energy and consequently heat up.[17, 27] The susceptibility of a material to dielectric polarization is dependent on the dielectric properties of the material as given by the dielectric constant, which is a complex number written as:

$$\varepsilon^* = \varepsilon' + i\varepsilon'' \qquad (1\text{-}1)$$

The real part of the dielectric constant (ε') is what is often tabulated as the (static) dielectric constant of a material. The imaginary term (ε'') is referred to as the dielectric loss and represents the energy loss through dielectric heating.[20]

1.4 Challenges in Application of Microwave Heating

There are two major barriers to the broader use of microwave heating, the difficulty of achieving uniform heating and the vastly different rates at which different materials absorb microwave radiation. Dielectric heating depends on dipolar rotation and the efficiency of conversion of electromagnetic energy depends on the dielectric loss of the molecule. The higher its dielectric loss term, the more efficient a material is at converting electromagnetic energy to heat; such materials are referred to as "lossy" materials. Water is a good example of a lossy material, and because of the high proportion of water in foods, microwaves have been readily applied to cooking food and food processing. Unfortunately, many chemical reactions do not include a suitable polar target for microwave absorption. One solution to this problem has been to introduce a species to the mixture that absorbs microwave energy to increase the overall microwave absorption. The added species then transfers the heat via conduction to the reacting mixture. This technique has been demonstrated with ionic liquids[24], vermiculite beads[28] and magnetic nanoparticles.[29]

The problem of uniform heating by microwave radiation is best separated into two coupled conditions: The interaction of the microwave with materials containing components with differing dielectric constants and the interaction of the microwave with the enclosure. One metric of the interaction of microwaves with a material is the penetration depth, which is defined as the distance over which the incident electric field drops to 1/e of its initial value.[1] For a semi-infinite material with the electric field given by:

$$E = E_0 e^{-\beta z} \tag{1-2}$$

the penetration distance β^{-1} is given by [20]:

$$\beta = \frac{\omega}{c}\sqrt{\frac{1}{2}\varepsilon'\left(\sqrt{1+\tan^2\delta}-1\right)} \tag{1-3}$$

where ω is the angular frequency, c is the speed of light, ε' is the static dielectric constant and tan δ is defined as:

$$\tan\delta = \frac{\varepsilon''}{\varepsilon'} \tag{1-4}$$

The equations show that the microwave radiation's penetration into a material depends on both frequency of the microwave radiation and the dielectric properties of the material.

Although microwave heating is a volumetric heating process, its spatial distribution of energy is not uniform. As a further complication, the dielectric properties of a material change with temperature, causing the heating profile of a dielectric material to vary over time, such a change can lead to "runaway" effects in materials when dielectric losses increase with temperature.[20] The problems of dielectric property change are further complicated by phase changes. One readily accessible example is the thawing of frozen food in a home microwave oven. If the food is simply heated by the microwaves with continuous power, the edges of the food will thaw and cook, while the center will remain frozen. This behavior is caused by the differences in the dielectric properties of ice and liquid water and in the penetration depth of microwaves in the food. Initially, ice, which has a low dielectric loss, dominates the heated food item and microwaves penetrate throughout it. However, because the field at the outer surfaces is stronger, the outer surfaces absorb more energy and begin to melt first. The generated liquid water in these regions has a higher dielectric constant, causing the outer sections to absorb microwaves more efficiently than the icy interior regions. The outer regions begin to cook while acting to shield the interior regions from the applied microwave radiation. To reduce this phenomenon, most domestic microwaves are equipped with a "thaw" mode that pulses the microwave field in set intervals, allowing time for conduction to distribute the energy throughout the food. The design of microwave cavities for uniform heating is complex task where the target geometry and its dielectric properties as well as the microwave frequency must be considered. Alternatively, a balance of conduction times relative to pulse power and frequency of the microwave source must be made to ensure uniform heating.

Alterations to the microwave field are not only caused by changes in the dielectric properties of the heated material, but the walls of the enclosure as well. The enclosure that holds the target material for microwave heating is called an applicator or a microwave cavity. In order to increase the efficiency of microwave heating, this cavity is usually designed as a resonant cavity, in which microwaves are reflected and pass through the target material multiple times.

With careful design, a resonant cavity can provide a particular EM field distribution in order to achieve a specific heating profile. The design of an efficient applicator is coupled with the specific dielectric properties of the target because both the design and material affect the EM field distribution. Although the spatial distribution of the EM field can be readily computed by solving Maxwell's equations, the coupled problem is much more difficult. Many attempts have been made to generate numerical solutions to this problem;[3, 6-11, 13-16, 20, 30, 31] however, experimental verifications are limited.[2, 4, 5, 17, 32, 33] The paucity of experimental data stems from the incompatibility of common instruments for temperature measurement with an electromagnetic field and the single point (or 1D) nature of these instruments. Thermocouples have been used to measure temperatures on samples directly after heating;[5 17] however, this approach does not capture the dynamics of the microwave heating process. Optical analogues to traditional thermocouples that measure temperature with fiber optics probes have been developed and used in microwave temperature measurements,[2, 4] but these approaches are still limited by to measurements at single points. 2D measurements have been made using infrared cameras in microwave systems;[2, 32] however, infrared cameras only provide information on heating profiles near a surface. To comprehensively explore microwave heating effects, a temperature measurement system that can measure internal temperatures of a dielectric material in three dimensions is needed.

This thesis details the development of a fluorescence-based thermometry instrument to measure temperature in a material that is being heated by microwave radiation. Chapter 2 discusses various optical methods for temperature measurement and describes the criteria for the selecting the fluorescent temperature sensors employed. Chapter 3 focuses on the design of a multidimensional imaging thermometry instrument and several of the key obstacles that were overcome in the development. In chapter 4 I discuss a set of experiments that were designed to verify the operation of the instrument and test its spatial and temperature resolution. Chapter 5 presents experimental work using the imaging thermometry instrument to measure dynamic temperature profiles of a microwave heated material. Finally, the results of 2D simulations of the electric field in the microwave cavity and sample are presented and their correlation to the experimental results is discussed.

References:

1. Lou, J., *Microwave-Assisted Chemical Processing: I. Modulation of Dielectric Absorption in Organic Media, Ii. Photophysical Behavior of Bipyrenyl Fluorescent Probes*, in *Department of Chemical Engineering*. 1998, Massachusetts Institute of Technology: Cambridge.Ph.D Thesis p. 213.
2. Ratanadecho, P., K. Aoki, and M. Akahori, *A Numerical and Experimental Investigation of the Modeling of Microwave Heating for Liquid Layers Using a Rectangular Wave Guide (Effects of Natural Convection and Dielectric Properties)*. Applied Mathematical Modelling, 2002. **26**(3): p. 449-472.
3. Jia, X. and P. Jolly, *Simulation of Microwave Field and Power Distribution in a Cavity by a 3-Dimensional Finite-Element Method*. Journal of Microwave Power and Electromagnetic Energy, 1992. **27**(1): p. 11-22.
4. Zhao, H. and I.W. Turner, *The Use of a Coupled Computational Model for Studying the Microwave Heating of Wood*. Applied Mathematical Modelling, 2000. **24**(3): p. 183-197.
5. Jia, X., *Experimental and Numerical Study of Microwave-Power Distributions in a Microwave-Heating Applicator*. Journal of Microwave Power and Electromagnetic Energy, 1993. **28**(1): p. 25-31.
6. Ayappa, K.G., H.T. Davis, E.A. Davis, and J. Gordon, *Two-Dimensional Finite Element Analysis of Microwave Heating*. AIChE Journal, 1992. **38**(10): p. 1577-1592.
7. Ayappa, K.G., S. Brandon, J.J. Derby, H.T. Davis, and E.A. Davis, *Microwave Driven Convection in a Square Cavity*. AIChE Journal, 1994. **40**(7): p. 1268-1272.
8. Ayappa, K.G. and H.T. Davis, *Resonant Microwave Power Absorption in Slabs and Cylinders*. AIChE Journal, 1997. **43**(3): p. 615-624.
9. Basak, T. and A.G. Ayappa, *Analysis of Microwave Thawing of Slabs with Effective Heat Capacity Method*. AIChE Journal, 1997. **43**(7): p. 1662-1674.
10. Basak, T. and K.G. Ayappa, *Influence of Internal Convection During Microwave Thawing of Cylinders*. AIChE Journal, 2001. **47**(4): p. 835-850.
11. Basak, T. and K.G. Ayappa, *Role of Length Scales on Microwave Thawing Dynamics in 2d Cylinders*. International Journal of Heat and Mass Transfer, 2002. **45**(23): p. 4543-4559.
12. Chatterjee, A., T. Basak, and K.G. Ayappa, *Analysis of Microwave Sintering of Ceramics*. Aiche Journal, 1998. **44**(10): p. 2302-2311.
13. Harms, P.H., Y. Chen, R. Mittra, and Y. Shimony, *Numerical Modeling of Microwave Heating Systems*. Journal of Microwave Power and Electromagnetic Energy, 1996. **31**(2): p. 114-121.
14. Hill, J.M. and T.R. Marchant, *Modelling Microwave Heating*. Applied Mathematical Modelling, 1996. **20**(1): p. 3-15.
15. Zhao, H. and I.W. Turner, *An Analysis of the Finite-Difference Time-Domain Method for Modeling the Microwave Heating of Dielectric Materials within a Three-Dimensional Cavity System*. Journal of Microwave Power and Electromagnetic Energy, 1996. **31**(4): p. 199-214.
16. Liu, F., I. Turner, and M. Bialkowski, *A Finite-Difference Time-Domain Simulation of Power-Density Distribution in a Dielectric-Loaded Microwave Cavity*. Journal of Microwave Power and Electromagnetic Energy, 1994. **29**(3): p. 138-148.

17. Wei, C.K., H.T. Davis, E.A. Davis, and J. Gordon, *Heat and Mass Transfer in Water-Laden Sandstone: Microwave Heating.* AIChE Journal, 1985. **31**(5): p. 842-848.
18. Childs, P.R.N., J.R. Greenwood, and C.A. Long, *Review of Temperature Measurement.* Review of Scientific Instruments, 2000. **71**(8): p. 2959-2978.
19. Hanson, R.K., *Planar Laser-Induced Fluorescence.* Journal of Quantum Spectroscopic Radiation Transfer, 1988. **40**(3): p. 343-362.
20. Ayappa, K.G., *Modelling Transport Processes During Microwave Heating: A Review.* Reviews in Chemical Engineering, 1997. **13**(2): p. 1-69.
21. Wei, J., M.C. Hawley, and J.D. Delong, *Comparison of Microwave and Thermal Cure of Epoxy Resins.* Polymer Engineering and Science, 1993. **33**(17): p. 1132-1140.
22. Wei, J., M.C. Hawley, and M.T. Demeuse, *Kinetics Modeling and Time-Temperature-Transformation Diagram of Microwave and Thermal Cure of Epoxy Resins.* Polymer Engineering and Science, 1995. **35**(6): p. 461-470.
23. Finzel, M.C., M.C. Hawley, and J. Jow, *Dielectric Properties of a Curing Epoxy/Amine System at Microwave Frequencies.* Polymer Engineering and Science, 1991. **31**(16): p. 1240-1244.
24. Leadbeater, N.E. and H.M. Torenius, *A Study of the Ionic Liquid Mediated Microwave Heating of Organic Solvents.* Journal of Organic Chemistry, 2002. **67**(9): p. 3145-3148.
25. Monsef-Mirzai, P., W.R. McWhinnie, M.C. Perry, and P. Burchill, *Reaction of Phosphorylating Reagents with Substituted Phenols and Coals, Using Microwave Heating.* Fuel, 1995. **74**(7): p. 1004-1008.
26. Majetich, G. and R. Hicks, *The Use of Microwave Heating to Promote Organic Reactions.* Journal of Microwave Power and Electromagnetic Energy, 1995. **30**(1): p. 27-45.
27. Stuerga, D.A.C. and P. Gaillard, *Microwave Athermal Effects in Chemistry: A Myth's Autopsy .1. Historical Background and Fundamentals of Wave-Matter Interaction.* Journal of Microwave Power and Electromagnetic Energy, 1996. **31**(2): p. 87-100.
28. Spinella, A., T. Fortunati, and A. Soriente, *Microwave Accelerated Wittig Reactions of Stabilized Phosphorus Ylides with Ketones under Solvent-Free Conditions.* Synthesis Letters, 1997. **1**: p. 93-94.
29. Holzwarth, A., J. Lou, T.A. Hatton, and P.E. Laibinis, *Enhanced Microwave Heating of Nonpolar Solvents by Dispersed Magnetic Nanoparticles.* Industrial & Engineering Chemistry Research, 1998. **37**(7): p. 2701-2706.
30. Kajfez, D., S. Chebolu, A.A. Kishk, and M.R. Abdul-Gaffoor, *Temperature Dependence of Composite Microwave Cavities.* IEEE Transactions on Microwave Theory and Techniques, 2001. **49**(1): p. 80-85.
31. Hirata, A., S. Matsuyama, and T. Shiozawa, *Temperature Rises in the Human Eye Exposed to Em Waves in the Frequency Range 0.6-6 Ghz.* IEEE Transactions on Electromagnetic Compatibility, 2000. **42**(4): p. 386-393.
32. Dibben, D.C. and A.C. Metaxas, *Finite Element Time Domain Analysis of Multimode Applicators Using Edge Elements.* Journal of Microwave Power and Electromagnetic Energy, 1994. **29**(4): p. 242-251.
33. Rattanadecho, P., K. Aoki, and M. Akahori, *Experimental Validation of a Combined Electromagnetic and Thermal Model for a Microwave Heating of Multi-Layered Materials Using a Rectangular Wave Guide.* Journal of Heat Transfer-Transactions of the ASME, 2002. **124**(5): p. 992-996.

Chapter 2: Introduction to Optical Temperature Measurement

2.1 Introduction

Temperature is one of the most important parameters of experimental systems, and its accurate measurement is of paramount concern. Childs, in a review article on thermometry, describes no fewer than 22 different methods of temperature measurement[1], a clear indication of the large amount of work in temperature measurement and its importance. The rising importance of small length scales in modern technology has prompted the development of microscale methods of temperature measurement. Of the many methods of microscale temperature measurement, the development of molecular probes shows particular promise as a solution for measuring temperatures in a microwave heated system. Temperatures in microwave heated systems are difficult to measure because of a combination of volumetric heating and an electromagnetic field that is disturbed by and disrupts traditional contact methods. Molecular probes present many advantages as a solution to the problem of temperature measurement in a microwave heated sample. Molecular probes can be observed remotely, avoiding disruption of the microwave electromagnetic field, and can operate in an electromagnetic field. Modern detector technology allows us to use molecular probes at very low concentrations, limiting their chemical effect on the system. Due to their small size, molecular probes react almost instantaneously to changes in temperature and unlike microscale contact thermometers, such as thermocouples, molecular probes present virtually no thermal load on the system. Thermometry by molecular probes is also readily scalable from macroscale to microscale. Finally, with the proper instrument design molecular probes can be used to measure temperature in two or even three dimensions. This chapter provides a broad overview of temperature measurement strategies and their limitations in applications to microwave systems. The specific class of fluorescent molecular temperature probes is discussed in detail along with the specifics behind the choice of Rhodamine B and Rhodamine 110 as a ratiometric temperature probe pair. The mathematical processing of ratiometric fluorescence data is developed along with the background on the major methods of exciting and detecting fluorescence.

2.2 Temperature Measurement

There are many methods of measuring temperature and they can be classified into two broad categories: direct contact measurements, and remote measurements.[1] It is helpful to break down the remote methods into two sub-categories: those that require a temperature sensitive material and those that take advantage of properties of the system. The direct contact category contains familiar methods, such as mercury or alcohol thermometers, thermocouples, and liquid crystal temperature strips. The remote methods contain a mixture of standard methods, such as infrared temperature measurements, and more exotic methods such as Raman scattering and temperature sensitive molecular probes.[1]

The first category, direct contact, is also the most common method of temperature measurement, often taking the form of a mercury thermometer or thermocouple. These devices are simple to use and have relatively low cost, but they suffer the disadvantage of requiring direct physical contact with the target for operation. Because these probes work by bulk conduction and convection, their response time to changes in temperature is slow. Smaller probes can reduce this response time (but only to the millisecond range) and they can disturb the thermal state of the system due to their size.[2] In addition, these probes are limited because they sample only a single point, and furthermore, in specific environments, such as in the presence of electromagnetic fields, thermocouples cannot be used. Optical thermometers have been developed to address some of the limitations of thermocouples.[1, 3] The optical thermometer is composed of two components, a probe tipped with a temperature sensitive fluorescent material sealed within a protective coating and an optical fiber to carry the excitation light to the probe and emission light from the probe. These optical probes are compatible with electromagnetic fields and have been used successfully in microwave heated samples.[4, 5] However, these probes suffer physical limitations similar to thermocouples: they act as a thermal load to the system, have a slow response time because of conduction, and sample only a single point. These problems limit the usefulness of optical thermometers for understanding the volumetric heating of microwaves.

The second category of remote measurement includes the most commonly used two dimensional temperature system: infrared cameras. The natural emission of infrared radiation can be correlated with the temperature of the body that emitted the radiation.[1] Infrared cameras have also been used to explore microwave heating[5, 6] However, infrared measurements suffer from some important limitations. For objects opaque to infrared radiation, the infrared emissions originate from the surface and are an accurate reflection of the surface temperature. However, in a material that is transparent or partially transparent to infrared radiation, some proportion of the infrared emission detected originates from within the sample, rather than the surface. The mixing of the origin of the radiation reduces the accuracy of the spatial temperature measurement. Infrared wavelengths are longer than visible wavelengths and their spatial resolution is reduced compared to visible light methods by the diffraction limit[2]. Infrared methods do provide numerous advantages over thermocouples, with 2D measurements that are noninvasive and can be made quickly.

Several remote methods take advantage of the spectroscopic properties of molecular probes. By using molecular scale probes, these techniques have a scaling flexibility in both time and spatial dimensions; however, they are complex and expensive techniques that require systems specifically tailored to ensure a good measurement. Generally, spectroscopic techniques rely on fluorescence, but scattering techniques have also been demonstrated to measure temperature.[1] In fluorescence thermometry, molecular probes can be attached as thin films to target systems for surface temperature measurements of solids, or as agents included in solution for spatial temperature measurements in liquid systems.[1, 3] These molecular probes offer many advantages over conventional approaches for temperature measurement. Molecular probes sample their microscopic environment directly, and thus report a local temperature instead of a bulk average temperature. Temperature measurements accurate to 0.01° C have been reported with fluorescent thin films.[7] Also, because of the microscopic nature of the probes, their spatial resolution is far greater than is possible for systems relying on macroscopic physical contact. Many probes have fluorescence output in the visible region, thereby increasing the spatial resolution compared to infrared methods because of a smaller diffraction limit. Spatial resolutions as high as 0.7 μm have been reported[8] and these length scales allow fluorescent probes to be used in examinations of microscopic systems (i.e. semiconductor devices) and

biological systems (i.e. cells).[9] High speed temperature measurements are also possible with fluorescent probes whose fluorescence decay is temperature sensitive. The time scales of fluorescent decay can be in the nanosecond range and high-speed temperature measurements in intervals as short as 18 ns have been reported.[2] Because fluorescence requires a source of light, it is possible to select specific regions to measure by altering the location, and geometry of the excitation light. The spatial confinement of the measurement area provides the ability to measure within 3D structures as well as in 2D planes deep inside samples. Finally, through careful choice of the molecular probe, fluorescence thermometry can be adapted for use in systems with environments hostile to conventional methods of temperature measurement.[9]

2.3 Fluorescence

2.3.1 Photophysical Mechanism

Fluorescence is a sub-class of a broader phenomenon of luminescence which refers to the emission of light by electronic state transitions. The photophysical mechanism of fluorescence is as follows: First an electron in the ground state of fluorescent molecule absorbs a photon. This event excites the electron to the excited singlet state. After a decay time, known as the fluorescence lifetime, the electron returns to the singlet ground state, either by emitting a photon, or through a non-radiative pathway. The ratio of emitted photons to absorbed photons is known as the quantum yield. Phosphorescence is the other sub-class and operates in a similar manner, with the exception that the electronic state transitions are from an excited triplet state to the singlet ground state. Empirically fluorescence and phosphorescence are distinguished by their lifetime, which is defined as the average time of transition between the excited and ground state. Fluorescent molecules typically have a lifetime in the nanosecond range, while phosphorescent molecules have lifetimes that are much longer, on the order of milliseconds to seconds. While some phosphorescent materials are used as temperature sensors, this work focuses on fluorescent probes, which have better temporal response due to their shorter lifetimes. Two common terms used in conjunction with fluorescence work are excitation and emission. Excitation refers to the light used to radiatively excite the fluorescent material and the fluorescent light radiated is referred to as the emission. The most common fluorescence data measured are the emission

spectrum and excitation spectrum. The emission spectrum is a plot of the intensity of light emitted by the fluorescent material at different wavelengths versus the wavelength. This plot shows all the wavelengths of light that the material can emit. The excitation spectrum is a plot of the intensity of light at the emission peak versus the excitation wavelength, and shows the effectiveness of a particular wavelength at exciting fluorescence. The difference in wavelength between the emission peak and excitation peak is called the Stokes' shift and its length has important implications for separating light from multiple fluorescent species. One important characteristic of fluorescence is that the shape of the emission spectrum remains the same regardless of the excitation wavelength. This feature greatly increases the flexibility of fluorescent probes because a range of excitation wavelengths can be used to produce fluorescence, which in turn means that a greater variety of excitation sources can be used. The invariance of fluorescence with excitation wavelength is commonly used as a diagnostic for separating light scattering from fluorescence. Light scattering occurs when radiation is reflected from a molecule and can appear like fluorescence in a fluorescence spectrum. The wavelength of the scattered light is determined by the wavelength of the incident light and thus a shift in the excitation wavelength will shift the peak intensity in the same direction as the change in the excitation wavelength. This is different from fluorescence, where the peak position of the emission remains the same despite a change in the excitation wavelength.

2.3.2 Temperature Dependent Fluorescence

Fluorescence spectroscopy has become important in many scientific fields because changes in the emission spectrum in many fluorophores can be tied to specific physical phenomena. The changes in fluorescence has been exploited by a number of companies and a wide selection of fluorescent probes now exist that range from probes that detect physical properties, such as pH and temperature to more exotic probes that detect specific sites on DNA sequences. The specific fluorescence change depends on the application. A common design is to create a fluorescent molecule that dramatically increases its fluorescence intensity when it is bonded to a target molecule. This on-off fluorescence behavior is typically used in detection tasks. The other method of detection requires a probe that displays a continuous change in fluorescence properties rather than a step change. There are three types of spectral changes in

fluorescence used for measurements: changes in the fluorescence emission intensity, changes in fluorescence decay time, and a shift in the emission peak. Examples of these spectral changes can be seen in three different temperature sensitive fluorescent probes: Rhodamine B, $CaF_2:Yb^{2+}$, and BTBP {N,N'-bis(2,5-di-*tert*-butylphenyl)-3,4,9,10-perylenedicarboximide}. Rhodamine B changes in intensity with temperature[10, 11], $CaF_2:Yb^{2+}$ changes fluorescence decay time with temperature[12] and BTBP shifts its fluorescence wavelength with temperature.[9] While all three methods can measure temperature, the detection of the spectral change is the limiting factor on its usability. The detection of fluorescence lifetime and frequency shift is difficult to accomplish in 2D and thus are not suited to the requirements for measuring temperature in a microwave system. Fluorescence intensity change with temperature is optically much simpler to measure and we focused our search on probes with this characteristic.

2.3.3 Temperature Measurement with Emission Intensity Change Fluorescent Probes

In order to measure temperature with a fluorescent probe with a temperature sensitive fluorescence emission, we must develop a method of relating the intensity to temperature. There are three approaches to matching the fluorescence with temperature and they are: absolute calibration, normalization, and referenced measurements (ratiometric). The absolute calibration approach directly maps the fluorescence output detected to the temperature. The direct correlation between the detected fluorescence and temperature is likely to be the most accurate if the system does not optically change. In a normalized approach the fluorescence intensity is measured at a normalization temperature and measurements at other known temperatures are divided by the fluorescence intensity at the normalization temperature. A function is fitted to the normalized data. In subsequent experiments, the fluorescence data from the measured system is normalized by dividing it with the intensity at a known temperature, usually taken at the start of an experiment. The previously determined function is then applied to calculate the temperatures. Normalization is mathematically simple and provides some degree of protection against errors because the normalization measurement acts as a reference point for each experiment. In a referenced approach, a second fluorescent probe, which has little or no temperature dependent fluorescence, is used to internally calibrate the fluorescence intensity. A fluorescence signal that is independent of the excitation source intensity can be measured by dividing the output of the

two fluorescence peaks. In some rare cases, a single probe molecule may have two peaks, one that is independent of temperature and one that is temperature sensitive. This dual emission probe can act as its own reference and renders a second reference probe unnecessary.

One limitation of the absolute calibration and normalization methods is that they depend on the stability of the excitation source. Both of these techniques depend on a single measurement of the fluorescence intensity as the calibration for temperature response and thus assumes that the excitation source intensity remains constant for subsequent measurements. Unfortunately, there is some drift in the excitation intensity with all excitation sources. In the calibrated approach, the excitation intensity is a part of the function that describes the relation of intensity with temperature. Thus the absolute calibration depends on excitation intensity remaining constant between experiments. Normalization is more robust because the reference is done with each experiment, so as long as the excitation intensity is constant in the experiment, the function is a valid description of the temperature dependence. For macroscopic single point measurements, the dependence on the excitation intensity is less important than the multi-dimensional case. In the 1D case the entire illumination area is treated as one average signal, smoothing spatial variations and increasing the signal to noise ratio. Also, with the 1D case, a variety of techniques can be used to sample the excitation beam in real time and provide a reference signal to normalize the fluorescence intensity. Unfortunately, for 2D and 3D temperature measurements, the combination of sampling the excitation light in 2D and matching it with spatial locations in the fluorescing sample is difficult. Instead of an elaborate excitation sampling scheme for 2D targets, the referenced approach provides the necessary excitation calibration.

The referenced approach is the most robust method, and in the ideal case is based on a dual-chromophore probe. Alternatively, a combination of two probess can be used as well. One dual-chromophore probe considered was PMPBA { N-1-Pyrenylmethyl-1-pyrenebutanamide} which was synthesized by Lou.[13, 14] PMPBA is a temperature sensitive fluorescent probe that has two emission peaks, one which is temperature sensitive, and one that isn't. The ratio of the fluorescence from these two peaks provides an internal reference for the excitation intensity, which eliminates excitation stability as a source of error. PMPBA consists of two pyrene

molecules linked by a molecular bridge. At high concentrations pyrene can form a dimer structure called an excimer which has a fluorescence signal that is at a different wavelength than the normal monomer emission. Linking two pyrene molecules together constrains the motion of the two pyrene molecules and increases the probability of excimer formation. This also dramatically reduces the probe concentration necessary to see excimer formation compared to free pyrene. The excimer fluorescence peak changes in response to temperature because the distance between the two linked pyrene molecules varies with the temperature, affecting the rate of excimer formation. Unfortunately the greatest drawback to PMPBA is that it requires a UV source for excitation, making it a more dangerous and more difficult optical system with which to work. Thus we began a search for an alternative temperature sensitive probe with an excitation wavelength band in the visible range.

2.3.3.1 Rhodamine B

There is a considerable library of fluorescent temperature sensitive molecular probes available to use, spanning a considerable range of temperatures from 20 to 2000 °C and a wide variety of solvent environments.[14] The choice of a probe for a specific application is determined by the temperature range and the compatibility of the probe with the target material to be measured. In this thesis work, the choice of probe was determined by temperature range, aqueous solubility, and excitation wavelength. One probe that satisfied the requirements for our microwave experiments was Rhodamine B. Rhodamine B is a xanthene dye with the chemical structure shown in Figure 1 and a fluorescence spectrum as shown in Figure 2.

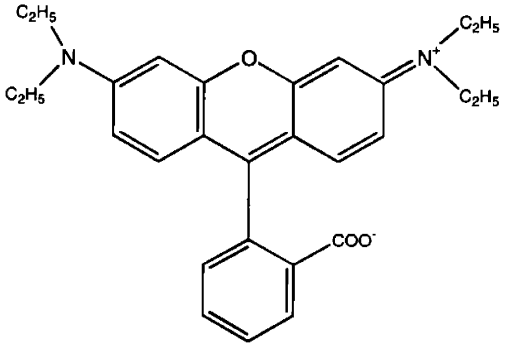

Figure 1: Chemical Structure of Rhodamine B

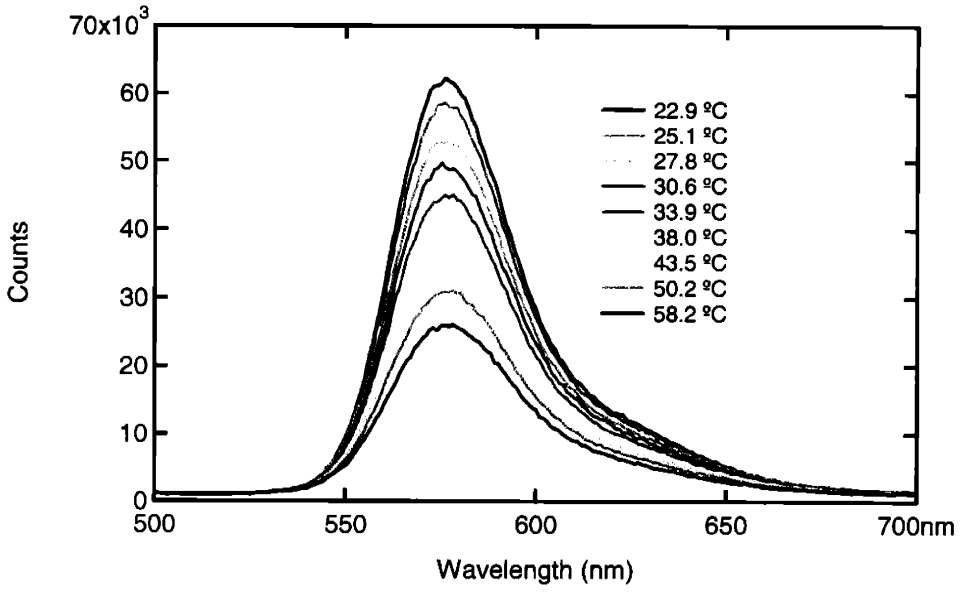

Figure 2: Rhodamine B Fluorescence Change with Temperature

From Figure 2 it is apparent that Rhodamine B fluorescence is strongly temperature dependent. The photophysical phenomenon responsible for the temperature dependence of Rhodamine B is widely believed to be a result of a change in the free-rotation of the diethylamino groups on the xanthene ring.[15] At lower temperatures, the hindered rotation of these groups results in a planar form that closely resembles Rhodamine 101, a fluorescent probe with a quantum yield near unity, while at higher temperatures the out-of-plane configuration increases proportionally, resulting in lowered quantum yield. Rhodamine B has a number of properties that make it suitable for our application. It is fairly soluble in water and has a high quantum yield as well as a large change in quantum yield as a function of temperature,[16] which aids in detection. Additionally, Rhodamine B has been well characterized and used extensively in the literature as a temperature probe.[10, 11 2, 17-23] As seen in Figure 2, the range of temperature sensitivity for Rhodamine B is from 10 °C to 60 °C. This range is well suited to studies of water because it lies between points of phase transition. The overlaid absorption and fluorescence emission spectra for Rhodamine B are shown in Figure 3 and the absorption and fluorescence peaks are located at 554 nm and 576 nm, respectively. The leading edge of its absorption spectrum includes the 488 nm and 514 nm emission lines of an argon-ion laser. Our sample for microwave heating is water, which presents unique challenges. In a fluid system, the optical properties of any direct observation path are likely to change in the presence of convection driven flows.

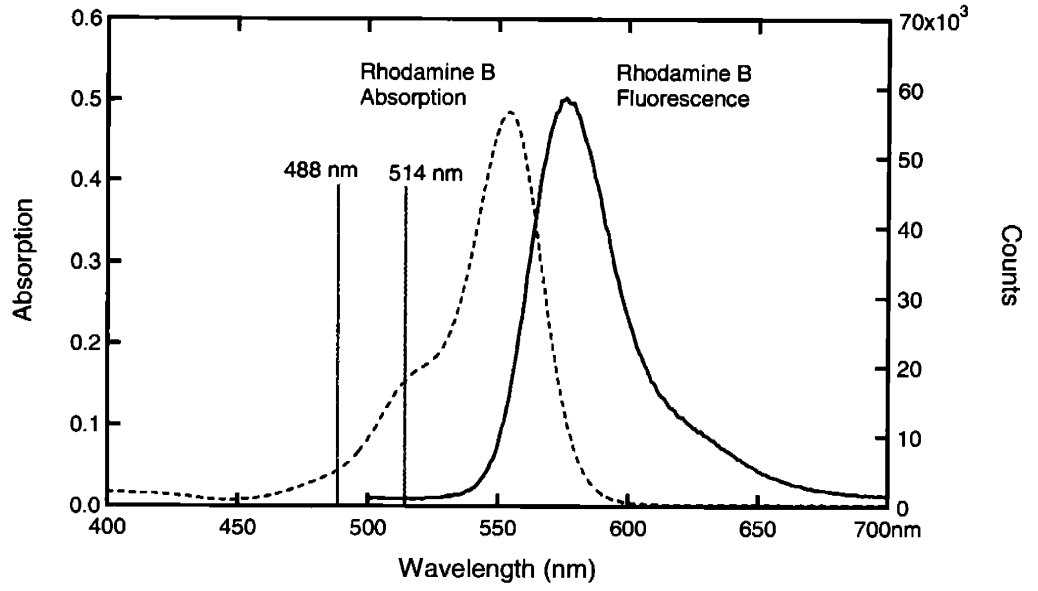

Figure 3: Overlapped Rhodamine B Absorption and Fluorescence

Therefore we need to be able to correct for changes both in the power distribution of the excitation source as well as changes in the optical medium. To account for this a referenced approach to measure the temperature was used and a probe complementary to Rhodamine B was selected to act as the reference for the excitation intensity. The ideal reference probe has perfect spectral isolation from the measurement probe, and can be excited by the same source. If multiple excitation sources are used, the referenced approach loses its utility in reducing excitation light noise. In addition, aligning multiple excitation sources is optically complex and the addition of a second excitation source increases the cost of the system. We elected to avoid this complexity and focus our search for a compatible probe with the same excitation wavelength and an emission band spectrally isolatable from Rhodamine B fluorescence.

2.3.3.2 Rhodamine 110

Sakkibara & Adrian reported success in using Rhodamine 110 as a reference probe for a fluorescence-based temperature measurement system based on Rhdoamine B.[11] Thus Rhodamine 110 was selected as a suitable candidate to act as a reference probe to Rhodamine B. The chemical structure of Rhodamine 110 is shown in Figure 4 and like Rhodamine B it is also a xanthene dye with a high quantum yield. Rhodamine 110 exhibits little temperature dependence in its fluorescence behavior as seen in Figure 5.

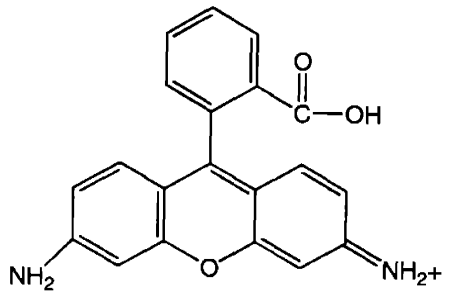

Figure 4: Chemical Structure of Rhodamine 110

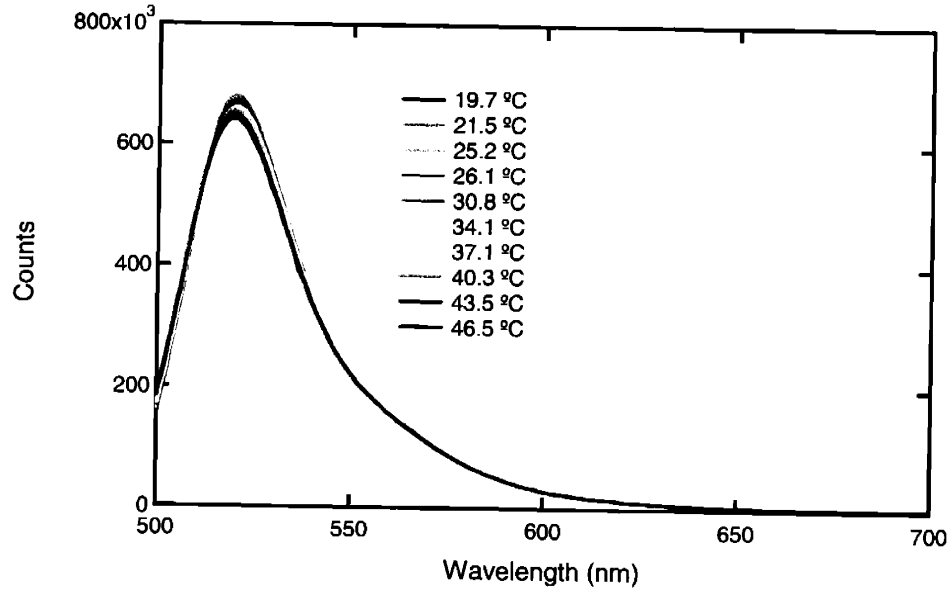

Figure 5: Rhodamine 110 Fluorescence Change with Temperature

Rhodamine 110's absorption and fluorescence peaks occur at 496 nm and 519 nm, respectively. Similarly to Rhodamine B, the absorption spectrum encompasses the principal lines of the argon-ion laser as seen in Figure 6. Rhodamine 110 therefore fulfills the basic requirements as reference probe for Rhodamine B with low temperature dependence in its fluorescence and an excitation spectrum that includes the same Argon-Ion laser lines as Rhodamine B. The final spectral requirement for Rhodamine 110 as a reference probe for Rhodamine B fluorescence is whether the two probes have spectrally separable fluorescence. This question is addressed in the next section.

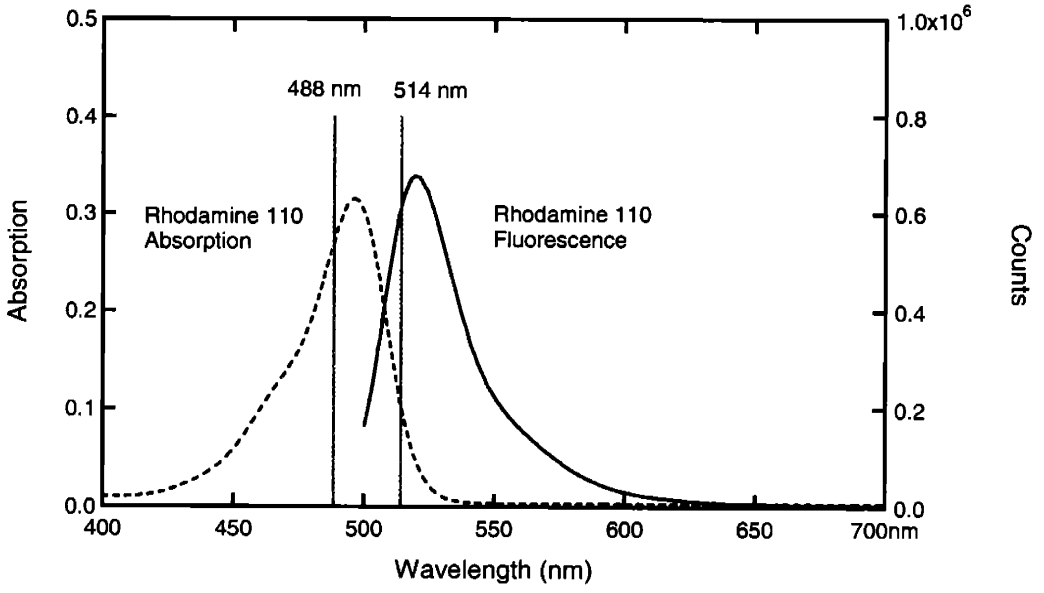

Figure 6: Overlapped Rhodamine 110 Absorption and Fluorescence

2.3.3.3 Analysis of Spectral Overlap

The suitability of a pair of fluorescent species to act as a complementary set for ratiometric measurements depends greatly on the overlap of their respective absorption and emission spectra. There are three types of spectral overlaps between the species, absorption-absorption, absorption-emission, and emission-emission overlap. The absorption-absorption overlap is the trivial case, and is required so that a single source can excite both probes. The absorption-emission overlap can result in additional fluorescence in one species, and attenuation of the second species. The emission-emission overlap obscures the true ratio, making it difficult to separate the fluorescence of the reference and measuring species. Absorption-absorption and absorption-emission overlaps depend on careful selection of the fluorescent species. Careful selection can reduce the emission-emission overlaps, but due the relatively small Stokes shift for most fluorescent species, some overlap is inevitable. The effect of the overlap can be reduced by using the narrowest bandwidth filters available to isolate areas of the spectrum where the overlap is at a minimum. Sakkibara & Adrian have also shown that it is possible to calibrate the contribution of each species in an overlapped emission-emission signal in ratiometric measurements.[11] In their solution the actual fluorescence intensities are not extracted, but the

ratio of fluorescence intensities is computed and that is sufficient for making temperature measurements.

We have already shown earlier that Rhodamine B and Rhodamine 110 have absorption spectra that overlap and contain both Argon-Ion laser emission lines. Thus the two probes are compatible for the absorption-absorption case. For the absorption-emission overlaps, the spectra for Rhodamine 110 and Rhodamine B are shown in Figure 7 and Figure 8.

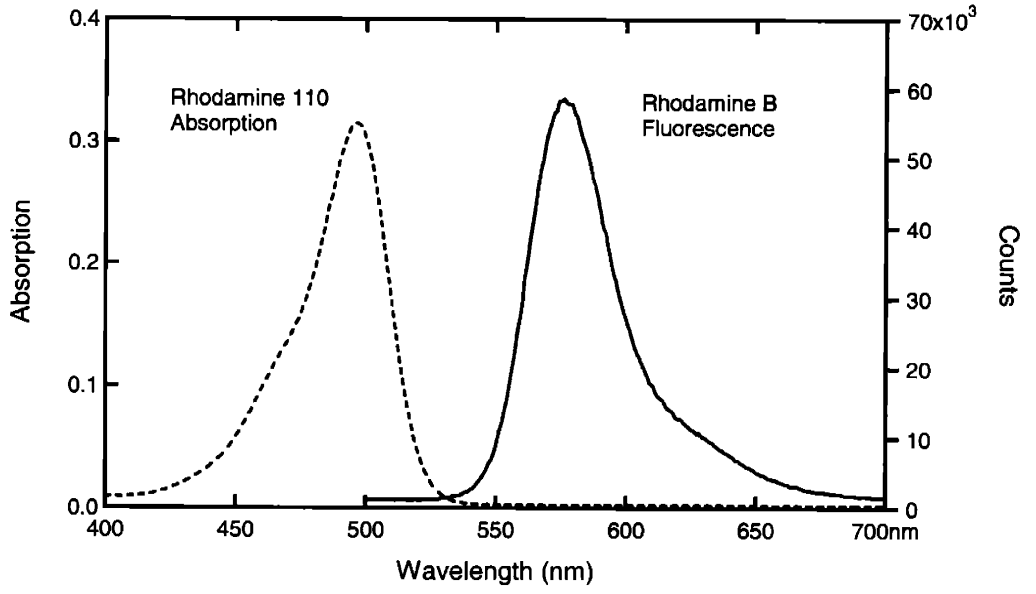

Figure 7: Rhodamine 110 Absorption of Rhodamine B Fluorescence

The absorption spectrum of Rhodamine 110 and the fluorescence spectrum of Rhodamine B are completely separate. This is the ideal case and thus we need not be concerned about the concentration of Rhodamine 110 affecting the Rhodamine B fluorescence signal through absorption. But the reverse case is not as clear-cut as seen from the overlapped spectra shown in Figure 8. There is a significant overlap of the absorption spectrum for Rhodamine B and the fluorescence spectrum of Rhodamine 110, which indicates that the Rhodamine 110 fluorescence can excite fluorescence from Rhodamine B. To minimize exciting significant fluorescence from Rhodamine B, it is important to keep the Rhodamine 110 concentration low. At low concentrations, the excitation provided by the excitation source will be far greater than that from Rhodamine 110 fluorescence.

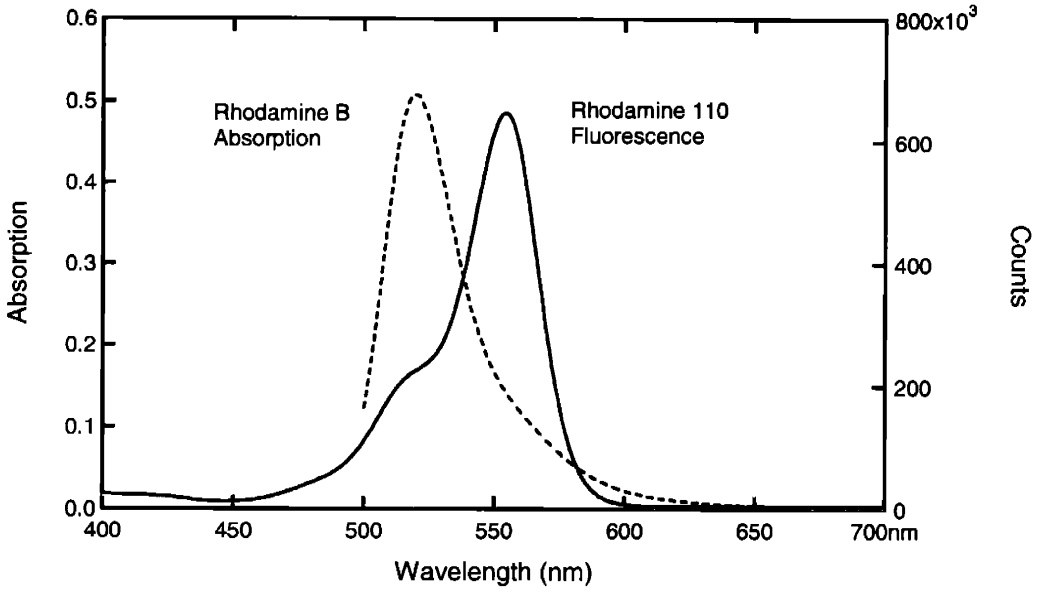

Figure 8: Rhodamine B Absorption of Rhodamine 110 Fluorescence

Rhodamine B concentration also must be low enough to avoid significant absorption of Rhodamine 110 fluorescence so that measurements of can be made of it. The most important tool to reduce the effect of absorption-fluorescence overlap is control of concentration. By keeping concentrations as low as possible, the absorption effects are minimized.

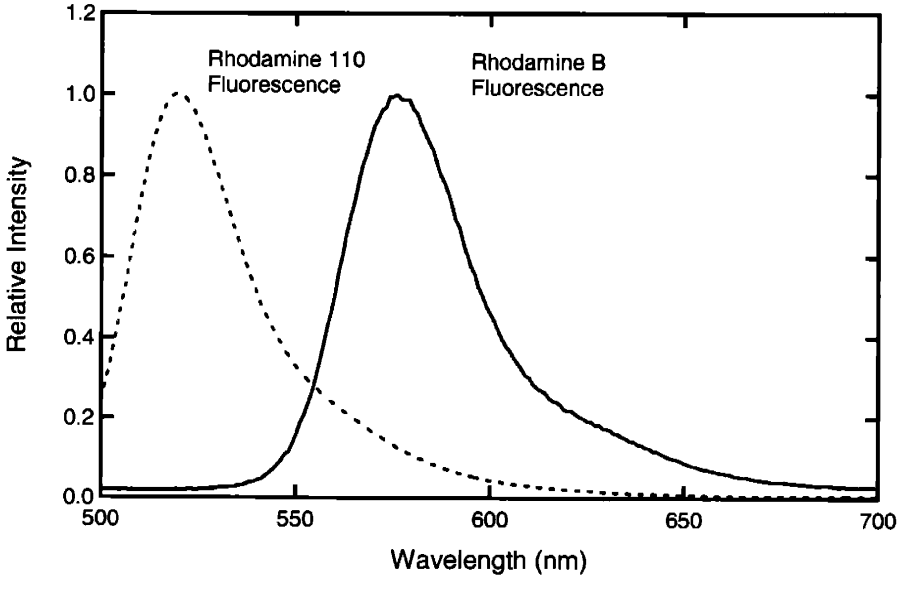

Figure 9: Rhodamine 110 and Rhodamine B fluorescence spectra on a relative (to peak) scale.

The emission-emission overlap for Rhodamine B and Rhodamine 110 is shown in Figure 9 and on first inspection the overlap is small. This suggests that Rhodamine B fluorescence should be simple to isolate from the Rhodamine 110 fluorescence. In Figure 9 the fluorescence intensity is plotted relative to its peak value for comparison of the spectral structures of the two probes. However if the fluorescence intensity is plotted on an absolute scale, as shown in Figure 10, a very different conclusion results.

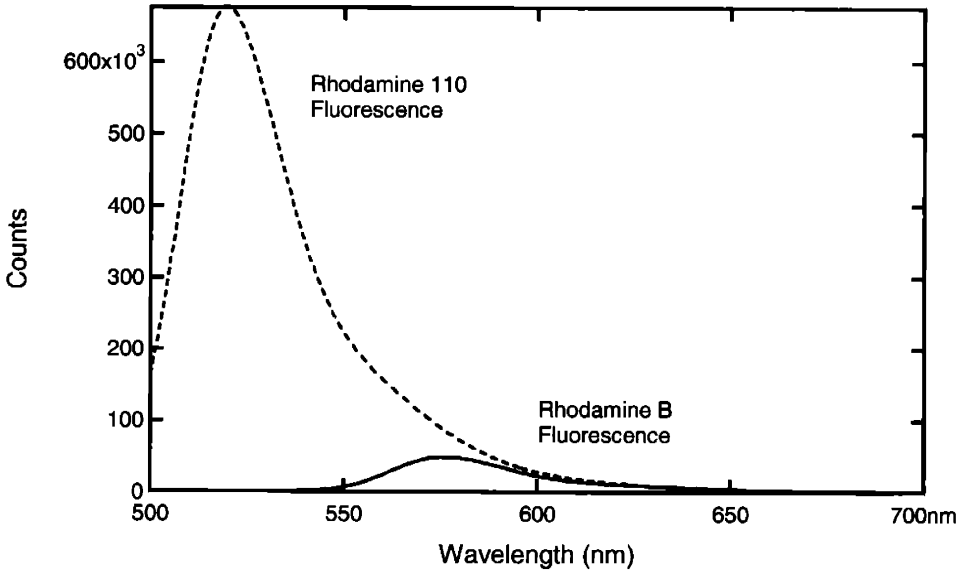

Figure 10: Rhodamine 110 and Rhodamine B fluorescence on an absolute scale.

In Figure 10 it is clear that, for the particular concentrations of probes chosen to balance detection and absorption, the actual intensity of the fluorescence of Rhodamine 110 at the tail exceeds the peak emission of Rhodamine B. Thus, there is significant emission-emission overlap. It is important, when using normalized fluorescence data for probes typically found in the literature, to pay careful attention to the absorbance spectra and concentrations used when considering emission-emission overlaps. With this significant emission-emission overlap of Rhodamine B and Rhodamine 110, we turn to mathematical processing of the data to retrieve the actual fluorescence data.

2.3.3.4 Calculating Temperature from Two Fluorescent Probes

From the previous section, we have seen that the Rhodamine B peak is masked by the emission-emission overlap of Rhodamine 110 and Rhodamine B. Following the derivation by Sakkibara & Adrian, it is possible to extract the actual ratio of the fluorescence signal using a designed series of calibration measurements.[11] The mathematical derivation is presented here.

The fluorescence intensity (I) can be expressed as the following expression:

$$I = C\phi\varepsilon \tag{2-1}$$

where (C) is the concentration of the probe, (ϕ) is the quantum yield and (ε) is the extinction coefficient. The quantum yield is the temperature dependent component of the equation and the extinction coefficient is a property of the material. We will label two probes A & B and the intensity output of two cameras as V^{α} and V^{β} respectively. Each camera reports a signal that is a combination of the fluorescence emission from the two probes so we will define fractions (F) for each camera and probe combination, using the subscript to denote the probe and the superscript to denote the camera. Thus, for example, $F_A{}^{\alpha}$ refers to the fraction of the fluorescence signal of probe A that is detected in camera α.

$$V^{\alpha} = F_A^{\alpha} I_A + F_B^{\alpha} I_B = I_0\left(F_A^{\alpha} C_A \phi_A \varepsilon_A + F_B^{\alpha} I_B C_B \phi_B \varepsilon_B\right) \tag{2-2}$$

$$V^{\beta} = F_A^{\beta} I_A + F_B^{\beta} I_B = I_0\left(F_A^{\beta} C_A \phi_A \varepsilon_A + F_B^{\beta} I_B C_B \phi_B \varepsilon_B\right) \tag{2-3}$$

To solve for the fractions, we need to do two calibration experiments. In these experiments only a single probe will be used. It is important to note that the calibration is only valid for cases where the absorption of fluorescence by the other probe is negligible. We use primes to denote where the values are specific to the experiment.

Fluorescent Probe B only case:

$$F_B^{\alpha} = \frac{V_B^{\alpha}}{I_0' C_B' \phi_B' \varepsilon_B} \tag{2-4}$$

$$F_B^{\beta} = \frac{V_B^{\beta}}{I_0' C_B' \phi_B' \varepsilon_B} \tag{2-5}$$

Fluorescent Probe A only case:

$$F_A^{\alpha} = \frac{V_A^{\alpha}}{I_0'' C_A' \phi_A' \varepsilon_A} \tag{2-6}$$

$$F_A^{\beta} = \frac{V_A^{\beta}}{I_0'' C_A' \phi_A' \varepsilon_A} \tag{2-7}$$

In equations 2-6, 2-7 we have used I_0'' to represent the excitation light because the probe A experiments are separate from the probe B experiments. It is important to realize that this derivation assumes that absorption contributions are small so that the single probe calibration images are correct. In addition there is an assumption that the calibration data have the same excitation intensity profile so that the signals are spatially comparable. We can then substitute these calculated fractions back into the expressions for the camera signal to get:

$$\frac{V^{\beta}}{V^{\alpha}} = \frac{\frac{1}{I_0''}\left(\frac{C_A \phi_A \varepsilon_A}{C_A' \phi_A' \varepsilon_A}\right) V_A^{\beta} + \frac{1}{I_0'}\left(\frac{C_B \phi_B \varepsilon_B}{C_B' \phi_B' \varepsilon_B}\right) V_B^{\beta}}{\frac{1}{I_0''}\left(\frac{C_A \phi_A \varepsilon_A}{C_A' \phi_A' \varepsilon_A}\right) V_A^{\alpha} + \frac{1}{I_0'}\left(\frac{C_B \phi_B \varepsilon_B}{C_B' \phi_B' \varepsilon_B}\right) V_B^{\alpha}} \tag{2-8}$$

For this calibration to reduce properly we must make a critical assumption that the excitation light intensity remains constant during the calibration experiments, i.e., that:

$$I_0' = I_0'' \tag{2-9}$$

We will make the following substitutions to simplify the equations,

$$A = \frac{C_A}{C_A' \phi_A'} \tag{2-10}$$

$$B = \frac{C_B}{C_B' \phi_B'} \tag{2-11}$$

$$R = \frac{V^{\beta}}{V^{\alpha}} \tag{2-12}$$

so that we can rewrite equation 2-8 as:

$$R = \frac{A\phi_A V_A^{\beta} + B\phi_B V_B^{\beta}}{A\phi_A V_A^{\alpha} + B\phi_B V_B^{\alpha}} \tag{2-13}$$

The ratio of the temperature dependent quantum yields can then be determined to be:

$$\frac{\phi_B}{\phi_A} = \frac{A}{B}\left(\frac{V_A^{\beta} - RV_A^{\alpha}}{RV_B^{\alpha} - V_B^{\beta}}\right) \tag{2-14}$$

This equation converts the camera ratio to a ratio of the quantum yield which, with a description of the temperature dependence of the quantum yield, will allow us to solve for temperature.

There are two approaches to determining the temperature dependence of the quantum yield: 1. Use the camera system to measure intensities at each temperature point to determine a fitting function. 2. Measure the fluorescence temperature response in a fluorimeter and couple those results with a mathematical approximation to the optical setup. The first method uses the same system for temperature calibration and measurement and simplifies the calibration from a mathematical standpoint. However, this method is more complex experimentally because it requires a temperature controlled measurement cell for calibration. Such a cell might not be possible for some experimental setups. Furthermore, any change to the detector optical path would require a recalibration. The second method splits the temperature calibration procedure into two components: the measurement of the quantum yield ratio and the measurement of the detector optical path. The first component is measured directly on a fluorimeter equipped with a temperature controlled sample cell. The use of a separate fluorimeter frees the experimental design from the constraint of a temperature controlled calibration cell. A separate set of measurements can be made to estimate the effect of the filters in the detection pathway. The advantage of this system is that the most time consuming step, the measurement of the temperature dependence of the ratio of the fluorescence from the probes, is only measured once. Any changes to the optical path can be handled by making new measurements only on the elements in the detection optical path. Because of the difficulty of installing a temperature controlled calibration cell in the microwave cavity the second method was chosen.

Of the two parts for determining the temperature dependence function, the optical path approximation is simpler. The detector path is dominated by the performance of the filters

located in front of the cameras. The filter transmittance is measured by UV-VIS and this result is then multiplied with fluorescence measurements to approximate the effect of the filter in the camera system. Determining temperature dependence of the quantum yield ratio requires some mathematical treatment. We begin the derivation with the fluorescence intensity equation as it appears in Equation 2-1.

$$I = C\phi\varepsilon \tag{2-1}$$

With two fluorescent probes, A and B, the equation can be re-expressed as a ratio:

$$\frac{I_B(T)}{I_A(T)} = \frac{C_B\phi_B(T)\varepsilon_B}{C_A\phi_A(T)\varepsilon_A} \tag{2-15}$$

Rearranging the terms yields:

$$\frac{I_B(T)}{I_A(T)}\left(\frac{C_A\varepsilon_A}{C_B\varepsilon_B}\right) = \frac{\phi_B(T)}{\phi_A(T)} \tag{2-16}$$

Equation 2-16 expresses the temperature dependence of the quantum yield ratio as a function of the fluorescence intensity, concentration and extinction coefficient. The constant factor

$$\left(\frac{C_A\varepsilon_A}{C_B\varepsilon_B}\right) \tag{2-17}$$

is computed by solving equation 2-16 at 20 °C, the temperature at which the quantum yields are known.

Molecular Probe	**Quantum Yield**
Rhodamine 110[11]	0.8
Rhodamine B[11]	0.31
Dextran Labeled with Rhodamine B	0.11

Table 1: Quantum yield of Rhodamine dyes at 20 °C.

The fluorescence intensity data measured with the fluorimeter is not the same as the intensity data that is measured by the camera. While the fluorimeter can arbitrarily measure a particular wavelength, the camera performance is defined by the filter in front of it. The camera

measurement is modeled by multiplying the fluorimeter data with the transmittance curves for the two filters in front of the cameras. A fit is then performed on the resulting intensity data to get the form of the $I(T)$ ratio. The plot for the Rhodamine B labeled Dextran and Rhodamine 110 probe ratio is shown in Figure 11.

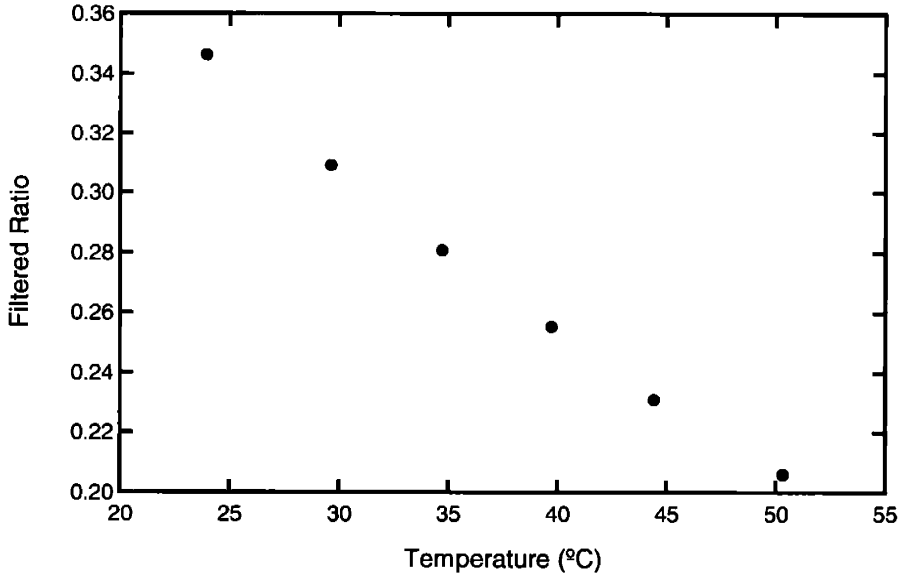

Figure 11: Filter Transmission multiplied with ratio of Rhodamine B labeled Dextran and Rhodamine 110

Rhodamine B has been shown in the literature to have linear temperature dependence[10, 11] and Rhodamine 110 has very little temperature dependence. The ratio is linear and shows no significant difference when Rhodamine B is attached to a Dextran polymer. The linear fit is multiplied with the calculated constant factor of concentration and extinction coefficients to describe the quantum yield temperature dependence.

Equation 2-16 describes the temperature dependence of the quantum yield ratio; however, in practice there are errors in concentration, differences in filter performance at different imaging positions, and variations in background light that will reduce the accuracy of the temperature measurement. To increase the accuracy of an experiment, the function is normalized to an image from the system of a constant temperature sample. This is accomplished by capturing images at room temperature, before an experiment is started. The mean is computed for these images and the 2D matrix of ratios is used to calculate the intercept of the temperature function for each

pixel position. The resulting matrix of temperature functions is then used to calculate the temperatures during the experiment.

A process of calculating the actual ratio of the fluorescence of two overlapping probes has been shown through mathematical derivations. The procedure requires two calibration experiments which measure the fluorescence of each probe in isolation. The resulting fluorescence ratio can be coupled with a functional description of the dependence of quantum yield with temperature to make temperature measurements in a dual fluorescent probe system with significant emission-emission overlaps.

2.4 Imaging Systems Overview

In order to measure temperature with a fluorescence signal, we must be able to excite the fluorescence response from the probe and to measure it. In the following section we examine the trade-offs between the two main choices for an excitation source, the lamp and the laser. The detection of fluorescence emissions is equally important and the two main detector technologies, photomultipliers and CCDs are examined in detail.

2.4.1 Fluorescence Excitation Sources

There are two basic light sources for fluorescence work, lamps and lasers, each of which has its own strengths and weaknesses. Lamps are the primary choice for most fluorescence work, with the major advantage of spectral adaptability. Lamps provide illumination over a broad range of wavelengths which can be narrowed by an appropriate filter, making them ideal in situations where many fluorescent probes may be used. They are simple to operate and maintenance is relatively inexpensive. However, lamps distribute their irradiance across a broad spectrum, limiting the output power in any single wavelength. Additionally, the output of a lamp is not tightly collimated, making it difficult to use in situations where the excitation light illumination needs to be spatially restricted. The intensity profile of the lamp is not consistent. While the specifics depend greatly on the exact lamp, the most common arc lamps depend on a high voltage arc through a mercury or xenon vapor that generates the light. The arc is subject to a phenomenon known as arc wander where the exact position of the arc varies in time randomly.

The arc wander results in variations in the spatial and temporal intensity of the excitation beam, however over sufficient integration time, the beam can appear free of large changes in intensity.

The laser's primary advantages are the narrow bandwidth of the particular wavelength that is output and collimation of the output beam. This combination of features allows selective illumination of a sample both spectrally and spatially. Lasers also scale to higher output power in a specific wavelength than lamps. There are two basic types of lasers, continuous wave and pulsed. Continuous wave lasers act much as lamps, producing a continuous stream of photons. Pulsed laser concentrate their light output into pulses of photons that may last no more than a few nanoseconds. Pulsed lasers can achieve extremely high photon flux over a short interval and are often preferred for high-speed applications where a system event is triggered or otherwise timed with the laser pulse. The biggest drawback to lasers is the restriction in available wavelengths. There are several specific laser lines that are obtainable easily due to the lasing materials used. However to obtain other wavelengths requires either a combination of a pump laser and power consuming methods such as frequency doubling, dye lasers, or other exotic technologies for lasing. The two most common lasers found in research use are the Argon-Ion laser, producing power in two lines at 488 nm and 514 nm, and Nd:Yag laser, which produces 1064 nm radiation, typically frequency doubled (532 nm), tripled (355 nm), and quadrupled (266 nm). The development of high power diode laser has led to some exotic designs and access to new ranges of laser lines, though often at significant cost. The laser power output, as with the lamp, depends greatly on the specific type of laser. However, in general, lasers have more consistent power output and control on the beam intensity than lamps. Lasers also vary greatly in their initial and maintenance cost.

For fluorescence imaging of molecular probes in 2D the advantage of the laser's spatial control over the lamps is undeniable. With the laser it is possible to illuminate a specific region of a sample container and thus restrict the fluorescence to that region. This allows measurement of the probe's fluorescence response in a specific location as opposed to the aggregated fluorescence of the entire sample cell. For this reason, the laser was chosen as the excitation source for the fluorescence thermometer

2.4.2 Fluorescence Emission Detectors

The choice of detectors in recent years has fallen primarily into two technologies; CCD detectors for 2D imaging and photomultiplier tubes for point measurements. Photomultiplier tubes are based on a charge amplification design.

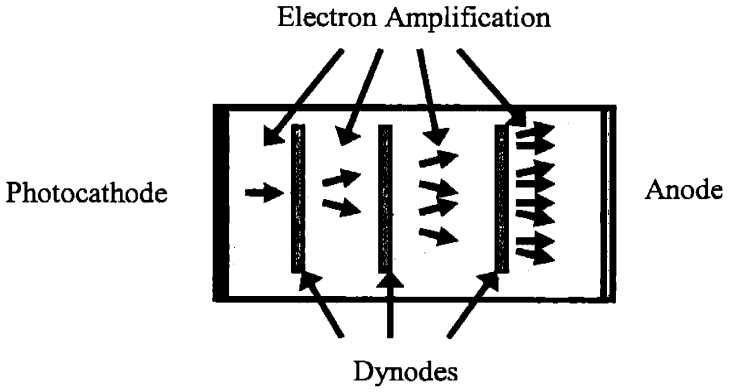

Figure 12: Photomultiplier tube design

The photocathode at the front releases electrons when struck by photons. The photons are accelerated by a potential difference between the photocathode and the next plate, known as the first dynode. This acceleration and impact produces more electrons and these resultant electrons then move to the next dynode. Thus, there is an amplification of the original signal which depends on the number of dynodes and potential difference between the stages.[24] Photomultipliers are very high gain devices capable of detecting very low signals down to almost single photon events. However they are limited to single point measurements and are often found in spectrometers.

The CCD is an imaging device that captures 2D snapshots of the photon flux to its surface. CCDs are used in most commercial and consumer digital still and video cameras as well as telescopes for astronomical observations. The CCD, or charge-coupled device, is a solid state detector composed of an array of metal oxide semiconductor (MOS) capacitors. The CCD operates by using the MOS capacitors store a charge generated when photons strike the silicon.[25] The individual capacitors are connected by electrical traces and shift these packets of charges to an amplifier which measures the charge and sends the resulting signal to an analog-to-digital

converter (ADC). The technology behind CCDs is rapidly advancing, achieving faster readout rates and lower noise every year. The primary limitation of most CCDs is low wavelength sensitivity in the UV range. Extended UV response is provided by a more expensive variant of the CCD that has a very thin substrate and is mounted in reverse. These are known as back-illuminated CCDs and they have the extended UV response, but smaller size capacitors which hold less charge. For very low light applications, a hybrid photomultiplier and CCD combination has been developed, called the intensified CCD. The intensified CCD camera has a photocathode at the front and an anode directly in front of the CCD. The original photons strike the photocathode and dislodge electrons which and are accelerated to the anode by an electric field, the anode is coated with a scintillating material that generates photons from the electrons and photons are captured by the CCD. For our application, the CCD is the obvious choice, since it provides imaging capabilities. Fortunately, the quantum yields of the molecular probes we use are high, so an intensified CCD camera is not needed.

2.5 Conclusion

Temperature measurements using molecular probes provides many advantages over conventional methods, such as fast time response, small length scale, 2D and 3D spatial measurements, and remote non-invasive thermometry in hostile environments. The choice of the molecular probe is the central decision in the development of an instrument for fluorescence-based thermometry, determining, in large part, the equipment needed for detection and excitation. For this work, a water soluble temperature sensitive xanthene dye, Rhodamine B was selected. To avoid variations in fluorescence associated with changes in excitation intensity, a ratiometric method of measurement was selected. This required a complementary temperature insensitive xanthene dye, Rhodamine 110, to act as a reference for the excitation intensity. The combination of the two fluorescent probes has significant absorption-emission and emission-emission overlaps. The absorption-emission overlap is handled by careful control of concentration, while the emission-emission overlap is handled by a series of calibration experiments and mathematical treatment of the fluorescence data. The excitation source and emission detector were chosen to be the laser and CCD camera, respectively. The spatial control of illumination coupled with the CCD camera's imaging capabilities make capture of 2D

temperature fields inside a sample container possible. In the next chapter, the design decisions in the construction of the fluorescence thermometry instrument are explored in detail along with an explanation of many problems that complicate fluorescence measurements.

References:

1. Childs, P.R.N., J.R. Greenwood, and C.A. Long, *Review of Temperature Measurement.* Review of Scientific Instruments, 2000. **71**(8): p. 2959-2978.
2. Romano, V., A.D. Zweig, M. Frenz, and H.P. Weber, *Time-Resolved Thermal Microscopy with Fluorescent Films.* Applied Physics B, 1989. **49**: p. 527-533.
3. Allison, S.W. and G.T. Gillies, *Remote Thermometry with Thermographic Phosphors: Instrumentation and Applications.* Review of Scientific Instruments, 1997. **68**(7): p. 2615-2650.
4. Zhao, H. and I.W. Turner, *The Use of a Coupled Computational Model for Studying the Microwave Heating of Wood.* Applied Mathematical Modelling, 2000. **24**(3): p. 183-197.
5. Ratanadecho, P., K. Aoki, and M. Akahori, *A Numerical and Experimental Investigation of the Modeling of Microwave Heating for Liquid Layers Using a Rectangular Wave Guide (Effects of Natural Convection and Dielectric Properties).* Applied Mathematical Modelling, 2002. **26**(3): p. 449-472.
6. Dibben, D.C. and A.C. Metaxas, *Finite Element Time Domain Analysis of Multimode Applicators Using Edge Elements.* Journal of Microwave Power and Electromagnetic Energy, 1994. **29**(4): p. 242-251.
7. Kolodner, P. and J.A. Tyson, *Microscopic Fluorescent Imaging of Surface Temperature Profiles with 0.01c Resolution.* Applied Physics Letters, 1982. **40**(9): p. 782-784.
8. Kolodner, P. and J.A. Tyson, *Remote Thermal Imaging with 0.7-Mm Spatial Resolution Using Temperature-Dependent Fluorescent Thin Films.* Applied Physics Letters, 1983. **42**(1): p. 117-119.
9. Schrum, K.F., A.M. Williams, S.A. Haether, and D. Ben-Amotz, *Molecular Fluorescence Thermometry.* Analytical Chemistry, 1994. **66**: p. 2788-2790.
10. Gallery, J., M. Gouterman, J. Callis, G. Khalil, B. McLachlan, and J. Bell, *Luminescent Thermometry for Aerodynamic Measurements.* Reviews of Scientific Instruments, 1994. **65**(3): p. 712-720.
11. Sakakibara, J. and R.J. Adrian, *Whole Field Measurement of Temperature in Water Using Two-Color Laser Induced Fluorescence (Vol 26, Pg 7, 1999).* Experiments in Fluids, 1999. **27**(1): p. U1-U1.
12. Bresson, F. and R. Devillers, *Fluorescence Temperature Sensing on Rotating Samples in the Cryogenic Range.* Review of Scientific Instruments, 1999. **70**(7): p. 3046-3051.
13. Lou, J., T.A. Hatton, and P.E. Laibinis, *Fluorescent Probes for Monitoring Temperature in Organic Solvents.* Analytical Chemistry, 1997. **69**(6): p. 1262-1264.
14. Lou, J.F., T.M. Finegan, P. Mohsen, T.A. Hatton, and P.E. Laibinis, *Fluorescence-Based Thermometry: Principles and Applications.* Reviews in Analytical Chemistry, 1999. **18**(4): p. 235-284.
15. Casey, K.G. and E.L. Quitevis, *Effect of Solvent Polarity on Nonradiative Processes in Xanthene Dyes - Rhodamine-B in Normal Alcohols.* Journal of Physical Chemistry, 1988. **92**(23): p. 6590-6594.
16. Karstens, T. and K. Kobs, *Rhodamine-B and Rhodamine-101 as Reference Substances for Fluorescence Quantum Yield Measurements.* Journal of Physical Chemistry, 1980. **84**(14): p. 1871-1872.

17. Lavieille, P., F. Lemoine, G. Lavergne, and M. Lebouche, *Evaporating and Combusting Droplet Temperature Measurements Using Two-Color Laser-Induced Fluorescence.* Experiments in Fluids, 2001. **31**(1): p. 45-55.
18. Lemoine, F., M. Wolff, and M. Lebouche, *Simultaneous Concentration and Velocity Measurements Using Combined Laser-Induced Fluorescence and Laser Doppler Velocimetry: Application to Turbulent Transport.* Experiments in Fluids, 1996. **20**(5): p. 319-327.
19. Lemoine, F., Y. Antoine, M. Wolff, and M. Lebouche, *Simultaneous Temperature and 2d Velocity Measurements in a Turbulent Heated Jet Using Combined Laser-Induced Fluorescence and Lda.* Experiments in Fluids, 1999. **26**(4): p. 315-323.
20. Seuntiens, H.J., R.N. Kieft, C.C.M. Rindt, and A.A. van Steenhoven, *2d Temperature Measurements in the Wake of a Heated Cylinder Using Lif.* Experiments in Fluids, 2001. **31**(5): p. 588-595.
21. Coolen, M.C.J., R.N. Kieft, C.C.M. Rindt, and A.A. van Steenhoven, *Application of 2-D Lif Temperature Measurements in Water Using a Nd : Yag Laser.* Experiments in Fluids, 1999. **27**(5): p. 420-426.
22. Hishida, K. and J. Sakakibara, *Combined Planar Laser-Induced Fluorescence-Particle Image Velocimetry Technique for Velocity and Temperature Fields.* Experiments in Fluids, 2000. **29**: p. S129-S140.
23. Ross, D., M. Gaitan, and L.E. Locascio, *Temperature Measurement in Microfluidic Systems Using a Temperature-Dependent Fluorescent Dye.* Analytical Chemistry, 2001. **73**(17): p. 4117-4123.
24. Lakowicz, J.R., *Principles of Fluorescence Spectroscopy*. Second ed. 1999, New York: Kluwer Academic/Plenum Publishers.
25. Harnly, J.M. and R.E. Fields, *Solid State Array Detectors for Analytical Spectrometry.* Applied Spectroscopy, 1997. **51**(9): p. A334-A351.

Chapter 3: System Design and Troubleshooting

3.1 Introduction

A fluorescence-based thermometry instrument has three major components: the excitation source and optics, the detection device and optics, and the fluorescent probe. Chapter 2 defined the spectral considerations that were needed in making a choice for a fluorescent probe. The ratiometric approach to measuring fluorescence was adopted and a mathematical treatment was developed that allows the use of a pair of molecular probes with overlapping fluorescence emissions. The final choice centered on the temperature sensitive probe, Rhodamine B, and the temperature insensitive reference probe, Rhodamine 110. The relative merits of the major technologies for excitation and detection of fluorescence were considered and the laser and CCD camera were chosen based on their suitability to imaging in 2D. In this chapter, we will focus on the design of the fluorescence thermometry instrument along with the major difficulties encountered in its implementation. The major design issues in the selection of the excitation source optics and the detector optics are discussed. The use of fluorescent molecular probes introduces some new issues concerning the effects of concentration, photobleaching, and wall adsorption of the probes. The change from the Rhodamine B probe to Dextran Labeled Rhodamine B is discussed along with the major issues concerning image processing used to process the fluorescence images.

3.2 Basic Design: Planar Laser Induced Fluorescence

The final goal of the fluorescence thermometry instrument is the measurement of temperature in a microwave heated sample. Microwave heating is a volumetric process, and to fully understand it, we need to make temperature measurements in 3D. One approach to 3D measurements is to record successive 2D images in different planes and assemble the "slices" into a whole 3D picture. The starting point for such a 3D image is a 2D image confined to a narrow plane. The simplest method to isolate fluorescence to a plane is to spatially isolate the

excitation light in the sample cell to a plane. As described in Chapter 2, the laser is well suited to spatial control of light because its light is collimated. The laser beam as it leaves the laser can easily illuminate a single line, which, with a single cylindrical lens can be transformed into a plane. A cylindrical lens expands light along a single axis. The result is an isosceles triangle with its angle defined by the focal length of the lens and its width defined by the beam diameter. The beam is directed into a sample and a camera placed orthogonal to the illumination plane captures fluorescence emission patterns. A schematic of such a setup is shown in Figure 1 and this technique is called planar laser induced fluorescence, or PLIF.

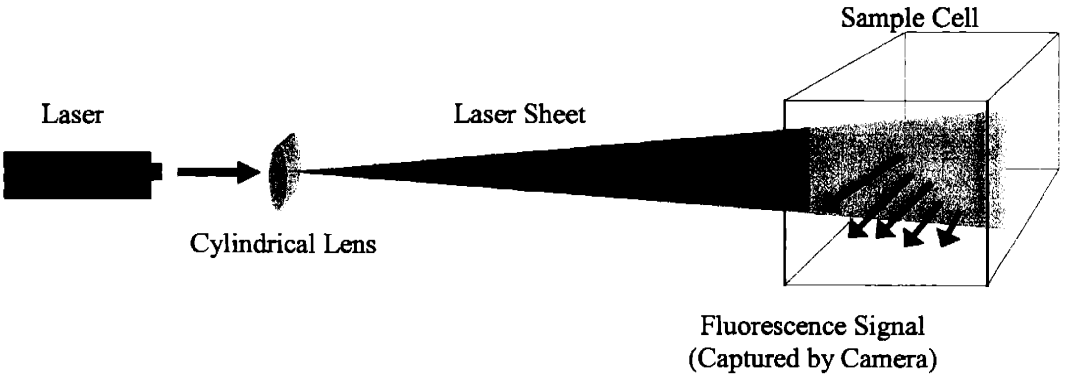

Figure 13: A generalized Planar Laser Induced Fluorescence (PLIF) setup.

There are many variations on the general PLIF setup which incorporate other optical elements to better control the beam shape. One of the most common additions is a second cylindrical lens. The second lens is used to collimate the light after the beam has expanded to desired height. The collimation stops the expansion and the sheet is now rectangular rather than triangular. The second collimation has two main purposes, first, to flatten the spatial power distribution along the height and second, to maintain the power over longer distances. With a single cylindrical lens, the laser beam expands indefinitely, thus there is expansion as the laser beam travels through the sample and the laser illumination is not spatially uniform. Collimating light produces an even power distribution in the sample, assuming that the sample absorbs an insignificant amount of light. In some applications, the laser optics must be located some distance from the sample. In these designs an indefinite expansion would result in a beam larger than the sample, wasting laser power. Collimating the laser light to sample size would spatially confine all the power and reduce power requirements. PLIF has been extensively used in examining flames[1-3], jets[4-6], and other fluid flows and is a powerful technique for examining

cross-sections of samples. The simplicity of PLIF and it's applicability to 2D and 3D imaging makes it a good choice for the basic design of an imaging fluorescence thermometry instrument. Although the PLIF appears simple in design, there are many design issues that arise from the characteristics of the laser beam and the specific challenges of detecting the fluorescence. In the following two sections, we discuss the major design considerations in the excitation and detection components and the trade-offs involved in the decisions made for our particular instrument.

3.3 The Excitation Component

3.3.1 Beam Quality

The ideal excitation source should have a narrow bandwidth and high uniformity in space and time. A laser fulfills the spectral purity requirement, and it is possible to achieve some degree of uniformity in space and time. A narrow band of excitation wavelengths simplifies blocking the excitation from the detector and allows better control of excitation-emission overlap. The advantage of a uniform illumination lies in its effect on the signal to noise ratio (S/N). The most accurate measurements are made when the S/N ratio is high and this occurs when the fluorescence signal is high. While the detector component does have a direct effect on the S/N ratio, noise in the excitation component will also affect the S/N ratio.

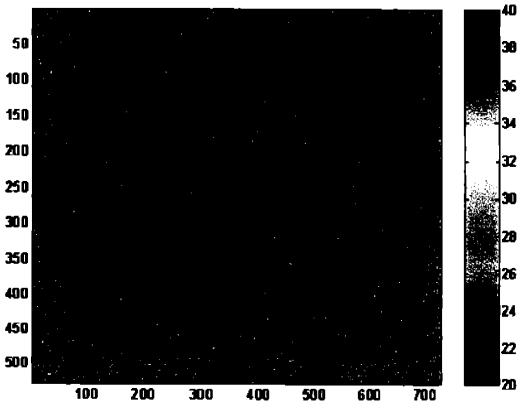

Figure 14: Fluorescence thermometry image of a constant temperature sample at room temperature.

The excitation effect can be the result of actual noise in the intensity of the radiation or due to constant spatial variations in the strength of the excitation beam in the sample. For our application, if we assume that the noise in the laser is spatially constant, the error will be determined by the spatial uniformity of the illumination. A good example of the effect is shown in Figure 14 and Figure 15. The image in Figure 14 is of a sample at a uniform temperature. A cursory visual inspection leads to the conclusion that the noise is uniform. However, if we plot the standard deviation of the columns and rows, the conclusion from our visual observation is clearly not true.

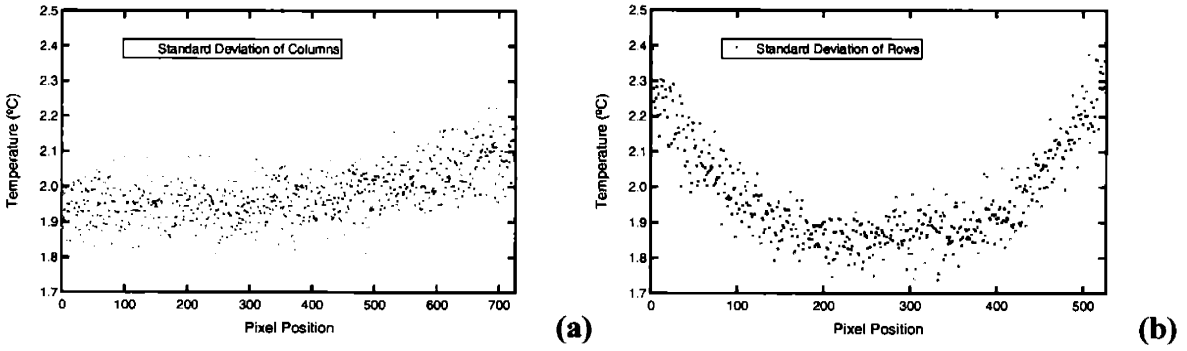

Figure 15: Standard deviation plot of columns (a) and rows (b) for the fluorescence thermometry image in Figure 14.

In Figure 15a the standard deviation of the temperature in each column is plotted, and in Figure 15b the standard deviation of temperature in each row. These plots reveal the error in each axis. For this sample, the laser enters from the left. In Figure 15a, the standard deviation of each column increases as laser travels through the sample. Clearly, the absorption of the laser light does have an effect, reducing the S/N by decreasing the fluorescence signal excited. In Figure 15b, the standard deviation of each row has a parabolic shape, which reflects the power distribution along the height of laser beam, which is the beam profile. This shape is a characteristic of laser illumination. Laser beams operate in different Transverse Electro-Magnetic or TEM modes, and these modes have differently shaped beam profiles. The most desirable shape for a laser profile is a simple Gaussian which is the TEM_{00} mode. Flattening a laser beam profile is simple to achieve with the TEM_{00} mode. The Gaussian is expanded and an aperture is used to cut off the edges and only allow the central portion to pass. Multiple expansions can be done to increase the flatness, however this comes at a significant cost in power. Ultimately a trade-off between S/N, illumination area and power has to be made.

3.3.2 The Sample Cell as an Optical Component

In the preceding section we considered the properties of our excitation source, the laser, on fluorescence measurements. However there is another significant factor that affects the beam besides its intrinsic characteristics. The laser beam must pass through the walls of an optically transparent sample cell. Although, it would seem that the criterion of optical transparency would be enough, there are more subtle optical criteria to consider. In a general fluorimeter setup, as shown in Figure 16, the primary design constraint on the sample cell is that it has to have two clear optical faces at right angles to allow the excitation to enter and the fluorescence to be detected.

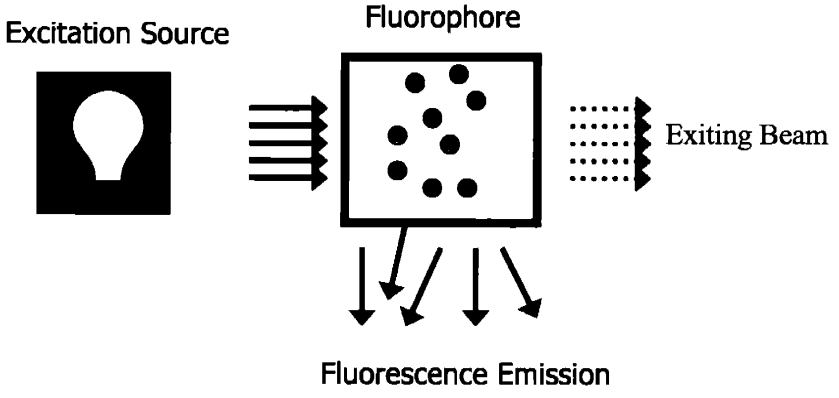

Figure 16: A drawing of the major components of a general fluorimeter

With our choice of a laser as the excitation source, an additional constraint is that a clear exit path is needed for the laser. The laser beam is sufficiently powerful that scattered laser light from an opaque surface will excite fluorescence outside of the illumination plane, and thus add to the noise in the form of a background signal. In the following sections, we will discuss two major problems that arise from the sample cell: optical defects, and the formation of etalons.

3.3.2.1 Optical Defects

The accuracy of optical measurements depends in large part on the absence of obstructions in the optical path. Despite all efforts, it is inevitable in optical systems to acquire data with some defects, though the defects do not necessarily invalidate all of the data. Imaging

systems acquire spatial information and are more sensitive to optical defects in both the excitation and detector optical paths compared to 1D systems which take an average over the entire detector. While a ratiometric measurement can compensate for small optical defects, large differences in signals cannot be compensated for because of the differences in S/N of the disturbance compared to that of the rest of the sample. An example of optical defects in the data is shown in Figure 17.

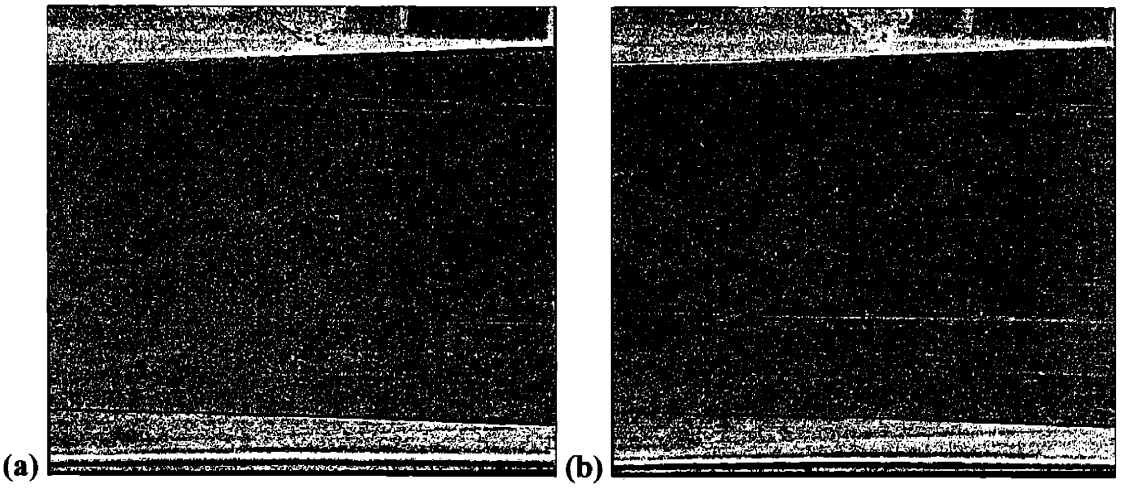

Figure 17: Fluorescence thermometry images of a constant temperature sample at (a) z-position +5mm (b) z-position +10mm.

These two images show PLIF images that have been transformed into temperature data of two separate planes, separated by 5 mm, in a sample cell at a constant temperature. Although distance between the planes is small, there is a substantial difference in the images. These two images show examples of both excitation and detector component optical defects. The excitation component defect is the obvious streak in Figure 17b. The clue that marks this as an excitation component defect is that it follows the laser beam path. This suggests that a bubble, or other occlusion, has disrupted the beam path. Unusual measurements that follow a laser beam path are likely to be an optical defect rather than a real measurement. In addition, a streak is physically unlikely in the context of the experiment. The detector component defect is very hard to detect and is shown, magnified in Figure 18. This defect is a constant spot in the lower right quadrant which appears in both images, thus marking it as a detector defect. Though a spot does not have

the obvious unphysical characteristic of the streak in Figure 17b, the repetition of the spot in the same location is physically unlikely, and thus it is probably an optical defect.

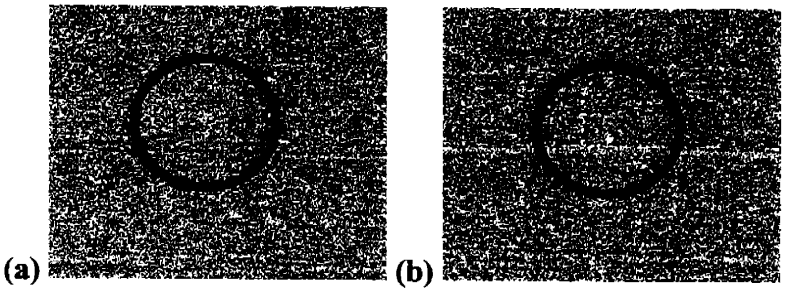

Figure 18: Magnified view of lower right quadrant of a pair of constant temperature images at different z-axis positions, showing constant defect (a) From Figure 17a (b) From Figure 17b.

While some wide ranging optical defects may invalidate an entire set of data, in 2D imaging, many defects are spatially limited and do not invalidate the entire image. Optical defects can affect either the excitation or emission component of the fluorescence thermometry instrument and specific clues to confirm their origin can be found depending on the component affected. These localized defects can then be safely ignored and the remaining data preserved.

3.3.2.2 The Etalon

As discussed in section 3.3, for better S/N it is advantageous to have a uniform illumination across the sample.

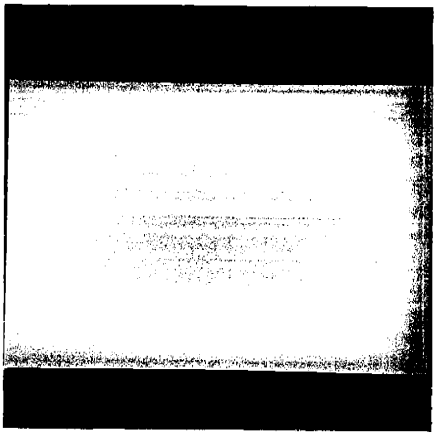

Figure 19: Fluorescence image showing line pattern noise in the laser beam from an etalon formed by sample cell wall

This can be achieved by the collimation of the laser beam after the initial expansion, using a second cylindrical lens, to parallelize the beam with the bottom of the sample cell. The resulting illumination should be equal, left to right, excluding differences due to adsorption by the sample. However, if a collimated beam strikes a plane of glass, an optical structure, an etalon, can be formed which causes spatial variations in the beam intensity as shown in Figure 19. We expect to see a fluorescence pattern consistent with the beam profile, however, what we see is an image streaked with lines along the path of the laser. These lines are caused by constructive and destructive interference, and originate from the interaction of the beam with sample cell wall. The two surfaces of the cell wall form an etalon, which is an optical structure that is formed with two parallel partially reflecting surfaces. When a collimated beam passes through an etalon, the partial reflection at each surface causes a small percentage of the beam to be reflected back in the direction of the beam, causing interference effects, which appear as alternating series of higher and lower intensity zones. The precise line pattern depends on the incident beam characteristics, angle of incidence, the reflectivity of the surfaces and the distance between the surfaces. Etalons are not a problem for light sources, such as lamps, that are not collimated. The light from a lamp strikes an etalon from many random angles of incidence so that the interference effects are limited. One solution to reduce the effect of the etalon is to mimic the lamp by decreasing the collimation of the light. Instead of using a second cylindrical lens to collimate the light into a rectangular shape, a longer focal length cylindrical lens is used with a shallower angle of expansion.

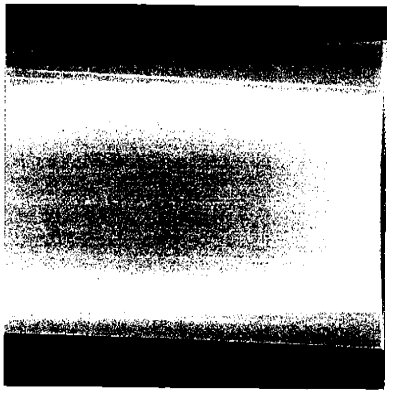

Figure 20: Fluorescence image with reduced line pattern noise from the etalon as a result of a slight expansion of the incident laser beam.

With the slight angle against the sample cell wall, the resulting interference lines occur at much higher frequencies as shown in Figure 20 which has a considerably smoother profile. The line

structure is still apparent but the reduced amplitudes of the interference pattern will increase the S/N for the whole image.

The sample cell is an optical component in the excitation path and therefore its interaction with the excitation beam must be thoroughly considered. Etalons can form whenever a collimated beam travels through two parallel surfaces. In the fluorescence thermometry instrument design, we have chosen to mitigate the effects of the etalon by a small expansion of the laser beam, which markedly reduces the interference pattern at a small cost to beam uniformity in the sample.

3.4 The Detector Component

3.4.1 Introduction

The detector component forms the other half of the excitation and detector couple that is a part of fluorescence measurements. The detector component can be split into two parts, the actual photon detector, and the optics that isolate the fluorescence signal from the background noise. The prominent photon detector technologies used in fluorescence detection were discussed in Chapter 2 and the CCD camera was selected as the technology to be applied to the fluorescence thermometry instrument. The need for capturing images made CCD technology the obvious choice. In this section we will discuss some of the trade-offs in choices between different CCD cameras. The fluorescence separation optics are critical in determining the success of the fluorescence thermometry instrument and depends greatly on the fluorescence spectra of the probes. In section 3.4.3 we discuss the choices and troubleshooting that were used in picking a filter combination for separating Rhodamine B and Rhodamine 110 fluorescence.

3.4.2 The CCD Camera

Selecting the camera model is a task that requires balancing trade-offs between performance and cost. The issue of cost is a detail that is ever changing and an analysis of the cost of a camera is best left to the individual application. However, it is important to note that there is no perfect camera available, whatever the price. From a practical standpoint, the most

important criterion for a camera is its sensitivity. CCD camera sensitivity is characterized by its quantum efficiency (QE) which reflects the efficiency of conversion of photons to electrons. This is a wavelength specific characteristic and it is important to choose a camera that has a high QE in the wavelengths for the fluorescence of all probes that will be used. The second consideration is the trade-off between resolution and speed. CCD cameras are limited in the rate at which the charge on the CCD can be moved off the CCD chip (readout), measured, and converted by the analog to digital converters (ADC). At high resolutions, more data need to be moved off the CCD, leading to a reduction in the number of frames per second (FPS) that the CCD camera can capture. Two technologies are commonly employed to help with this trade-off; on-chip binning and frame transfer CCDs. On-chip binning is a technique that treats groups of pixels as a single pixel, combining their charge before sending it to the ADC. The binning gives the camera more flexibility, giving it two modes, a slower high resolution mode, and a faster, low resolution, binned mode. The other technology, frame transfer CCDs, splits a CCD chip in half, with one half covered so that no light sensitive surface is exposed, while the other section is exposed normally. When an image is captured in a frame transfer CCD camera, the image is first shifted to the blanked area, and then read out. This allows the camera to start exposure for the next frame immediately after transferring the charge to the blank area. Because the readout and ADC are significantly slower than inter-chip charge transfer, the camera can quickly do the transfer, and then begin the next exposure while the readout is performed in parallel. This technique speeds up the overall camera capture rate.

3.4.3 Optical Filter Selection

One of the greatest technical challenges in fluorescence measurement of two probes is the separation of the fluorescence spectra. The combined spectrum may appear to have peaks that are easily distinguished by eye, but in practice the separation can be far more difficult. The simplest and most versatile tool for separating wavelengths of light for imaging systems is the optical filter. Although exotic systems, such as imaging monochromators exist, they are designed for multi-track spectroscopy, expensive and not suited to reproducing images. There are many different filter types, but the most common and widely used types are the colored glass filter and the interference filter. The colored glass filter is a piece of glass that has been doped

with an additive to change its spectral response. Interference filters are made of multiple layers of material that cause multiple reflections and cancellations so that only light in a particular wavelength range is transmitted. Filters can be broadly categorized by the shape of their transmittance curve. The three categories are band-pass, short-pass and long-pass. Band-pass filters allow transmittance in a group of adjacent wavelengths; short-pass filters transmit all wavelengths shorter than a particular cut-off wavelength, while long-pass is the opposite of a short-pass filter, transmitting only those wavelengths longer than the cut-off wavelength.

The process of designing a fluorescence separation strategy begins with an examination of the fluorescence spectra. Shown in Figure 21 are the fluorescence spectra of Rhodamine B and Rhodamine 110 at the highest concentrations possible with the transmission of the excitation beam still above 95%. The fluorescence spectra have significant overlap, but in Chapter 2 we have shown that the emission-emission overlap can be dealt with mathematically. However, the Rhodamine 10 peak still needs to be separated from the Rhodamine B peak to provide the two signals needed for ratiometric imaging. The spectra in Figure 21 were generated using 488 nm light, one of the two high power laser lines available in an Argon-Ion laser. The other laser line available from an Argon-Ion laser is 514 nm. The superposition of the laser lines and the absorption spectra for Rhodamine B and Rhodamine 110 is shown in Figure 22.

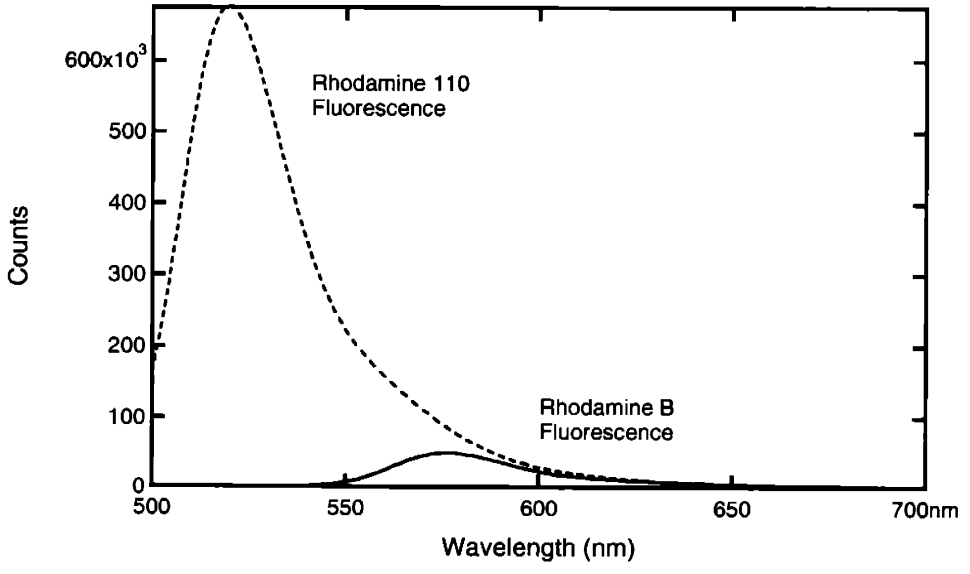

Figure 21: Fluorescence Emission Spectra Overlap of Rhodamine 110 and Rhodamine B

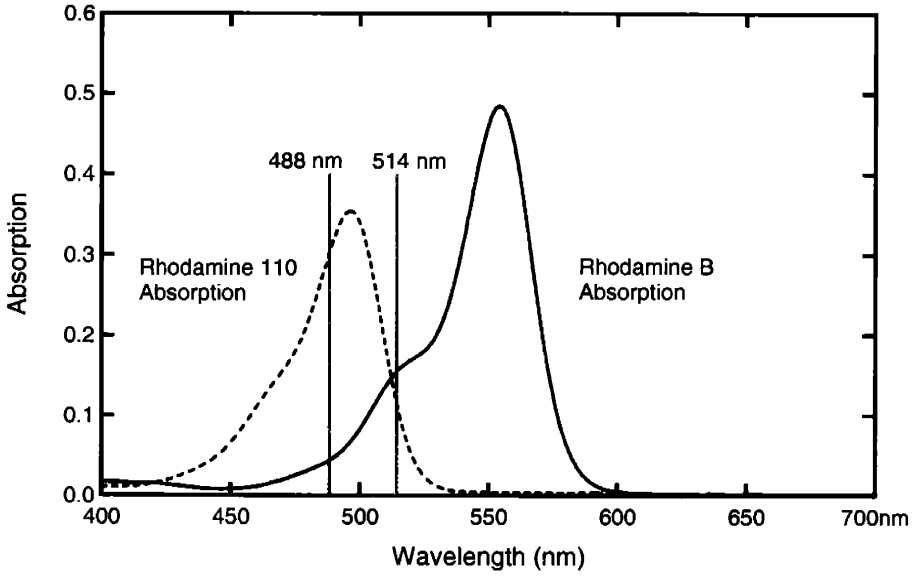

Figure 22: Absorption Spectra of Rhodamine 110 & Rhodamine B

A shift to 514 nm would dramatically increase the Rhodamine B fluorescence and decrease Rhodamine 110 fluorescence. However, the Rhodamine 110 fluorescence peak is at 520 nm, which is too close to 514 nm to separate. It is likely that light scattering from the 514 nm light would be indistinguishable from the Rhodamine 110 fluorescence, and because the excitation is far stronger than fluorescence, this would remove our ability to detect Rhodamine 110 fluorescence.

The concentration can be adjusted to compensate for differing responses of the probes; however, this is limited by the sensitivity of the detector and absorption of the laser light through the sample. Because some filters have extremely low transmissions, the mismatch in peak intensities may not exist if the Rhodamine 110 peak filter transmits significantly less light than the filter used for Rhodamine B. A final option is to increase excitation intensity, although increasing excitation also increases the photobleaching rate.

One method for separating Rhodamine B and Rhodamine 110 fluorescence was developed by Sakakibara[7]. A schematic of their detector component layout is shown in Figure 23.

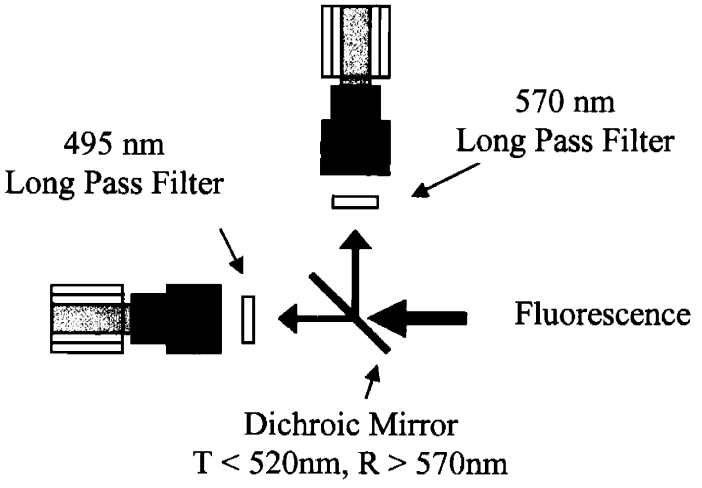

Figure 23: Optical Setup for separation of Rhodamine 110 fluorescence peak from the Rhodamine B fluorescence peak designed by Sakakibara & Adrian[7]

The design by Sakakibara uses a dichroic mirror to split the fluorescence signal into two groups of wavelengths. Wavelengths shorter than 520 nm are transmitted into one camera and wavelengths longer than 570 nm are reflected into a second camera. The advantage of a dichroic mirror is that it splits the wavelengths without absorbing, thus providing maximum signal in the appropriate region to each camera. Both the 495 nm and 570 nm long pass filters in this design are colored glass filters. (Schott GG-495 & OG-570).

There are two problems with the design by Sakakibara. The first problem is the choice of the dichroic mirror. The dichroic mirror was a custom piece from CVI Laser Corporation that transmits lower wavelengths and reflects higher wavelengths. Transmission of lower wavelengths and reflection of higher wavelengths is a difficult combination to manufacture and has unpredictable optical characteristics. The second issue is the choice of a colored glass 495 nm long pass filter. A laser beam is a very intense light source and even the scattered light can be as bright as the fluorescence of the probes. Unfortunately, colored glass filters typically do not have very strong blocking outside their transmission regions, and the proximity of the 495nm long pass filter to the laser excitation line of 488 nm exacerbates this problem as shown in Figure 24.

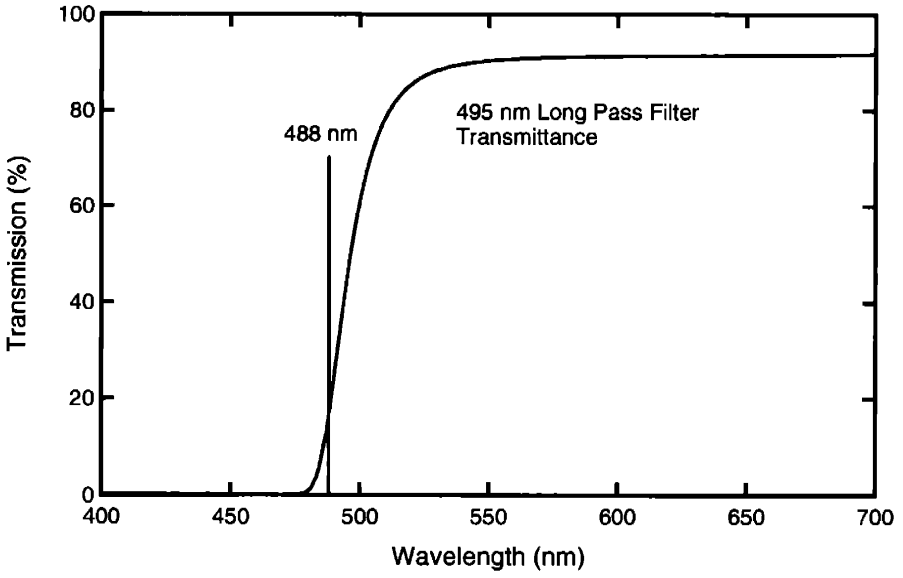

Figure 24: Transmission of 495 nm long pass filter compared with Argon-Ion laser line at 488 nm

The 495 nm long pass filter transmits 15% of the 488 nm laser line, which guarantees that the camera will detect the scattered light from the laser in addition to Rhodamine 110 fluorescence.

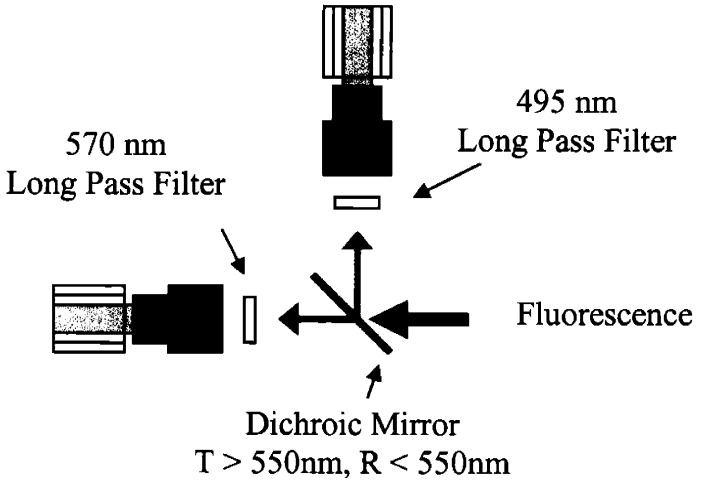

Figure 25: Optical layout of Sakakibara & Adrian adapted to incorporate a reversed dichroic mirror.

We tested the filter set used by Sakakibara in the configuration shown in Figure 25. The dichroic mirror was substituted to a stock dichroic from Omega Optical (560DRLP) that approximates the transmission and reflection ranges of the custom dichroic mirror used by

Sakakibara. Rhodamine B has negligible fluorescence below 500 nm which makes it a good test of the separation of fluorescence spectra from background scattering. Figure 9 shows the images from a test sample of water with Rhodamine B.

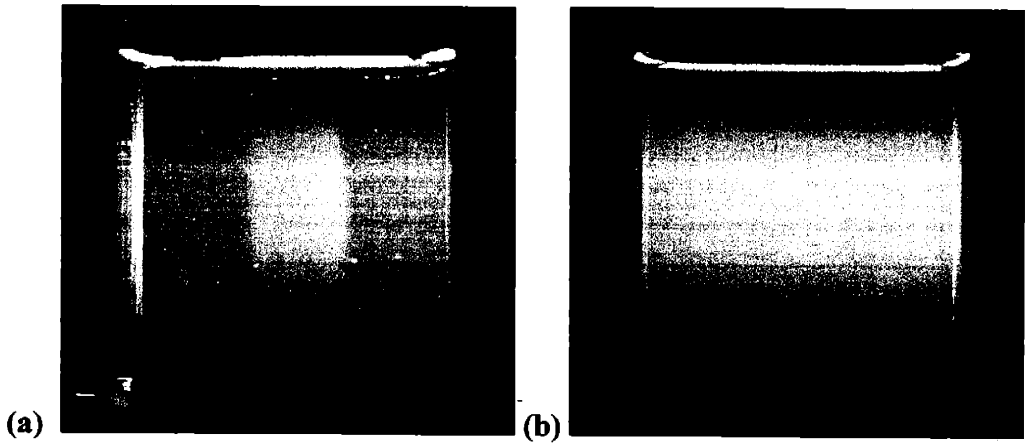

Figure 26: Demonstration of the filter and dichroic performance on a solution of Rhodamine B in water (a) 495 nm long pass filter, dichroic reflection (b) 570 nm long pass filter, dichroic transmission.

Figure 9a clearly has a large signal, indicating that there is substantial scattering from the 488 nm excitation laser beam leaking through the 495 nm long pass filter. Anecdotally, a black mounting screw can be seen clearly in the image, which is unlikely to be visible from reflected fluorescence from Rhodamine B.

The optical layout that addresses both limitations in the setup by Sakakibara is shown in Figure 27. The 520 nm interference filter is used to isolate Rhodamine 110 fluorescence. Interference filters have high blocking of wavelengths outside of the transmission range and the transmission does not overlap with the 488 nm laser line. (Figure 28) The 520 nm interference filter transmittance coincides with the Rhodamine 110 fluorescence peak; however, the narrow bandwidth reduces the total fluorescence that is transmitted. Thus, the Rhodamine 110 concentration will be higher with this optical setup compared to the design by Sakakibara. The new optical setup shows good separation of the Rhodamine B fluorescence to a single camera. (Figure 29)

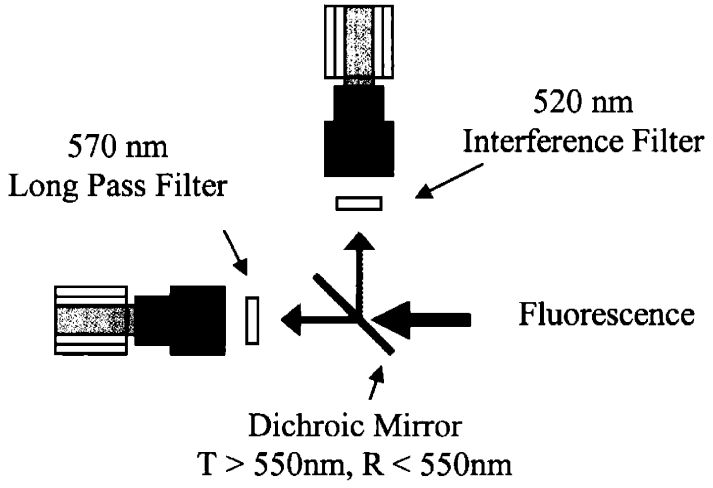

Figure 27: Optical layout with stock dichroic mirror and filter combination that blocks scattering from the laser.

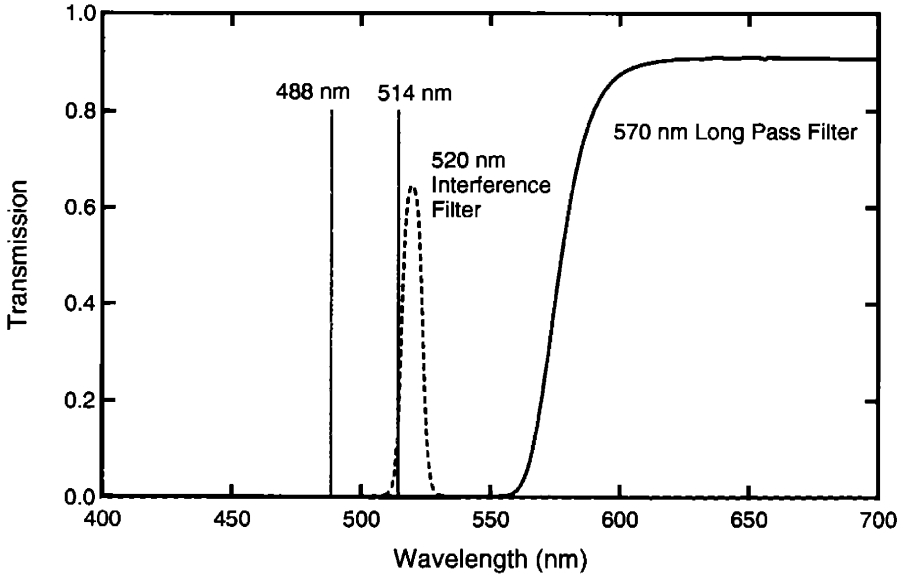

Figure 28: Transmittance curves for 520 nm interference filter and 570 nm long pass filter plotted with the Argon-Ion laser lines.

Virtually no signal is detected by the 520 nm filtered camera, in stark contrast to the images shown in Figure 26. Rhodamine B has a very small amount of fluorescence in the 520 nm region and we can verify that all the light scattering is blocked by examining the structure of the image from Figure 29a.

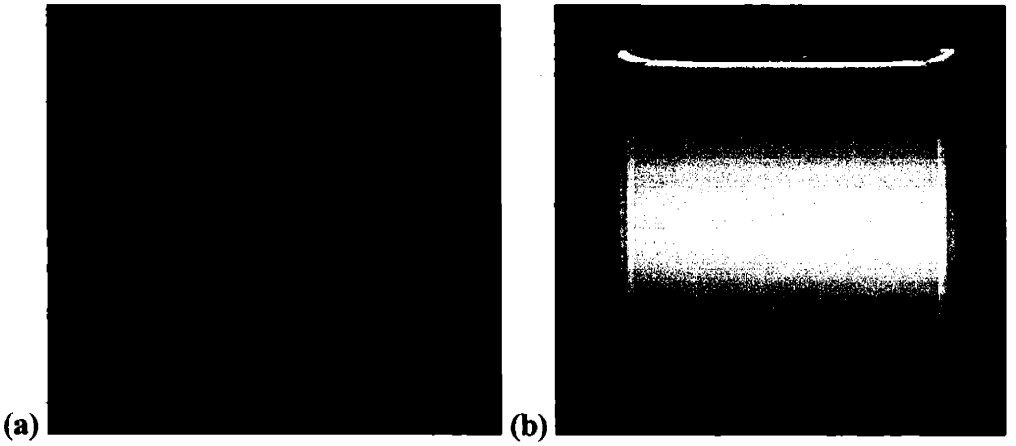

Figure 29: Demonstration of the filter and dichroic performance on a solution of Rhodamine B in water (a) 520 nm interference filter, dichroic reflection (b) 570 nm long pass filter, dichroic transmission.

Rescaling the color scale to a much smaller range produces the image shown in Figure 30. Figure 30 has more noise than Figure 29b because the signal levels are much lower, but otherwise the fluorescence looks similar. Notably, screw is not visible, empirically demonstrating that only fluorescence is detected. The 520 nm filter blocks light scattering from the laser while isolating 520 nm wavelength band where Rhodamine 110 fluoresces.

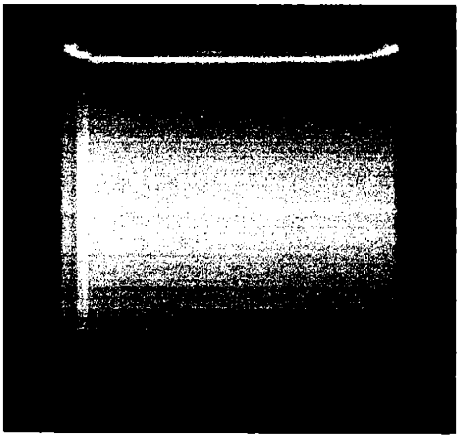

Figure 30: 520 nm interference filter image of a Rhodamine B solution rescaled to show structural details in the fluorescence.

In Figure 31, the results are shown for a solution of Rhodamine 110 in water. As expected, Figure 31a shows a large increase in signal compared to the Rhodamine B experiment, indicating that Rhodamine 110 fluorescence has been detected.

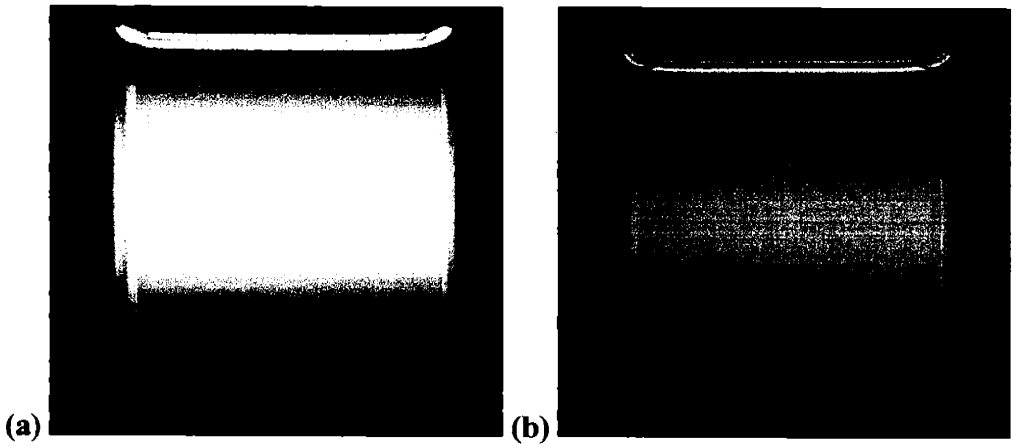

Figure 31: Demonstration of the filter and dichroic performance on a solution with only Rhodamine 110 (a) 520 nm interference filter, dichroic reflection (b) 570 nm long pass filter, dichroic transmission.

There is considerable fluorescence signal in the 570 nm image, as expected from the emission-emission overlap between the Rhodamine 110 tail and the Rhodamine B peak. The separation of Rhodamine B fluorescence peak from the Rhodamine 110 fluorescence tail cannot be done optically, and instead will be resolved mathematically as described in Chapter 2.

Separation of fluorescence peaks in a sample with multiple molecular probes is critical to making ratiometric fluorescence measurements. Careful attention must be paid to the choice of optical filters used in order to avoid light scattering from the excitation laser beam and achieve separation of the fluorescence. We have shown how a dichroic mirror and optical filter system can be used successfully to isolate the Rhodamine 110 peak from the Rhodamine B fluorescence. The Rhodamine B peak is superimposed on the Rhodamine 110 tail and thus cannot be resolved optically.

3.5 Optical Layout

In the preceding two sections, we have described in detail the design of the excitation and detector components of the fluorescence thermometry instrument. The final optical design uses an excitation system based on PLIF and a dual CCD camera detector component. The detector component uses a combination of filters and a dichroic mirror to separate the fluorescence

emissions of Rhodamine B and Rhodamine 110. A schematic of the complete imaging fluorescence thermometry system is shown in Figure 32.

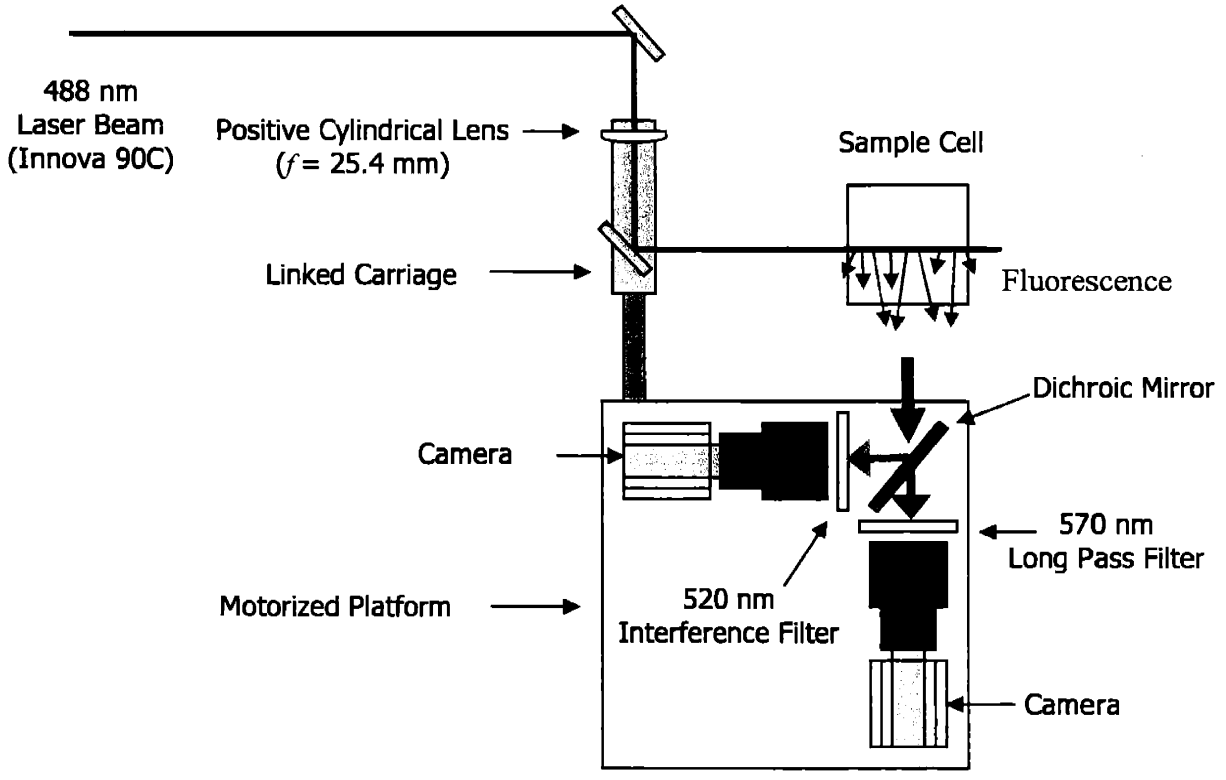

Figure 32: Schematic Diagram of 3D Imaging Fluorescence Thermometry Instrument

This particular instrument is designed to demonstrate the general principles of temperature measurement using PLIF in a setup that provides temperature control, and provide diagnostics for unanticipated difficulties in the implementation of this approach for remote temperature sensing. The instrument is designed to measure temperature distributions in a liquid sample enclosed in an optically clear sample cell. The sample cell is a 5 cm open top cubic glass container with a capacity of 125 ml. It has four optically clear sides and rests on a water cooled/heated aluminum plate which is connected to a water bath. The measurement range used in tests ranges from room temperature to 60 °C. Room temperature was chosen as the starting temperature. The high temperature limit is the maximum temperature that the Rhodamine B temperature probe can measure. The two camera design is required for the referenced (ratiometric) approach to temperature measurement. In this approach, one camera monitors a temperature insensitive fluorescent probe to provide a reference for intensity fluctuations in the

laser beam. Two separate cameras (Qimaging Retiga 1300 with Optem 34-11-10 Macro Video Zoom Lens) were used, one for the emission peak of Rhodamine B (576 nm) and the other for the emission peak of Rhodamine 110 (519 nm). The fluorescence output is divided between the two cameras by a 550 nm dichroic mirror (Omega Optical 560DRLP). The dichroic mirror reflects wavelengths shorter than 550 nm into the Rhodamine 110 camera and passes wavelengths longer than 550 nm into the Rhodamine B camera. A simple 550 nm split is insufficient to completely separate the fluorescence emissions, so filters were placed in front of the cameras. The Rhodamine B camera has a 560 nm long pass filter (CVI Laser Corp. CG-OG-570-2.00-3) which passes all wavelengths higher than 560 nm and the Rhodamine 110 camera has a 520 nm (10 nm FWHM, Oriel 54351) interference filter which passes a 10 nm wide band centered at 520 nm. The beam was expanded by a BK7 plano-convex cylindrical lens (CVI Laser Corp. RCX-25.4-12.7-12.7-C) with a focal length of 25.4 mm. The laser illumination was provided by a Coherent Innova 90C argon-ion laser.

3.6 Fluorescent Probe Issues

3.6.1 Introduction

To this point we have focused on the technical aspects of the optical design of the fluorescence thermometry instrument. In this section, we will focus on particular issues that originate from the fluorescent probes, Rhodamine B and Rhodamine 110. The interaction of the fluorescent probes with the excitation beam, with themselves and with the sample container is discussed. Finally this section ends with a discussion on the change from Rhodamine B to Dextran labeled with Rhodamine B to address problems of surface adsorption.

3.6.2 Concentration Effects

Selecting a concentration to use for a molecular probe is a task that involves trade-offs. At high concentrations, molecular probes will absorb too much of the excitation light and therefore lower the S/N ratio across the sample. At low concentrations the detector may not have

sufficient signal and if there is sufficient signal, photobleaching may be detected and reduce the S/N ratio.

The first point to consider is whether the fluorescence at a particular concentration can be measured by the detector component. The concentration must be high enough that the detector can pick up the fluorescence signal. Next, the S/N must be considered, and the concentration must be further adjusted until the probes emit sufficient fluorescence to achieve the desired accuracy. The third point to consider is absorption of the excitation light by the molecular probes. Absorption can be modified in two ways: decreasing the concentration, or decreasing the path length the excitation beam travels through the sample. Both of these factors depend on the specific goals of the fluorescence instrument. Decreasing concentration potentially decreases S/N, and decreasing path length reduces the sample volume. Absorption of excitation light is not the only absorption that can create problems. Most fluorescent probes have a small Stokes shift, and thus have overlapping absorption and emission spectra. This is true for Rhodamine B, whose overlap of absorption and emission spectra can be seen in Figure 33. This overlap results in self-absorbance and at high concentrations can be significant source of absorption.

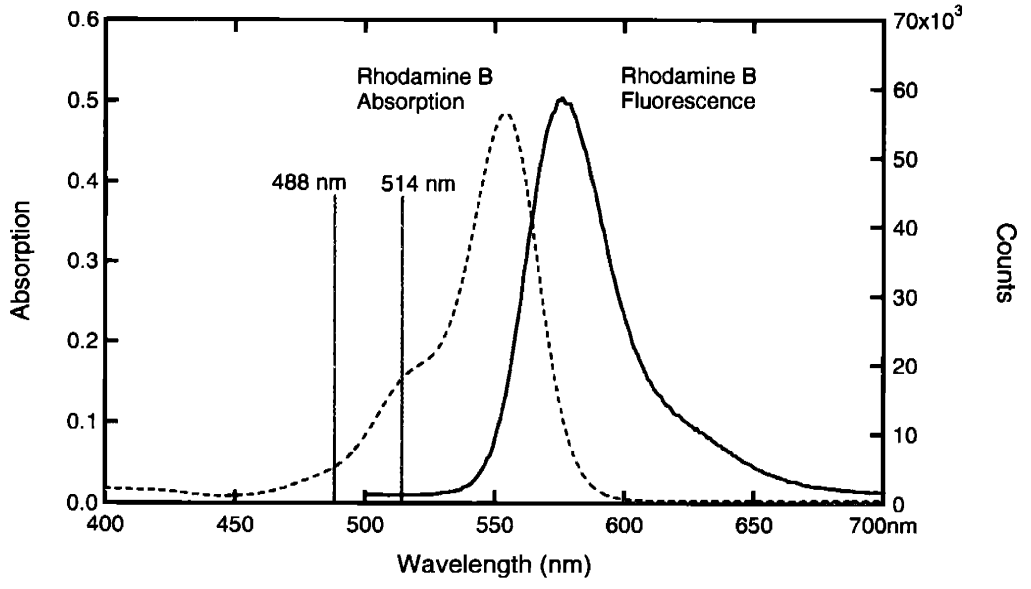

Figure 33: Rhodamine B absorption and fluorescence emission spectra

Additionally, at high concentrations, fluorescent species can also self-quench. This is a phenomenon where unexcited probe molecules interact non-radiatively to de-excite the excited molecule.

For the fluorescence thermometry instrument described in this thesis, the concentrations were chosen by maximizing the concentration for a combination of the probes for a 95% transmission of the excitation laser beam through the sample cell. The relative concentrations of the two probes were determined by taking the transmission of the optical filters and the QE of the cameras into account. The final relative concentrations were then adjusted to maximize the signal in each camera with an allowance for some headroom for errors in probe concentrations, laser power, and optical path changes.

3.6.3 Photobleaching

When fluorescent molecules are subject to an excitation radiation, they energize to an excited state. In this state, it is possible for the fluorescent probe to react with other species in the solvent and lose its fluorescing ability. This phenomenon is called photobleaching. The most common initiator of photobleaching is oxygen, and one common solution is to degas solutions before exposure. However oxygen does not significantly affect photobleaching of Rhodamines[8], which are generally much more resistant to photobleaching than most fluorescent species and are commonly used as laser dyes. In spite of this, Rhodamines will photobleach, and the rate depends on the intensity of the excitation radiation and the absorbtivity of the fluorescent probe at the excitation wavelength. In molecular probe applications it is desirable to minimize the concentration of the fluorescent probes to reduce interactions with the sample. However, reducing the probe concentration increases the detection of photobleaching by increasing the ratio of photobleached molecules to normal molecules. Ultimately, the best way of minimizing photobleaching is to reduce the exposure to the excitation source. This requires a careful balance of fluorescence signal intensity with the detector sensitivity. In the specific case of Rhodamine B and Rhodamine 110, the low concentration of Rhodamine 110 and its high absorptivity at 488nm combine to make Rhodamine 110 a perfect candidate for photobleaching detection. Figure 34 shows the problem of Rhodamine 110 photobleaching. The images in Figure 34 are

the difference between the first and last images of a 5 image sequence taken of a Rhodamine 110 sample at room temperature. The darker areas represent regions where the intensity of fluorescence in the fifth frame dropped relative to the first frame.

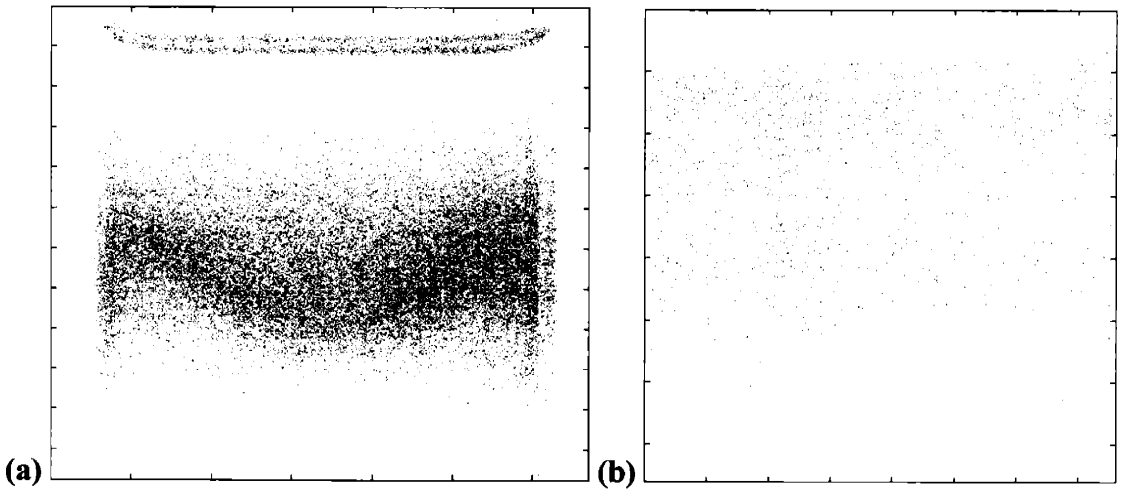

Figure 34: Photobleaching demonstration in a 5 image sequence of a sample of Rhodamine 110 in solution. Each images shows the result of Image 5 – Image 1 for (a) Continuous laser illumination (b) Illumination only during camera exposure time

In Figure 34a, the laser continuously illuminates Rhodamine 110 as images are taken at 1 Hz, while in Figure 34b the laser is timed to illuminate only during the 100 ms exposure time of the cameras. With continuous illumination, there is a significant decrease in the fluorescence output, on the order of 5-10%. The magnitude of decrease is in the same order as the temperature sensitivity of Rhodamine B, which is 2.3% per °C[7]. Clearly a 5-10% change in fluorescence intensity will greatly reduce the sensitivity of the fluorescence thermometry instrument. The final design of the instrument uses a high-speed shutter, with a response time of 1 ms, and electronics to trigger the shutter only during the actual exposure time of the camera. This combination effectively removed the photobleaching problem for Rhodamine 110. Rhodamine B showed no detectable photobleaching, due to its high concentration in the sample and low absorptivity at the excitation wavelength.

3.6.4 Wall Adsorption

We have seen that high probe concentrations present a number of difficulties. Arbitrarily low concentrations can offer difficulties as well. At low concentrations photobleaching is easier

to detect and disturbs the fluorescence measurement. Low concentrations also reduce fluorescence emissions and make more sensitive, and therefore more expensive, detectors a requirement. However, beyond these more obvious problems, there is the problem of surface adsorption of the molecular probes.

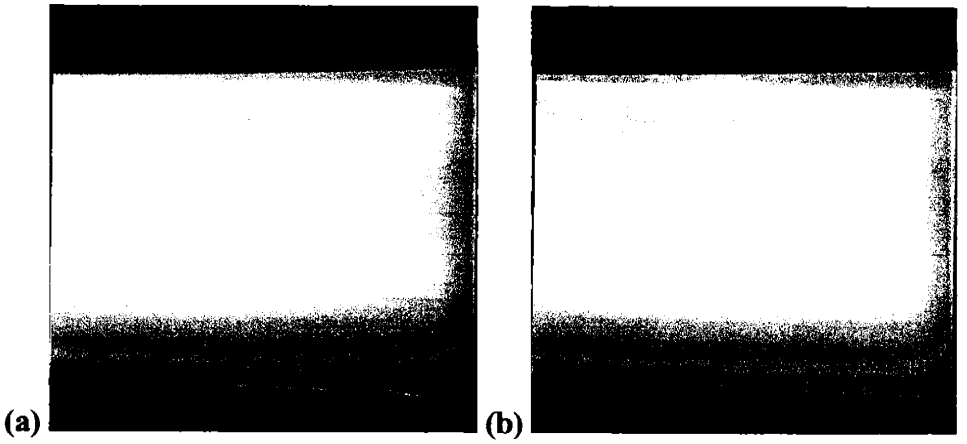

Figure 35: Adsorption differences in a heating experiment on a mixed sample. (a) Rhodamine 110 camera image shows no response to the heater at the top. (b) Rhodamine B camera image shows unphysical increase in fluorescence which corresponds to decrease in temperature.

Fluorescence measurements depend on a uniform concentration of probes in the sample and because the walls of a fluorescence cell can adsorb probe molecules, at low concentrations this absorption can distort the fluorescence measurements. Rhodamine B and Rhodamine 110 have very different adsorption characteristics and this is shown in Figure 35. In this experiment, the sample cell is heated by a cartridge heater located just above the laser illumination. The heater is inside an oil filled test tube made of glass. The images in Figure 35 show the fluorescence intensity observed shortly after activation of the heater. As expected, the Rhodamine 110 signal shows no significant response to the heating, owing to its small fluorescence change in response to temperature. Rhodamine B however shows an increase in intensity of fluorescence in patterns that extends from the vicinity of the heater. The increase in fluorescence intensity with the increase in temperature caused by the heater is opposite to the temperature response of Rhodamine B. The increased fluorescence is the result of a local increase in Rhodamine B concentration because of desorption from the surface of the test tube caused by the large temperature increase.

Surface adsorption can be tackled by modifying the surfaces to hinder adsorption or chemically change the probe molecule so that it doesn't readily adsorb to the walls. One chemical approach is to attach the probe molecule to a polymer that has a higher solubility than the probe itself. If the polymer is sufficiently large, the combined molecule will preferentially remain in solution. We tested a commercially available probe from Molecular Probes that is a composed of a Dextran polymer with a Rhodamine B label. The following section analyzes the suitability of the probe as a replacement for pure Rhodamine B.

3.6.5 Rhodamine B Labeled Dextran

Chemically binding a fluorescent probe to another molecule can often result in changes to the fluorescent properties of the probe. Many fluorescent probe molecules are specifically designed to exploit these changes in their properties upon binding. Once bound, the change in fluorescence is easy to distinguish from the background fluorescence of unbound probe molecules. In our application we need to ensure that the temperature response of Rhodamine B is unchanged when it is bonded to the Dextran polymer.

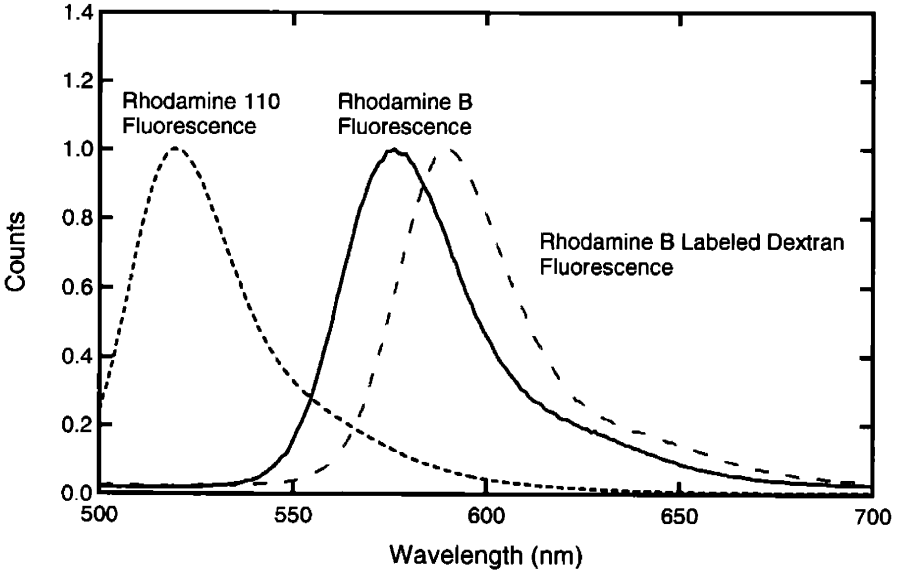

Figure 36: Overlaid fluorescence spectra for Rhodamine 110, Rhodamine B and Rhodamine B labeled Dextran

It is also important that the fluorescence spectrum is sufficiently similar so that the filters and dichroic mirror can remain unchanged. The Rhodamine B labeled Dextran used has a labeling density of approximately one Rhodamine B molecule per chain and a molecular weight of 10,000. The probe was used as received from Molecular Probes without additional purification. The spectrum in Figure 36 shows the peak normalized fluorescence of Rhodamine 110, Rhodamine B, Rhodamine B labeled Dextran. When bound to the Dextran, the Rhodamine B peak red-shifts from 576 nm to 590 nm, but otherwise retains the same shape. A similar shift is observed in the absorbance spectrum shown in Figure 37.

In the absorbance spectrum, the Rhodamine B absorbance peak shifts from 554 nm to 571 nm. As a result of the red-shift in the absorbance spectra, the 488 nm line of the Argon-Ion laser is even more weakly absorbed compared to Rhodamine B and the resulting fluorescence of Rhodamine B labeled Dextran 1/3 that of Rhodamine B. To compensate, the concentration of Rhodamine B labeled Dextran was tripled to accurately compare its temperature response with that of Rhodamine B. The spectra of Rhodamine B labeled Dextran is sufficiently similar that no changes need to be made to the excitation and detector component setup.

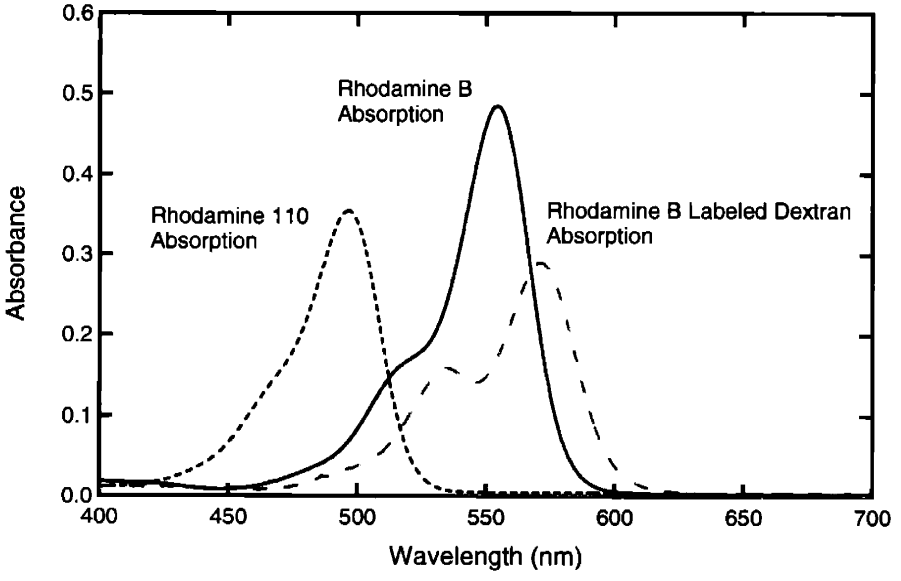

Figure 37: Overlaid absorption spectra for Rhodamine 110, Rhodamine B and Rhodamine B labeled Dextran

The temperature dependent behavior of Rhodamine B labeled Dextran is shown in Figure 38.

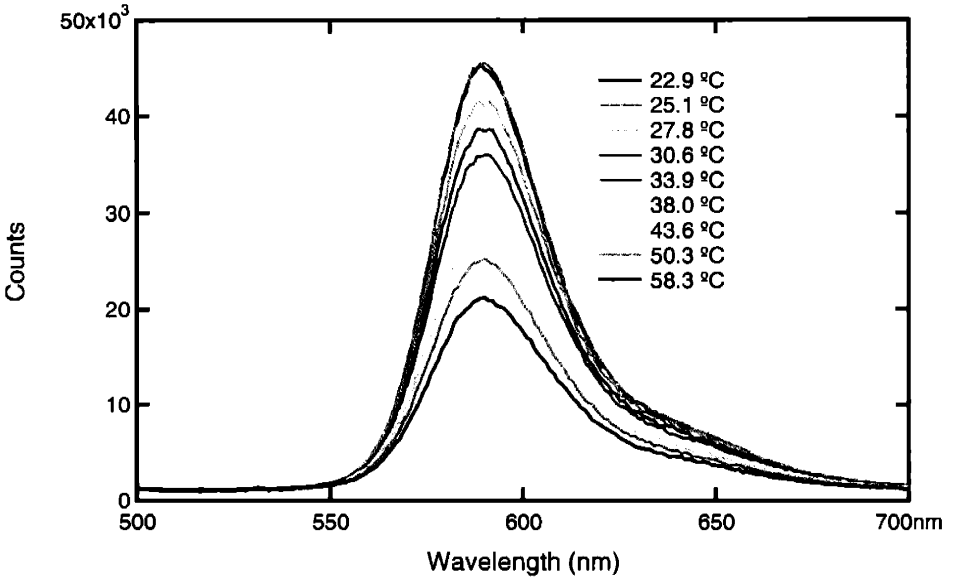

Figure 38: Rhodamine B labeled Dextran fluorescence response to temperature change

The temperature response of Rhodamine B labeled Dextran fluorescence is strong and similar to that of Rhodamine B. A comparison of the temperature response of Rhodamine B and Rhodamine B labeled Dextran is shown in Figure 39.

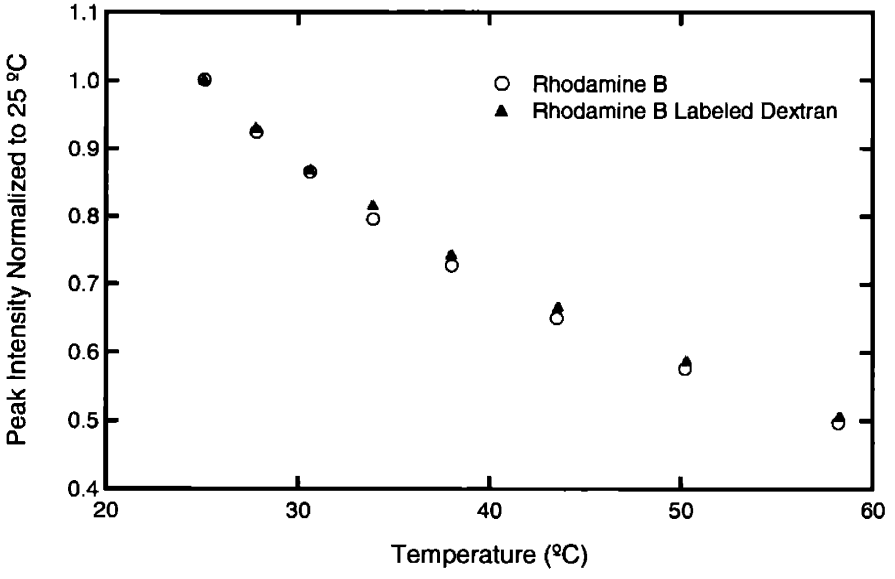

Figure 39: A comparison of the temperature dependent behavior of Rhodamine B and Rhodamine B labeled Dextran fluorescence.

Rhodamine B labeled Dextran tracks temperature almost identically to Rhodamine B and thus is a good replacement for Rhodamine B as a temperature probe.

Surface adsorption was the motivating issue for the Rhodamine B modification and the differences in the behavior of the two probes can be seen in Figure 40.

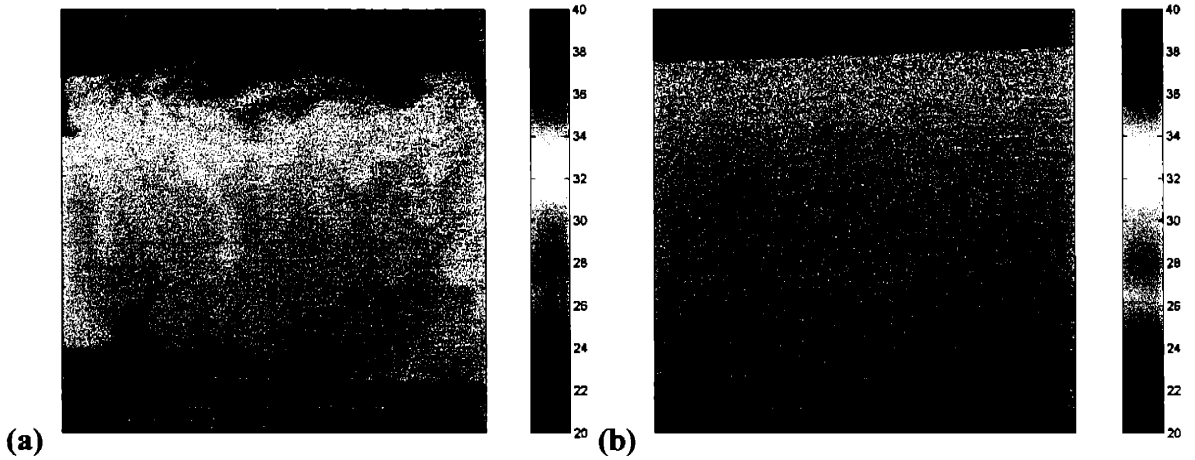

Figure 40: Surface adsorption and desorption phenomena seen in temperature images generated with (a) Rhodamine B as the temperature probe (b) Rhodamine B labeled Dextran as the temperature probe.

The sample cells were both heated from the upper left hand corner by a cartridge heater that is held above the laser illumination region. Figure 40a and Figure 40b appear drastically different. The lower left corner in Figure 40a shows non-physical temperatures dipping up to 10 °C below room temperature. This suggests that the temperature information is mixed with concentration driven flows which are disrupting the temperature measurements. The same experiment with Rhodamine B labeled Dextran in Figure 40b does not show the unphysical temperatures, or the dramatic structures. Based on this evidence, Rhodamine B labeled Dextran has reduced adsorption to the sample cell wall below levels that can significantly affect temperature measurement.

Rhodamine B labeled Dextran is a good replacement for Rhodamine B. It shows none of the adsorption and desorption problems of Rhodamine B and has a similar temperature response to Rhodamine B. Finally, it also has a fluorescence spectrum that is sufficiently similar to use

the same optical setup. Therefore we decided to switch to Rhodamine B labeled Dextran as our temperature probe.

3.7 Image Processing

3.7.1 Introduction

In chapter 2, we developed relations that derive temperature from ratiometric fluorescence data measured by a dual camera system. However these relations assume that the cameras are looking at the sample from exactly the same perspective. This requires an alignment process called image registration. In this section we will discuss how image registration works and some pitfalls encountered. The final section of this chapter covers the effect of binning images to achieve better temperature resolution by sacrificing spatial resolution.

3.7.2 Image Registration

When more than one camera is required to record events in a single sample the cameras need to be aligned so that a mapping can be established between the two cameras.

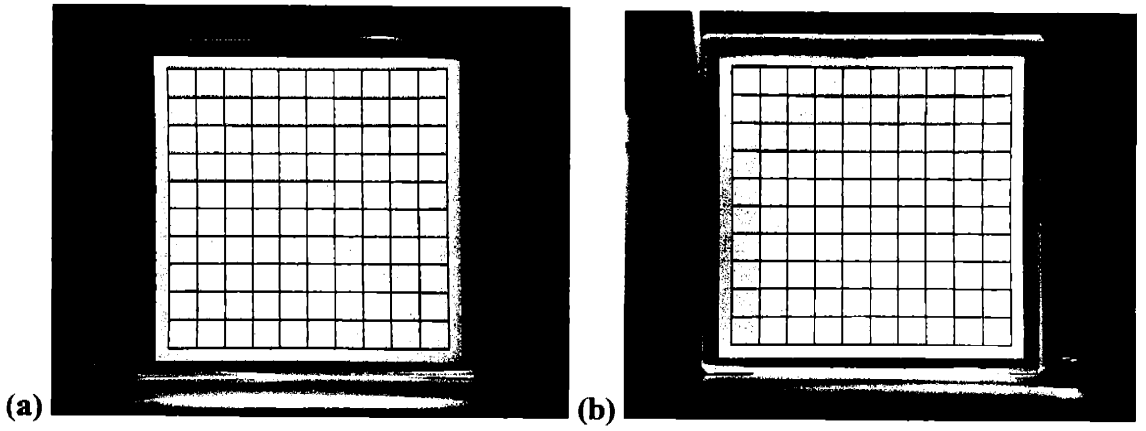

Figure 41: Registration test target images. (a) Reflected image from dichroic mirror. (b) Transmission image through dichroic mirror.

This process is known as image registration. The simplest approach is to optically align the cameras so that they record exactly the same scene. In practice, this is a difficult, and sometimes

impossible to accomplish. Generally it is possible to bring the cameras into a rough mechanical alignment, and then electronically process the data in each camera so that they are aligned with each other. The electronic alignment is handled by imaging a test target designed with identifiable points that could be recognized and mapped to the same points on the second camera. The images are processed by using a custom detection algorithm programmed in Matlab to find the crossing points of the gridlines. This program generates a list of positions in the coordinate space for each image that correspond to the same physical structures in actual test target. The points in image 1 can be mapped to points in image 2 by using an image registration algorithm. This algorithm generates a transformation function that converts an image from its coordinate system to the coordinate system of the other image. The Matlab Image Processing Toolbox has a set of image transformation routines that apply to different types of spatial distortion seen in optical misalignment. By mechanically aligning the cameras so that the images were visually similar, the distortion was limited to simpler linear distortions, such as translation and scaling.

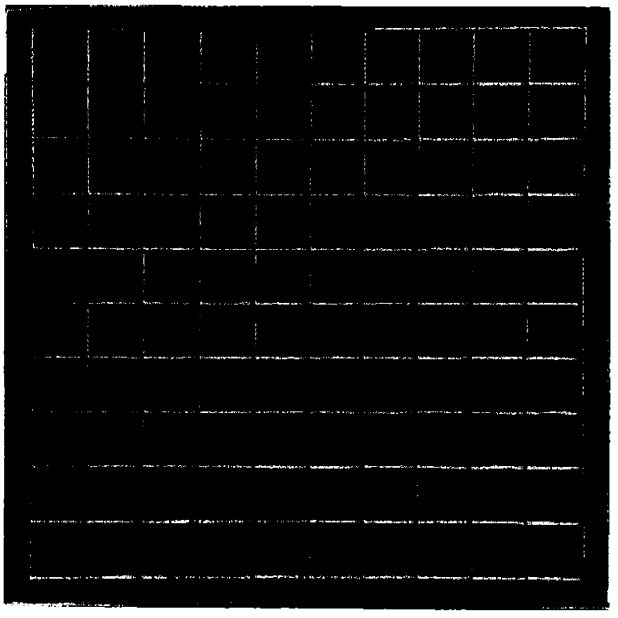

Figure 42: The superposition of two threshold images of the test target that has been electronically aligned. Red indicates perfect alignment, while light blue and green are the lines of the test target from the individual images.

The appropriate transformation routine in the Matlab 'imtransform' function for linear distortions is called the "linear conformal" method. A common method of analyzing registration

targets is to perform a threshold on the image. A threshold is a binary image that is either 0 or 1. The threshold value is the value that marks the boundary between 0 and 1. To aid the mapping algorithms, all alignment images are designed with high contrast between the alignment markers and the background. Performing a threshold on the mean value of the image will usually produce a binary image that clearly shows the alignment markers. Figure 42 shows the superposition of the threshold images of image 2 and the transformed image 1. The red lines are areas of perfect overlap, while the light blue and green are the individual lines corresponding to image 1 and 2. Although the alignment is good, there is not a perfect one-to-once correlation between the two images. The problem lies in the nature of digital imaging. The two cameras observe the test target with the translation and scaling difference that is not in a perfect ratio with the pixel pitch. Thus when one image is transformed, an approximation has to be made when moving the pixels. Some pixel positions lie in-between possible pixel positions and a filtering algorithm is required to determine how the values in the in-between pixels are distributed to adjacent pixels. Although this may appear to be a small issue, the choice of a filtering algorithm can have a significant effect on the final image. The Matlab image registration function "imtransform" by default uses a technique known as bilinear filtering.

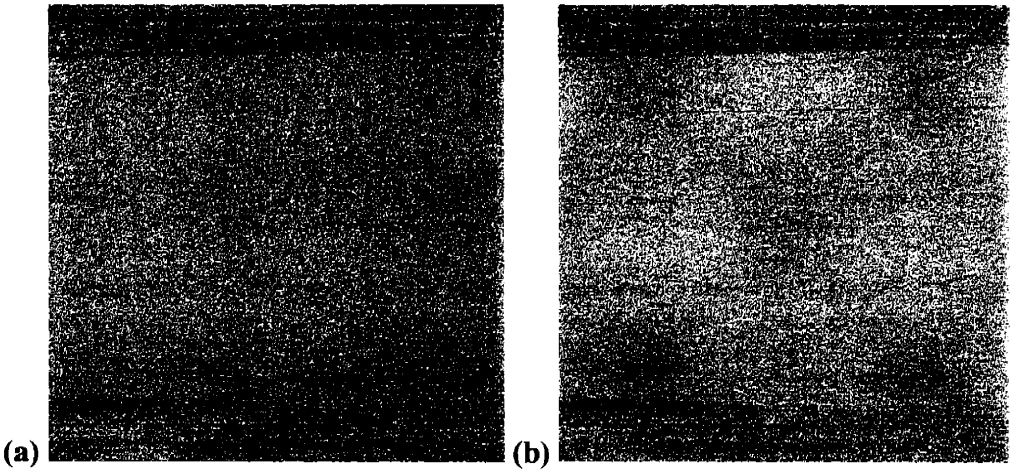

Figure 43: Bilinear filtering example. The images show the result of the division of two fluorescence images taken at different times by the same camera. (a) The images are directly divided. (b) The images were transformed with a function that used bilinear filtering.

This technique is commonly used in image transformations of everyday photographs because it reduces aesthetically unpleasing sharp edges that can result from filtering. However, this technique can introduce artifacts that can affect a measurement system. The images in Figure 43

demonstrate how bilinear filtering affects the final image. Figure 43a shows the division of two images taken at different times with the identical optical system. This is a "perfect registration", since the camera and optical path are exactly the same for the two images. The variations seen are the result of noise in the detector and noise in the laser and have an anisotropic quality. To test the bilinear filter, a transformation function for registration to a different camera was applied to both images.

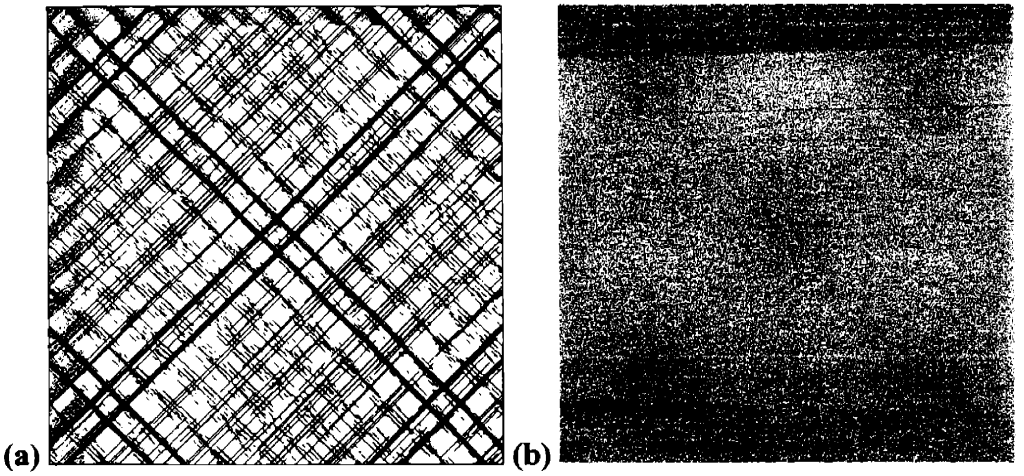

Figure 44: Bilinear filtering comparison. (a) Bilinear filtering on a uniform image. (b) Bilinear filtering on actual data.

Because both images have the same transformation function applied and they are both from the same camera, we expect that dividing them will produce a result that is the same as Figure 43a. However the image in Figure 44b is an image that is smoother and also has an unusual structure in the form of an "X". Bilinear not only smoothes the data, but also introduces some artifacts to the data. The bilinear filtering effects were isolated by performing the transformation operation on an image of completely uniform intensity. In this case the transformation function should produce the exact same image, a completely white image. The results are seen in Figure 44a. The black areas in Figure 44a are picture elements that have a value different from the original base image. We can clearly see in Figure 44a that the image is not all white and there is a specific pattern. The position of this "X" in the uniform image correlates strongly with the "X" in the Figure 44b. Thus we conclude that the "X" was not a result of the optical system, but rather the data processing. If, instead of bilinear filtering, we choose to use nearest neighbor method, the result is the image shown in Figure 45.

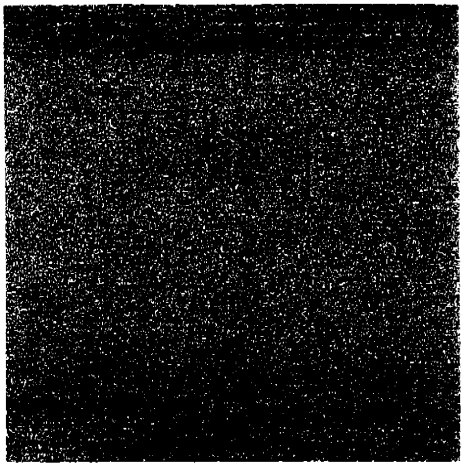

Figure 45: The result of the division of two fluorescence images taken at different times by the same camera. Each image had a transformation function applied that used nearest neighbor filtering.

Clearly, this image maintains the granularity of the original image. Because of the non-homogenous behavior of the bilinear filter, we chose to use the nearest neighbor as the method for resolving the image transformation interpolation method.

Image registration is an important part of the image processing needed for ratiometric imaging systems. Ratiometric systems require two cameras to provide data that is located in the same spatial and temporal position. Mechanical alignment can only partly fulfill the requirements of images that are perfectly aligned. Electronic image registration techniques have been developed to successfully align images from the two cameras in the fluorescence thermometry instrument.

3.7.3 Binning and Error

In an imaging optical measurement system, the precision of a measurement is inversely related to the spatial resolution. The spatial resolution is determined by the number of subdivisions on the imaging sensor and as a result the signal per subdivision (pixel) is a fraction of the original signal. The noise in the detector is given by Poisson statistics which states that the noise in a Poisson process, such as photon detection, is given by the square root of the signal. Thus the S/N ratio drops when the signal intensity falls, and the precision of the measurement

decreases. The signal can be increased by increasing the total sensor area and the sensitivity of the detector. The theory of binning is to reverse the trade-off made with the CCD sensor, by grouping pixels together into larger pixels and thus increase signal, and reduce noise and spatial resolution. There are two types of binning, on-chip binning and off-chip binning. On-chip binning is possible with CCD cameras that support it. In on-chip binning, the CCD combines the charges of the grouping of the pixels and reads out only the reduced spatial resolution image. The advantage of this is that any fixed noise from the CCD, such as in the amplifiers and in the ADC is only present once in each pixel group, whereas if the binning is done off-chip, the noise is present in every pixel read out. Off-chip is more flexible because it provides the original high spatial resolution image. If we decide against the trade-off of spatial for precision, the original data is available, instead of being lost in the on-chip binning approach. In this section we will discuss off-chip binning, because it is possible with any camera system, since the operations are performed after the images are captured.

Rhodamine B fluorescence decreases in intensity with temperature increases, and thus reduced precision is expected as temperature increases

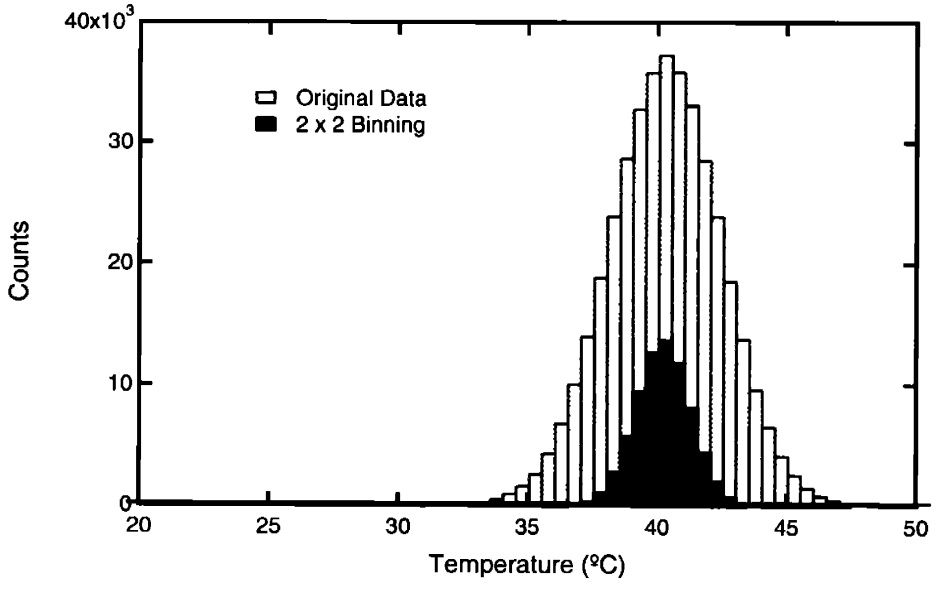

Figure 46: Overlaid plots of the histograms of temperatures measured for the original data and 2X2 binning in a sample at a constant temperature of 41.5 °C.

A sample with a uniform temperature of 41.5 °C was measured by the fluorescence thermometry instrument and we will examine the effect of binning on this high temperature case as a worst-case analysis. The size of each measurement area is 0.0676 mm per pixel. In 2 X 2 binning, a 4 pixel block is converted into a single pixel, increasing the area by 4 and decreasing the resolution in each direction by a factor of 2. The histograms in Figure 46 show the distribution of the temperature measurements made from the original data and 2X2 binning.

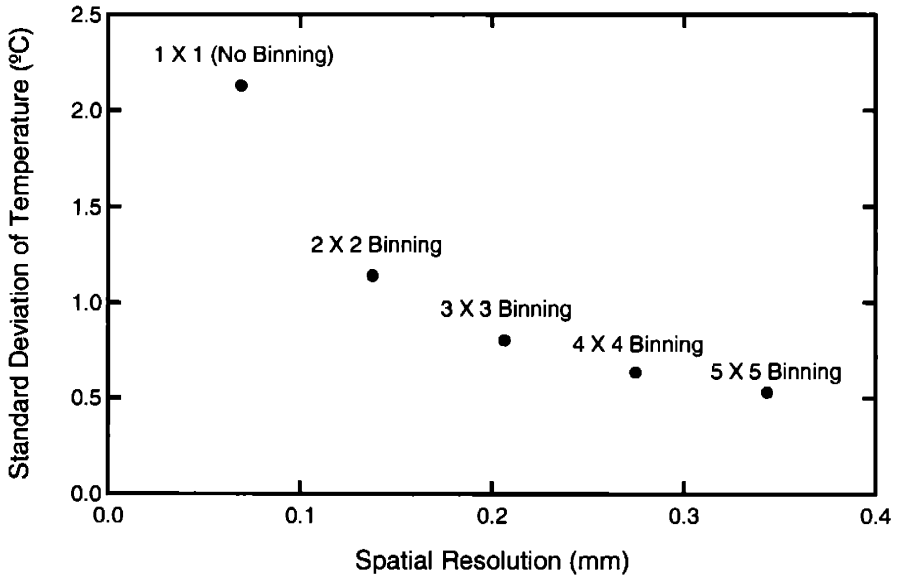

Figure 47: The effect of binning on spatial resolution and the standard deviation for binning between 1x1 and 5x5.

The change in the distribution with 2 X 2 binning can be plainly seen. The absolute count is reduced due to the reduction in resolution by binning and the distribution narrows, reflecting a reduction in noise. Figure 47 shows the effect of binning from the original to a 5x5 pixel group on the spatial resolution and on the standard deviation of the temperature measurements. From this plot we can see that the decrease in noise falls exponentially. The best trade-off between spatial resolution and noise occurs between 2 X 2 and 3 X 3 binning. At 3 X 3 binning the fluorescence thermometry instrument has a temperature resolution of +/- 1.6 °C (2 standard deviations, 95% confidence) and a spatial resolution of 0.2 mm.

The spatial resolution of an imaging detection system is inversely related to the noise in the system because of the Poisson process that governs the photon detection. Binning is a

technique that allows imaging researchers to choose different trade-offs between noise and spatial resolution in images according to their needs. In the fluorescence thermometry instrument, we have shown that the best trade-off for this instrument lies at the 3 X 3 binning, where the instrument has a temperature resolution of +/- 1.6 °C (2 standard deviations, 95% confidence) and a spatial resolution of 0.2 mm.

References:

1. Cooper, C.S. and N.M. Laurendeau, *Laser-Induced Fluorescence Measurements in Lean Direct- Injection Spray Flames: Technique Development and Application.* Measurement Science & Technology, 2000. **11**(7): p. 902-911.
2. Hanson, R.K., *Planar Laser-Induced Fluorescence.* Journal of Quantum Spectroscopic Radiation Transfer, 1988. **40**(3): p. 343-362.
3. Cessou, A., U. Meier, and D. Stepowski, *Applications of Planar Laser Induced Fluorescence in Turbulent Reacting Flows.* Measurement Science & Technology, 2000. **11**(7): p. 887-901.
4. Lee, M.P., B.K. McMillin, and R.K. Hanson, *Temperature Measurements in Gases by Use of Planar Laser-Induced Fluorescence Imaging of No.* Applied Optics, 1993. **32**(27): p. 5379-5396.
5. Lemoine, F., M. Wolff, and M. Lebouche, *Simultaneous Concentration and Velocity Measurements Using Combined Laser-Induced Fluorescence and Laser Doppler Velocimetry: Application to Turbulent Transport.* Experiments in Fluids, 1996. **20**(5): p. 319-327.
6. Lemoine, F., Y. Antoine, M. Wolff, and M. Lebouche, *Simultaneous Temperature and 2d Velocity Measurements in a Turbulent Heated Jet Using Combined Laser-Induced Fluorescence and Lda.* Experiments in Fluids, 1999. **26**(4): p. 315-323.
7. Sakakibara, J. and R.J. Adrian, *Whole Field Measurement of Temperature in Water Using Two-Color Laser Induced Fluorescence (Vol 26, Pg 7, 1999).* Experiments in Fluids, 1999. **27**(1): p. U1-U1.
8. Arbeloa, F.L., T.L. Arbeloa, M.J.T. Estevez, and I.L. Arbeloa, *Photophysics of Rhodamines - Molecular-Structure and Solvent Effects.* Journal of Physical Chemistry, 1991. **95**(6): p. 2203-2208.

Chapter 4: Verification Experiments

4.1 Introduction

In Chapter 3, the design of the excitation and detection components of the fluorescence thermometry instrument was discussed in detail. The final design for the test version of the instrument was presented. The potential problems with fluorescent probes, such as photobleaching and adsorption of the probes to the sample cell wall were discussed, along with optical problems such as etalons and occlusions in the beam path. With the completion of the design of the instrument, the next question to be addressed is the verification of its operational capabilities. There are two stages to the verification process. The first stage is to test the whether 3D images of a sample at a known uniform temperature can be measured. This test will verify the accuracy of the instrument and provide a check on its spatial uniformity across different 3D planes. The second stage of testing involves using an experimental setup that generates a temporal change in temperature to verify the accuracy of the instrument for temperature distribution measurements of dynamic processes. In this chapter we present the two experimental validation tests as well as a mathematical verification of the dynamic test.

4.2 Experimental Tests

4.2.1 Uniform Temperature Test

The most obvious test of a thermometry instrument is whether it is accurate at measuring temperatures in samples of a known uniform temperature. In the case of the fluorescence thermometry instrument, the additional test will be to check if the measurements are consistent in all three dimensions. The test setup for the uniform temperature sample cell is shown schematically in Figure 48. The sample cell was heated from below by an aluminum block that was fitted with channels for heated water. The water for the aluminum block is temperature controlled by a VWR Scientific 1168 water bath.

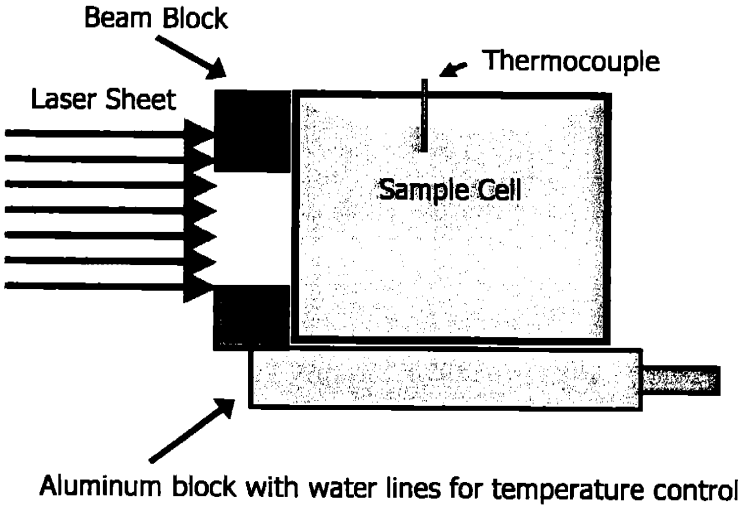

Figure 48: Schematic of constant temperature control sample cell setup.

The setup relied on convection to mix the fluid so that the temperature remained constant. The sample cell is a 50.8 mm square open top glass container with optically clear walls on all four sides. The sample cell was loaded with a solution of Rhodamine B labeled Dextran at 0.3 μM and Rhodamine 110 at 0.03 μM in deionized water. A thermocouple was used to monitor the actual temperature in the sample cell. Four temperatures were set on the water bath: room temperature, 30 °C, 40 °C, and 50 °C. The sample cell was allowed to equilibrate at each temperature for 1 hour to ensure a uniform temperature. The temperature measurements made at the thermocouple was found to be: 24.2 °C, 27.6 °C, 34.7 °C, and 41.5 °C. The laser power was set to 620 mW and the exposure time for each image was 100 ms. Five positions in the z-axis space were tested starting at 20 mm from the front wall and spaced in 5 mm increments.

The temperature across the entire 2D plane at the second z position (25 mm) is summarized in the histograms shown in Figure 49. In this plot we can see that each histogram has the same approximate distribution of temperatures centered on a peak that is close to the thermocouple temperature. The clear separation of the histograms shows that the temperature response is being observed by the cameras and the distribution is representative of the error. The shape of the distribution resembles a Gaussian and that is expected if the distribution is noise due to the Poisson statistics of fluorescence measurements. In Figure 50, mean temperature of each histogram in Figure 49 is plotted versus the thermocouple temperature measurement.

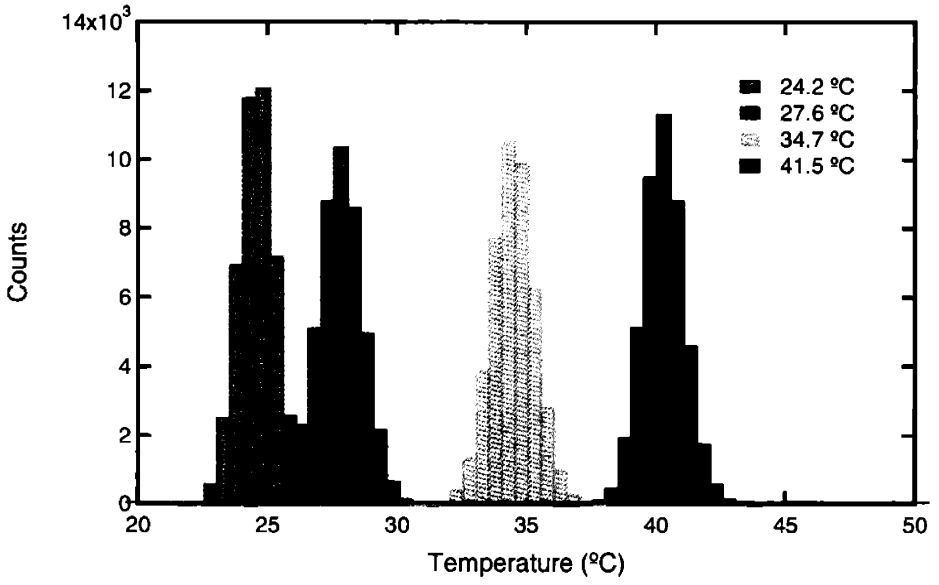

Figure 49: Distribution of temperatures measured in the 2D plane of z = 25 mm for a sample at different uniform temperatures. (3X3 Binning)

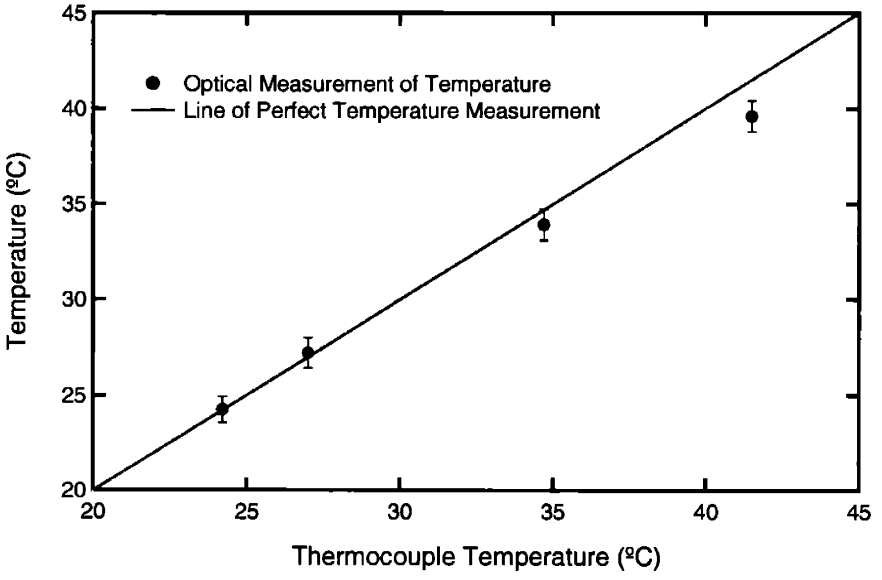

Figure 50: Plot of the mean temperature against the thermocouple temperature. The error bars correspond to ±2 standard deviations in the temperature measurement.

The 1:1 temperature correlation line is the ideal response of a temperature measurement system. From this plot it is evident that the temperature measurement by the fluorescence thermometry instrument is accurate below 35 °C. At temperatures higher than 35 °C the instrument begins to underpredict the temperature. These results show that at constant temperatures, the fluorescence thermometry instrument can measure temperature accurately with increasing error as the sample

temperature increases and maintaining the same precision throughout the entire experiment. The 3D capabilities of the instrument were checked by repeating the same temperature measurements done in 2D at different positions along the z-axis. The mean temperature of five tested 3D positions at each temperature is shown in Figure 51.

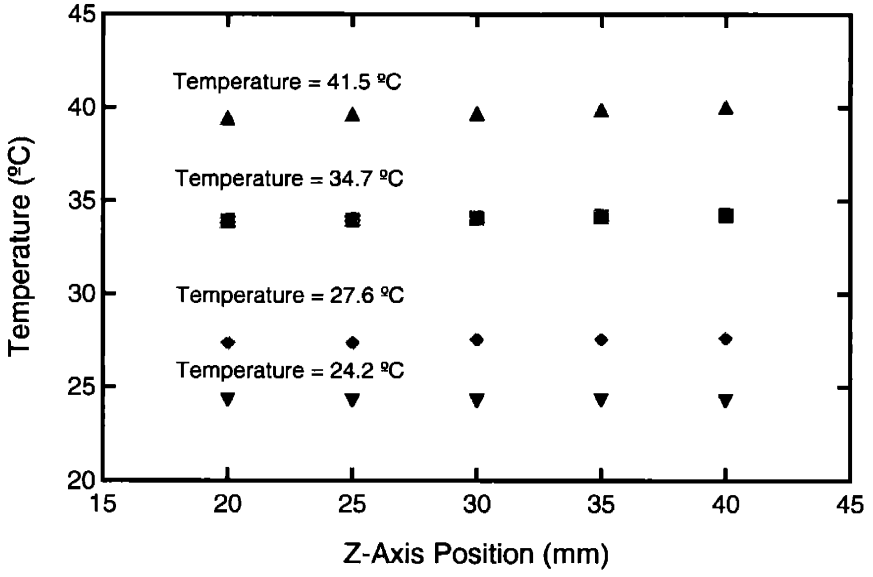

Figure 51: The mean temperature of each z-axis position at four sample temperatures.

The temperature trends in Figure 51 are very near a horizontal line, indicating that the fluorescence thermometry instrument measurements were consistent throughout the sample cell. The standard deviations, which are not shown, were also found to be consistent across all 5 sample planes. The error calculated in Chapter 3, showed that the instrument is capable of an accuracy of ±1.6 °C with 3 X 3 binning.

The results of the test of the fluorescence thermometry instrument for static temperatures were successful. The instrument was able to measure temperature with a small offset error that increases with temperature. Measurements made along different points of the z-axis were consistent in the mean temperatures and in the error.

4.2.2 Temperature Changes with Time

The preceding section has shown that the fluorescence thermometry instrument can make temperature measurements in 3D for a static sample at uniform temperature. The second phase of testing requires the verification of a dynamic system. The goal of dynamic verification is to match evolution of a temperature change over time with the results of a mathematical model of the system. The same basic experimental setup for the static verification experiment was used with the addition of a glass test tube encased cartridge heater to provide time-variable heat input. A schematic of the sample cell and heating system is shown in Figure 52.

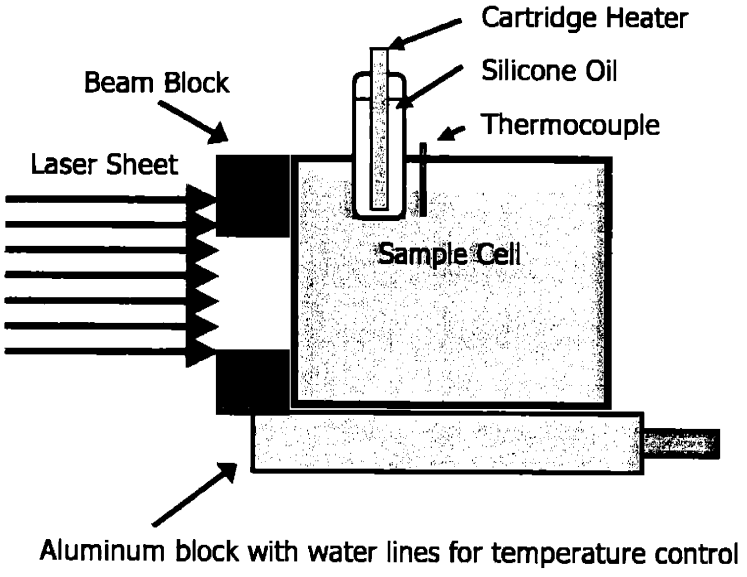

Figure 52: Schematic of the sample cell test setup.

The cartridge heater sheathed in a test tube to minimize interactions with the medium. Silicone oil was used between the heater and the test tube wall to act as a thermal conductor and avoid creating hotspots on the test tube. The cartridge heater was inserted into the water from the top and placed at an off-set position to create spatial gradients in the heating. The cartridge heater was driven at a constant current and provided a constant heat flux into the sample. The aluminum base was driven at a constant temperature to provide heat removal.

The sample cell was loaded with a solution of Rhodamine B labeled Dextran at 0.3 μM and Rhodamine 110 at 0.03 μM in deionized water and allowed to equilibrate at each

temperature for 1 hour to ensure a uniform starting temperature. The water bath was set to 24.1 °C which corresponded to room temperature. The laser power was set to 620 mW and the cameras were set to an exposure time of 100 ms. The cartridge heater was activated after the equilibration period and operated at constant current over 87 minutes. Temperature from the thermocouple was recorded and images were collected at 3 minute intervals for five different z-axis positions separated by 5 mm. Because of the large disparity in spatial resolution between the z-axis and the x and y-axis, we chose to bin using a 56 X 55 bin size (x,y). This bin size produces a 3D image with the resolution of 13 X 10 X 5 (x,y,z) with a voxel (volume element) size of 3.7 mm x 3.7 mm x 5 mm.

The plot in Figure 53 shows three different x-z planes in their correct relative positions in 3D. These temperatures were measured after 87 minutes of heating by the cartridge heater. In this plot the camera observation direction is normal to the x-y plane looking in the direction of increasing z positions. The heater is located approximately at (3,0,3.5) (x,y,z).

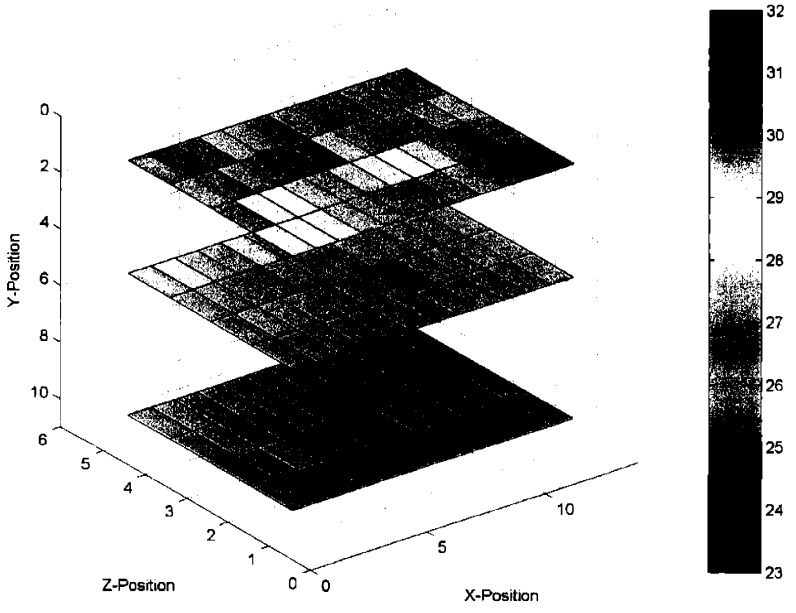

Figure 53: Temperature measurements in three different planes of the sample cell after 87 minutes of heating.

Although a non-uniform heating pattern was expected in the x-z plane, the plot shows otherwise. There a temperature increase in the vicinity of the heater, but as a whole, the temperatures in the x-z planes were relatively uniform. These observations led to the hypothesis that convection driven mixing might explain the relatively flat temperature profiles. A schematic of the process is shown in Figure 54.

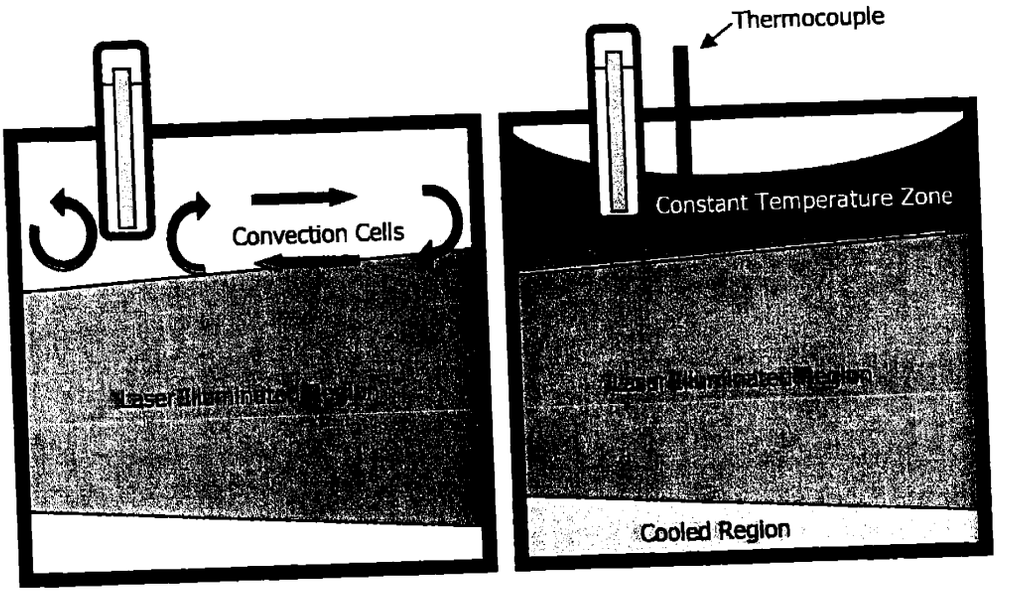

Figure 54: Theoretical convection heating process that occurred in sample cell.

The vertical surface of the heater forms convection cells which drives a mixing process in the top layer. The convection driven mixing makes the top layer of water fairly uniform in temperature, which then heats the rest of the cell by conduction. This theory would explain the results seen in Figure 53.

In order to verify that this hypothesis of the mixing layer is what is observed, a mathematical model of the system must be built to compare to experimental data at different time steps. The top layer can be treated as a single uniform layer whose temperature was measured by the thermocouple. The first step is to describe the temperature of the heating in the top layer. The thermocouple in the sample cell was in a position to measure temperature in the top layer and the temperatures measured over time are shown in Figure 55.

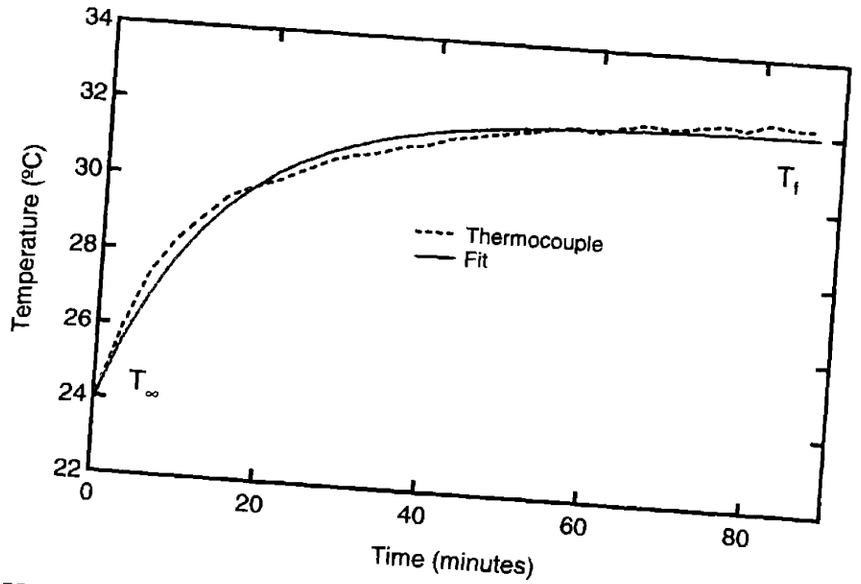

Figure 55: Least-squares fit to the thermocouple data.

The form of the temperature response of the thermocouple is an exponential and the equation chosen to describe it is:

$$\Theta = 1 - e^{-k\tau} \tag{4-1}$$

where the non-dimensionalized temperature Θ is defined as:

$$\Theta = \frac{T - T_\infty}{T_f - T_\infty} \tag{4-2}$$

and the non-dimensionalized time τ is defined as:

$$\tau = \frac{t\alpha}{L^2} \tag{4-3}$$

The value of k is 21 and can be thought of as the rate constant for energy transfer to the constant temperature zone versus the conduction zone. The characteristic time for conduction, L^2/α, is 293 minutes for the length of the cell, L = 50.8 mm. The fit closely matches the experimental data from the thermocouple and this result is used to describe the top boundary condition in a 1D model of the sample cell. The diagram shown Figure 56 describes the non-dimensionalized mathematical model of the system.

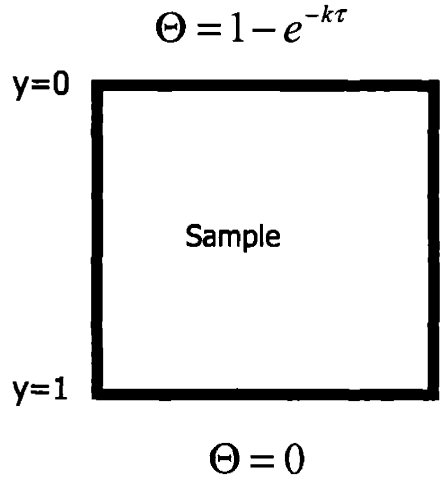

Figure 56: 1D non-dimensionalized model of sample cell heating experiment.

The top of the sample cell is driven by the top heating layer, described by Equation 4-1. The bottom of the sample cell is held by the aluminum block at room temperature, T_∞, therefore the non-dimensionalized temperature, Θ, is zero. In non-dimensional form the energy-balance equation can be simplified written as:

$$\frac{\partial \Theta}{\partial \tau} = \frac{\partial^2 \Theta}{\partial y^2} \tag{4-4}$$

The initial condition in non-dimensional form is:

$$\Theta(y,0) = 0 \tag{4-5}$$

The energy-balance equation can be solved using the FFT (Finite Fourier Transform) method and the final solution for Θ can be expressed as:

$$\Theta(y,\tau) = 2\sum_{n=1}^{\infty}\left[\left(1-\frac{k}{n\pi}\right)\left(e^{-(n\pi)^2\tau}-e^{-k\tau}\right)-e^{-(n\pi)^2\tau}+1\right]\frac{\sin(n\pi y)}{n\pi} \tag{4-6}$$

The experimental data consists of three spatial dimensions, time, and temperature. This 5D space cannot be represented on a 2D image and our model only contains three dimensions (time, temperature, y-axis). Therefore a subsection of the experimental data will be compared to the

model results. The voxels in the experimental data are referenced by the numbering scheme shown in Figure 57.

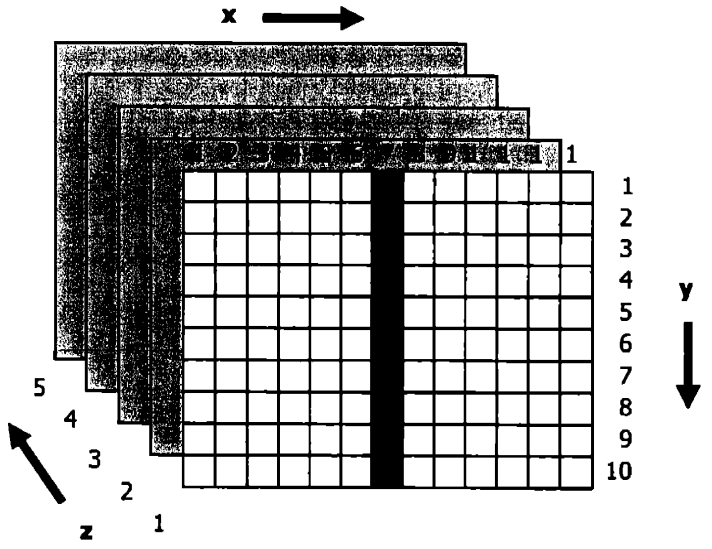

Figure 57: X, Y, Z position numbering convention.

The only spatial dimension in the model is the y-axis. Therefore we must choose a specific x and z coordinate in the experimental data to specify the location of y values to be compared with the model results. The x = 7 column and the z = 4 plane were chosen as the coordinates that would best match the model conditions. The x = 4 position was selected because it is at the centerline of the cell and least affected by any wall effects from the sample cell. The z = 4 plane was chosen because it is closest to the plane where the cartridge heater is located. The model results and experimental data for this coordinate are plotted in Figure 58.

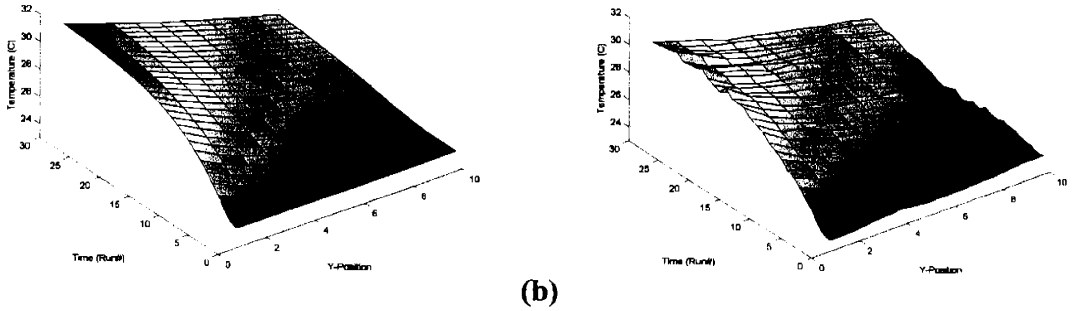

(a) (b)

Figure 58: Comparison of (a) model and (b) experimental results.

Figure 58 shows the temperature variation along the y-axis in time. The time evolution of the temperature profile in the experimental solution matches the model very well. The final temperature in the experiment is lower than in the model, but can be easily the result of heat loss through the side walls that were assumed to be adiabatic in the model.

The results of the test of the fluorescence thermometry instrument for time-evolving temperatures were successful. The instrument was able to measure a time-temperature profile in close agreement with predictions from a model of the system. A small offset in the final temperature was measured, but can be accounted for by simplifications made in the model.

4.3 Summary of the Capabilities of the Instrument

The capabilities of the 3D fluorescence thermometry instrument can be characterized by four main parameters: temperature resolution, spatial resolution, temporal resolution and imaging speed. The temperature resolution and spatial resolution have an inverse relationship. From chapter 3, a 3 X 3 binning of pixels offers the best temperature resolution with a minimum of loss of spatial resolution. With a 3 X 3 binning, the temperature resolution is +/-1.6 °C (2 standard deviations, 95% confidence) and the spatial resolution is 0.2 mm in the x-y plane. The spatial resolution in the z-axis depends on the width of the laser beam, which is estimated at <5 mm. The temporal resolution is limited by the exposure time, which is 100 ms. The imaging speed has two components, 2D imaging speed, and the z-translation speed. The 2D imaging has the maximum rate of 1 frame per second, while the z-translation speed is approximately 2 seconds for every 5 mm translation. In this chapter, we compared the results of the instrument with model predictions in experiments with static and dynamic temperature fields. These experiments have verified that the instrument can measure both static and dynamic temperature fields. Chapter 5 will go forward and discuss the final modifications of fluorescence thermometry instrument so that it can operate in a microwave cavity. The results of experiments with a microwave heated sample are also presented in Chapter 5.

Chapter 5: Temperature Measurement of Microwave Heating

5.1 Introduction

Fluorescence-based thermometry using molecular probes is a powerful tool for examining temperature fields in 2D and 3D for systems in hostile environments such as a microwave heated system. In the preceding chapters, the issues surrounding the theory of fluorescence, the particular choice of probes was explored. In chapter 3, the specifics of the optical design of a fluorescence-based thermometry instrument was examined. The numerous challenges of spectral separation of fluorescence signal, artifacts from photobleaching, etalon formation, probe concentration, and surface adsorption were tackled. The final system uses Dextran labeled with Rhodamine B as the temperature sensitive probe and Rhodamine 110 as the reference probe. In chapter 4 a series of experiments were described which established the capabilities of the system. Static and dynamic tests conducted, verified the operation of the system and established it's accuracy at +/-1.6 °C with a spatial resolution of 0.2 mm in x-y plane and 5 mm in the z plane. In this chapter we address the optical difficulties surrounding the use of the instrument in an enclosed microwave cavity and describe the final instrument constructed. 2D and 3D experiments were performed on microwave heated solutions. The results of 2D experiments on the effect of salt solution on microwave heating over time is explored and compared to 2D simulations performed in FemLab.

5.2 Imaging inside a Microwave Cavity

A typical microwave heating arrangement consists of a microwave generator connected to a closed box with a waveguide as shown in Figure 59. The sample is placed in this box and is heated by microwaves entering the box. The box is a resonant cavity where the microwaves set up a set of standing and propagating electromagnetic waves, known as modes, through reflection and interference. The local electric field can vary widely from point to point within both the cavity and the sample. The particular modes found in a resonant cavity are determined by the geometry, frequency of the electromagnetic radiation, and the properties of the sample, or load.

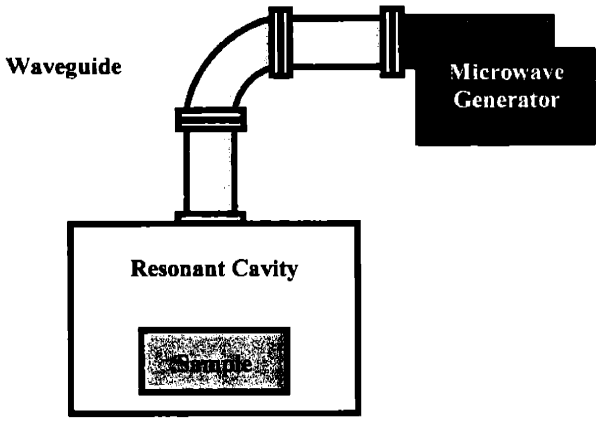

Figure 59: Simple resonant cavity microwave heating system.

This simple design is quite similar to the modern home microwave oven. Depending on the particular load placed in the microwave oven, the modes may produce multiple hotspots or areas where the electric field is more intense.[1,2] These hotspots lead to uneven application of power in the oven and, to partially combat this problem, most ovens are equipped with a mode-stirrer. A mode-stirrer, as its name implies, changes the modes in the cavity by randomly disrupting the microwaves coming from the waveguide. Typically this is accomplished by means of a fan with irregular blades to cause reflections at different angles. The energy that is transferred into the resonant cavity is stored there until it is absorbed through one of three processes: heating of the walls, heating of the load, or reflecting back to the magnetron and heating it. The resonant cavity increases the efficiency of microwave heating by limiting losses to the environment, but creates a problem for optical thermometry. The cavity is enclosed by conducting material that is opaque to visible radiation. Although, because of the wavelength of microwaves, a coarse mesh can be substituted for a wall, the mesh found on home microwave ovens would significantly reduce the resolution acquired on any sample in the cavity. The solution to the problem of optical access is solved by using a carefully designed microwave cavity.

We have used a commercially available microwave cavity plasma heater with orthogonal optical ports designed by Sairem to power plasmas in a quartz tube. (Figure 60) The cavity is a modified section of a microwave waveguide with two large ports on either side to provide entrances for the quartz tube and two smaller auxiliary ports for optical observation of the plasma. This microwave cavity is a single mode cavity resonator.

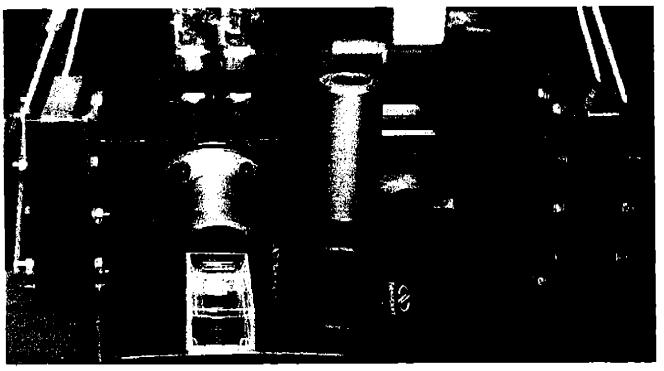

Figure 60: Microwave cavity plasma heater designed by Sairem

Unlike the home microwave oven, this cavity excites a single mode which is easier to model and control. The complete system is shown schematically in Figure 61 and has a number of components that are not typically found on a home microwave oven.

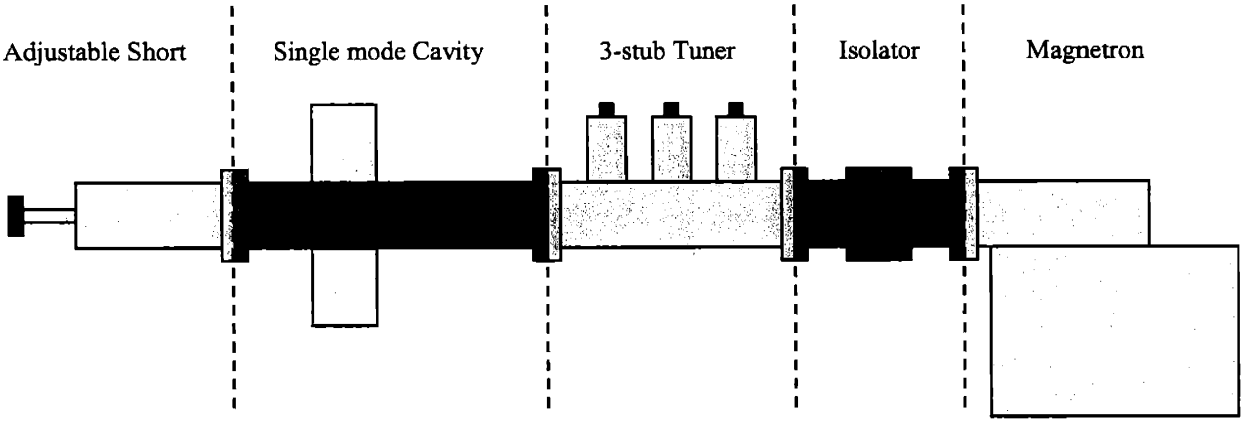

Figure 61: The microwave generator and resonant cavity.

The entire system was purchased from Sairem and consists of a GMP12K/SM 1.2 kW microwave generator, CD1 isolator, MC1 3-stub tuner, SC3 single mode cavity and MC3 sliding short circuit. The magnetron is the first component in the chain and generates the microwave radiation at a specific frequency, in this case 2.45 GHz. The isolator prevents reflected microwave radiation from reaching the magnetron by deflecting the reflected microwaves into a reservoir of water, known as a dummy load. The tuner is a metal rod that can be inserted at a set distance into the waveguide to change the impedance of the cavity. When the impedance of the load in the cavity is matched with the impedance in the transmission line, reflection drops to zero and the power absorbed by the load is maximized. The single mode cavity is a microwave

plasma applicator in which the sample is placed and contains the optical imaging ports and an adjustable position aperture located in the waveguide in front of the ports. Finally, the adjustable short circuit is used to alter the cavity length and thus change the modes that are present in the cavity. The cavity itself is defined by the position of the aperture and the short circuit. The aperture is a metal plate with an open hole in its center that is inserted into the waveguide to reduce the size of the waveguide input cross-section and to provide a reflective surface to create a resonant cavity.

5.3 Optical Challenges

The microwave plasma applicator is a section of the microwave waveguide that has been fitted with two large cooled chimneys and two small optical observation ports at right angles to each other, providing optical access to ensure that for the fluorescence observation, the excitation beam is perpendicular to the observation path. The two major optical challenges are to illuminate the sample with sheet of laser light inside the cavity, and to capture the fluorescence image from the position normal to that plane. The two ports are shown in Figure 62.

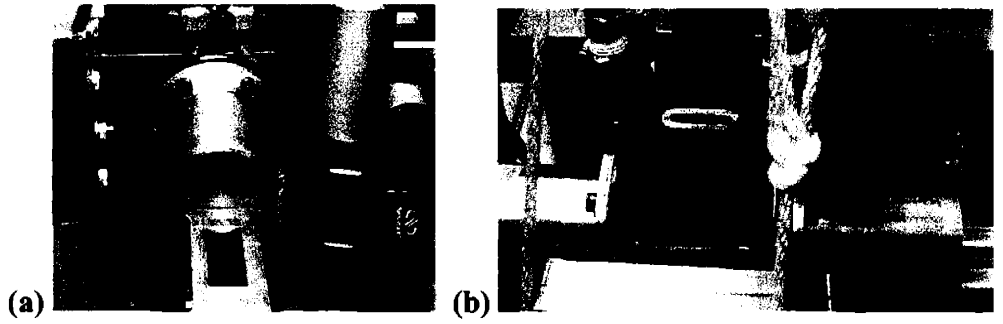

Figure 62: Microwave applicator openings. (a) 50 mm circular port (b) 20 mm long port.

Because of its size, the 50mm diameter larger opening, or chimney, in Figure 62a was used by the cameras to image the sample. The smaller oval port in Figure 62b was used as the entrance for the excitation laser beam. The orientation of the oval allowed us to position the beam for 3D imaging, but the narrow width makes beam expansion more difficult. A simple expansion of the beam outside the cavity that matched the width of the port resulted in a very narrow region of illumination in the cavity as shown in Figure 63.

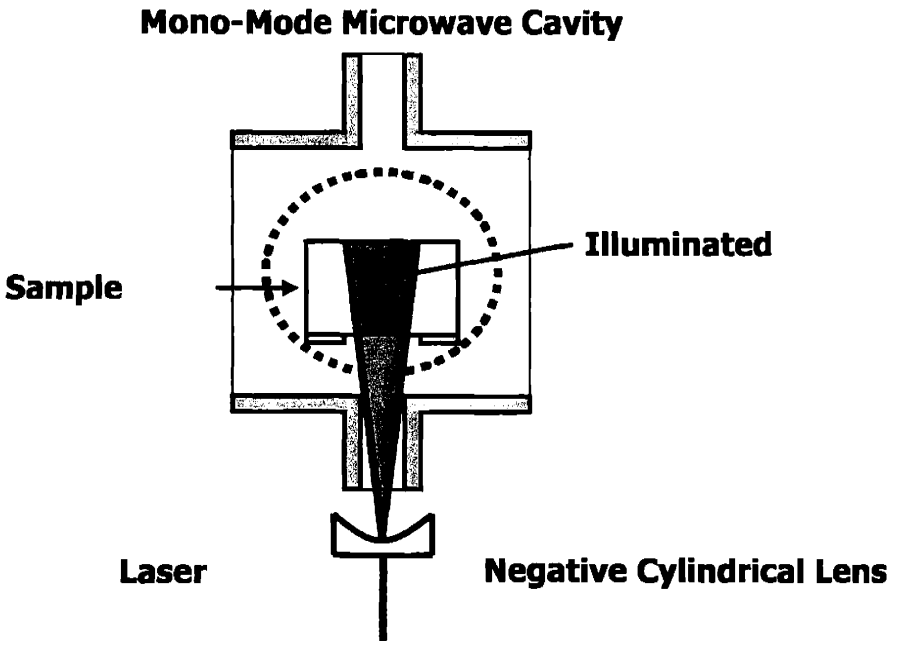

Figure 63: Microwave cavity illumination with a negative lens.

It is apparent that the limiting dimension is the interior width of port coupled with the closest approach of the lens. In order to increase the illuminated area an alternate strategy was devised to focus the beam at a point inside the port as seen in Figure 64.

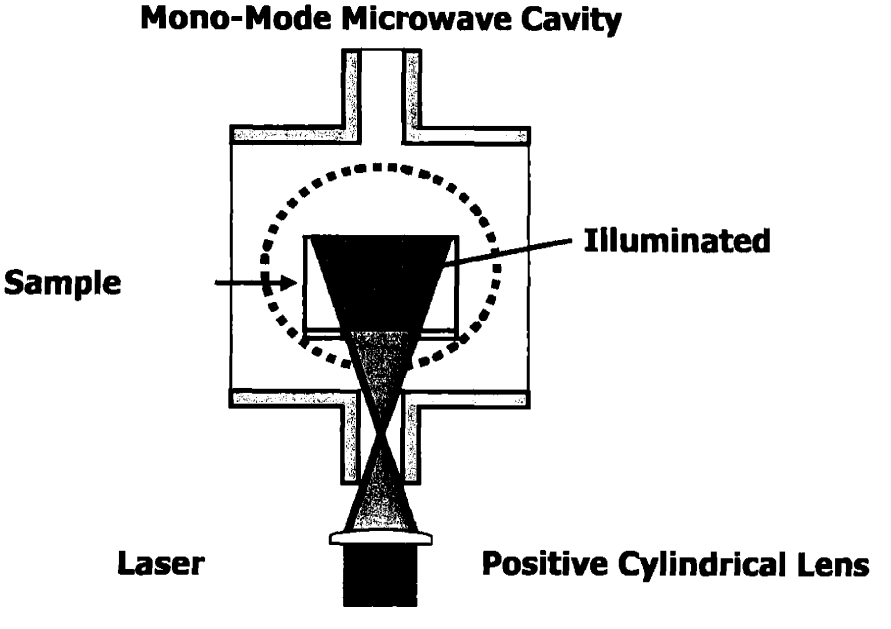

Figure 64: Microwave cavity illumination with a positive lens.

The positive lens in this optical layout doubled the maximum expansion angle of the beam by moving the focal point inside the optical port which allowed substantially more of the interior to be illuminated. However, this approach also presented a serious limitation in that the focused point of laser energy caused local heating of the air that could disturb the beam stability. This effect is the same as the commonly seen optical distortion when viewing objects behind a heated region of air, such as air heated by the tail pipe of a vehicle or a section of pavement on a hot summer day. Because the Rhodamine B and Rhodamine 110 probes have a high quantum yield, the limit on laser power was not a significant barrier to our design, and in order to maximize the field of view, the positive lens design was chosen.

Reproducible positioning of the sample cell was crucial, both for experimental repeatability and to avoid etalon problems. In chapter 3, the issue of etalon formation was addressed. The origin of the etalon is the glass wall of the sample cell. The width of the wall determines the exact pattern of lines formed by the interference of partial reflections from the two interfaces of the wall. Since the exact line position was recorded in the calibration images taken of the single probe cases for the instrument it was necessary to align the images properly. The sample cell was therefore mechanically constrained to the exact same location each time a sample was changed. While this is easily done in the open by means of mechanical guides, the addition of anything in the microwave cavity needs to be done with care. If the material used absorbs microwaves to any significant degree, the entire microwave field will be disrupted. A carrier for the sample cell was machined from a plastic (Polysulfone) that had been shown to be transparent to microwaves. (Figure 65)

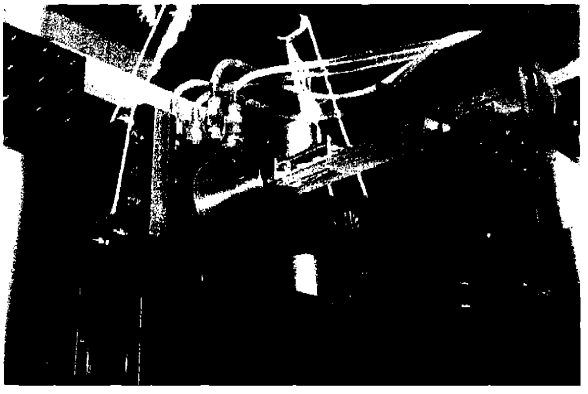

Figure 65: The sample cell with the carrier prior to loading into the microwave cavity.

The sample cell had exterior dimensions of 23.6 mm x 34 mm x 70 mm (HWD) and was registered to the carrier by a raised L shaped guide. The carrier was moved manually and slid into the cavity until it hit a mechanical stop. The carrier also had a clear aperture in the bottom through which the expanded laser beam passed. (Figure 66)

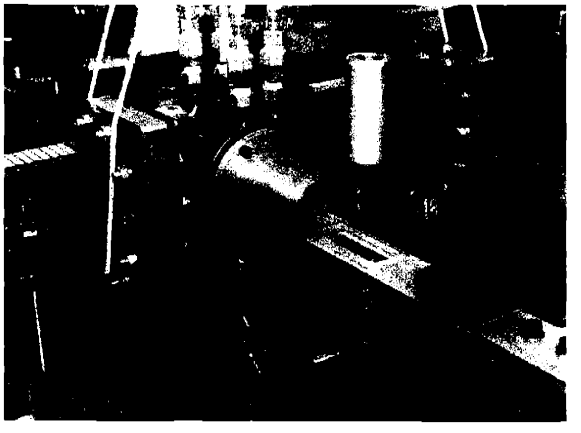

Figure 66: The sample carrier without the sample cell. The clear aperture for the laser is shown here.

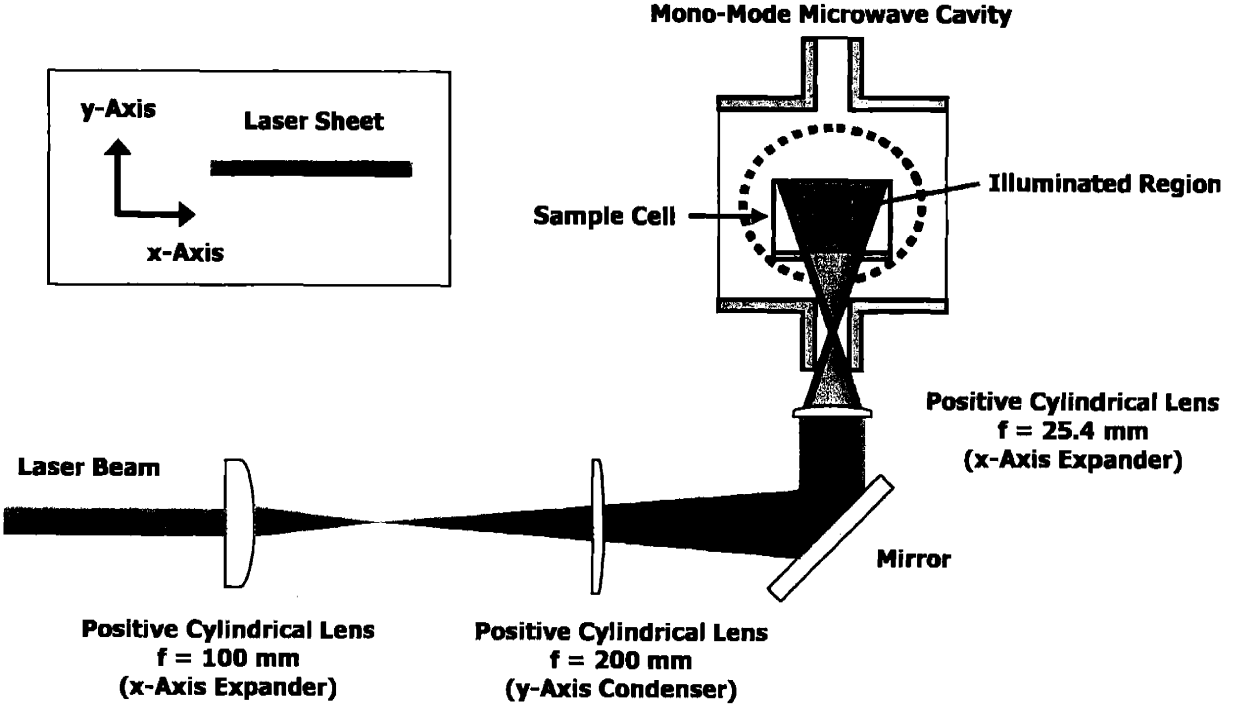

Figure 67: Complete optical path for illuminating the microwave cavity.

The complete optical layout is shown in Figure 67, and incorporates the positive lens in Figure 64 along with two other lenses necessary to provide initial laser beam sizing. The three positive lenses in this optical system were used to shape the beam. The first lens (Newport CKX100AR.14 f = 100 mm) was used to set the width (x-axis) of the input beam for the last lens so that the maximum area of the sample could be illuminated. The second lens (Newport CKX200AR.14 f = 200 mm) was used to gradually focus the (y-axis) to counteract the divergence of the laser beam. The last lens (Newport CKX025AR.14 f = 25.4 mm) was the positive lens seen in Figure 64 and focused the laser beam to a point midway into the optical port to attain the maximum expansion angle in the cavity.

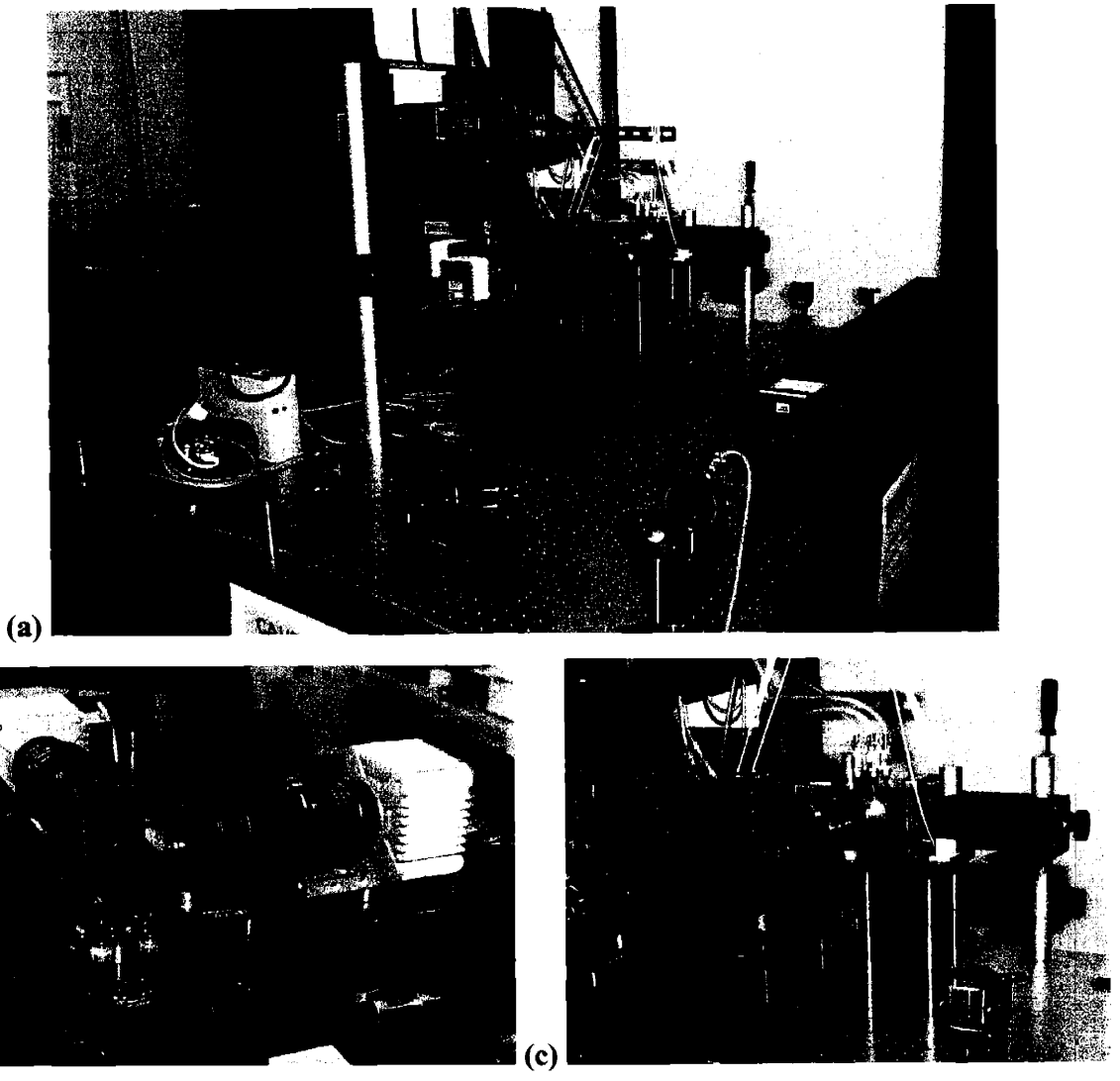

Figure 68: (a) The entire optical setup. (b) Dual camera setup with dichroic mirror. (c) View of microwave cavity from the camera side.

Although the microwave applicator was designed to contain the microwaves, at higher power levels, some microwave leakage may be possible. To ensure the safety of the camera electronics, the camera system was located 50 cm away from the microwave applicator. This is a significant change from the test instrument described in chapter 3, where the cameras were <20 cm from the sample cell. The longer distance coupled with a decrease in the observing area from 2581 mm^2 to 802 mm^2 required a change in the camera lenses. Nikon Micro Nikkor 105 mm lenses replaced the original lenses and Hamamatsu Orca ER cameras replaced the original cameras. The new cameras are capable of higher frame rates than the original Qimaging cameras. The change in the relative position of the sample vis-à-vis the dichroic mirror also had a secondary consequence. The reflected image was no longer in focus because a blurred double image was formed by a superposition of reflections from both interfaces of the dichroic mirror. The dichroic mirror was replaced with an Omega Optical XF2017 which had an anti-reflection coating that removed the reflections from the second interface. The instrument with the microwave system installed is shown in Figure 68.

5.4 2D Experiments

5.4.1 Introduction

Microwaves are electromagnetic waves and ultimately, microwave heating depends on the strength of the electric fields in a load and the strength of the coupling between the load and these electric fields.[3, 4] The two parameters that affect the electric field are the resonant cavity geometry and the properties of the dielectric load. These parameters are coupled and the interaction is further complicated by the strong temperature dependence of the dielectric properties in many materials.[2] The strongest candidate for use as a sample in testing microwave heating is water. The 2.45 GHz frequency of the microwave generator is ideal for heating water, it is well studied, a critical component in food heating (thus, industrially relevant) and has well-characterized dielectric properties. Finally, the Dextran labeled Rhodamine B and Rhodamine 110 fluorescent probe combination is usable in a water system. The two avenues we have to manipulate the electric field are the cavity geometry and the properties of water. We modified the dielectric properties of water with salt (NaCl), which is safe, is present in foods, is readily

available, and has a substantial effect on the dielectric properties of water. Extensive data is available from literature on the dielectric properties of salt solutions. [5-10]

5.4.2 Effect of Salt on Microwave Heating

Both the dielectric constant and the dielectric loss constant are affected when salt (NaCl) is dissolved in water. The graph Figure 69 shows the differences in dielectric constant and dielectric loss constant between water and 0.5 M salt concentration. The values in Figure 69 are calculated from relations given by Stogryn.[10]

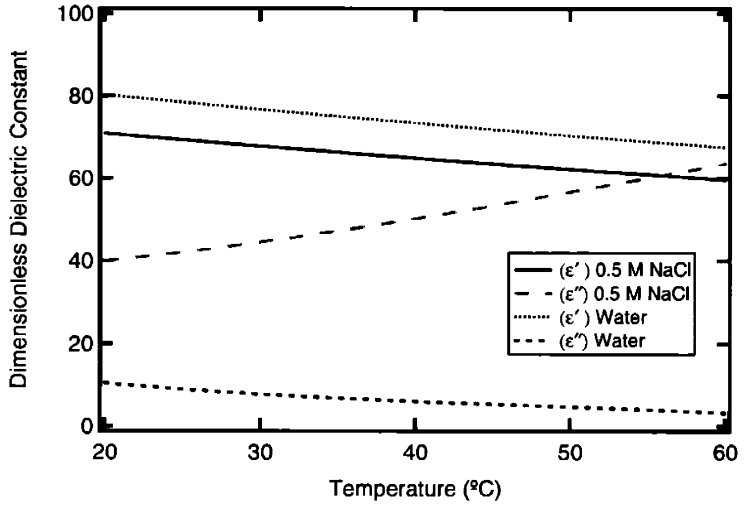

Figure 69: Dielectric properties of Water and 0.5 Molar NaCl in Water at different temperatures. (f=2.45 GHz)

The presence of salt in water changes the absolute value of the dielectric properties and the behavior of the dielectric loss (ε″) with temperature. There is a moderate decrease in the dielectric constant (ε′) of salt water compared to that of pure water and a substantial increase in the dielectric loss (ε″). The dielectric loss (ε″) determines the effectiveness of the absorbance of microwaves; with an increase in dielectric loss, microwave heating will increase. But even more importantly, the slope of the temperature response of ε″ is also reversed. This change in slope implies that as the salt solution heats, the absorbance of microwaves will increase, the opposite of the behavior of water. This temperature response of dielectric loss leads to the phenomenon of runaway heating in a microwave system in which the rate of heating increases with time (for a

constant microwave power input), and which is one of a myriad of issues that make controlled applications of microwave heating difficult.[1, 11]

5.4.3 Experimental Procedures

In order to explore the changes in microwave heating of water in the presence salt, a set of experiments was conducted over a range of salt solutions (0.05 M, 0.1 M, 0.2 M, 0.5 M) and pure water. The microwave frequency was 2.45 GHz and the input power was set to 400 W. The total heating time for each sample was 25 seconds. The sample cell was filled with 30 ml of a solution with the fluorescent probes, Dextran labeled Rhodamine B (10,000 MW anionic, 95% purity from Molecular Probes) at 0.3 μM and Rhodamine 110 (99% purity from Sigma-Aldrich) at 0.03 μM. The laser was run at 488 nm with a power setting of 620 mW. The exposure time of both the laser and the cameras was set to 100 ms and a capture rate of 2 Hz was used. The sample cell was loaded and allowed to equilibrate for 1.5 hours. A sequence of 10 images was captured of the room temperature sample and then the microwave was turned on for 25 seconds. The camera and laser shutter timing were controlled by the computer and the microwave start and stop were triggered manually. Sixty images were captured in each experiment with the first 10 images used as the constant temperature calibration image.

The captured images were of a cross-section of the sample cell with a pixel size of 41 μm.

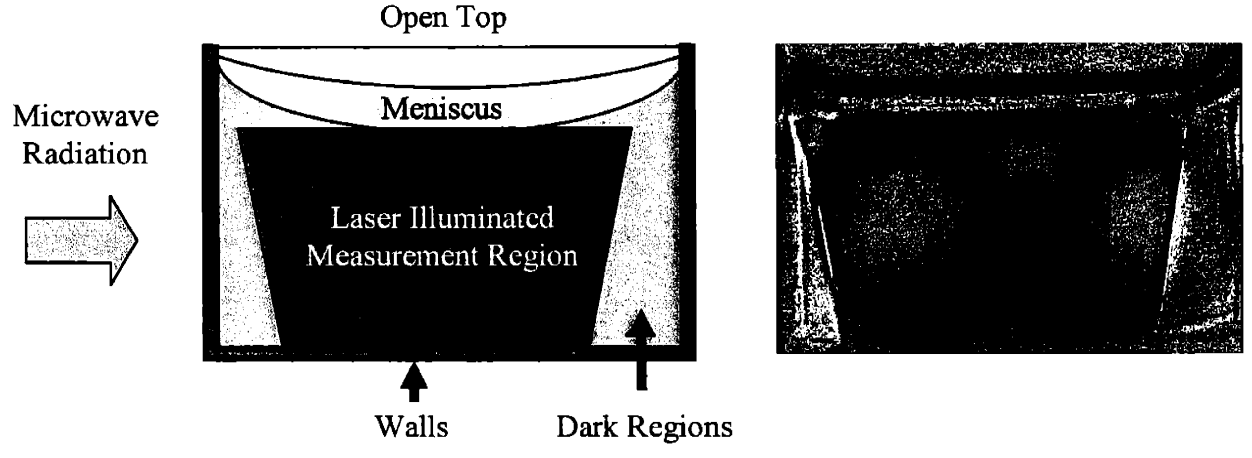

Figure 70: Different regions seen in a typical 2D image.

A drawing of the majors features seen in the images captured is shown with an actual image in Figure 70. Although the dark regions do not yield precise temperature measurements, general trends in temperature can be seen in these regions. The microwave radiation approaches the cavity from the left, but inside the cavity, reflections create an electric field distribution that is not limited to the leading edge of the sample. Microwave heating occurs throughout the sample, its power determined by the dielectric properties of the sample and the cavity geometry. An example of this can be seen in Figure 70 where heating occurs on both sides of the sample cell, with no clear indication of the direction that microwaves enter the cavity. There is an obvious optical anomaly seen in Figure 70, the presence of lines running parallel to the laser path, which are the result of mismatches between the interference pattern formed by etalons during calibration and the interference pattern formed by the etalons in the actual experiment. These mismatches occur because of slight mechanical errors in positioning of the sample cell and because of the thermal expansion of the glass cell walls during the microwave heating, which would change the interference pattern. An example of the increase in the strength of the etalon lines on heating is clearly shown in Figure 71.

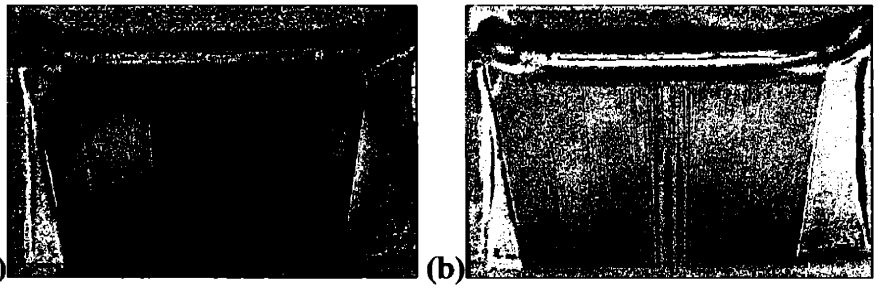

Figure 71: Line formation in images due to thermal expansion of the glass sample cell. (a) 2.5 seconds of heating (b) 7.5 seconds of heating.

In Figure 71a, the image shows few lines, especially near the centerline after 2.5 seconds of heating, whereas there are significantly more lines in the centerline of Figure 71b, after 7.5 seconds of heating. The line pattern at the center of the image becomes more pronounced as the microwave heating progresses due to the thermal expansion of the sample cell floor. These line artifacts are concentrated in the center of the image because the laser light is perpendicular to the sample cell floor at this point, which leads to the greatest magnitude of interference. The etalon formed by the sample cell floor does cause other lines to form beyond the center, but the pattern

is at a higher frequency with much lower magnitude and has less of an affect on the image. From this example, we can expect to recover higher quality images at earlier times in the microwave heating process and progressively reduced quality as the heating process continues.

5.4.4 Results

Pure Water

The results for microwave heating of pure water are seen in Figure 72. The major changes in the shape of the heated regions are seen within the first 7.5 seconds of heating.

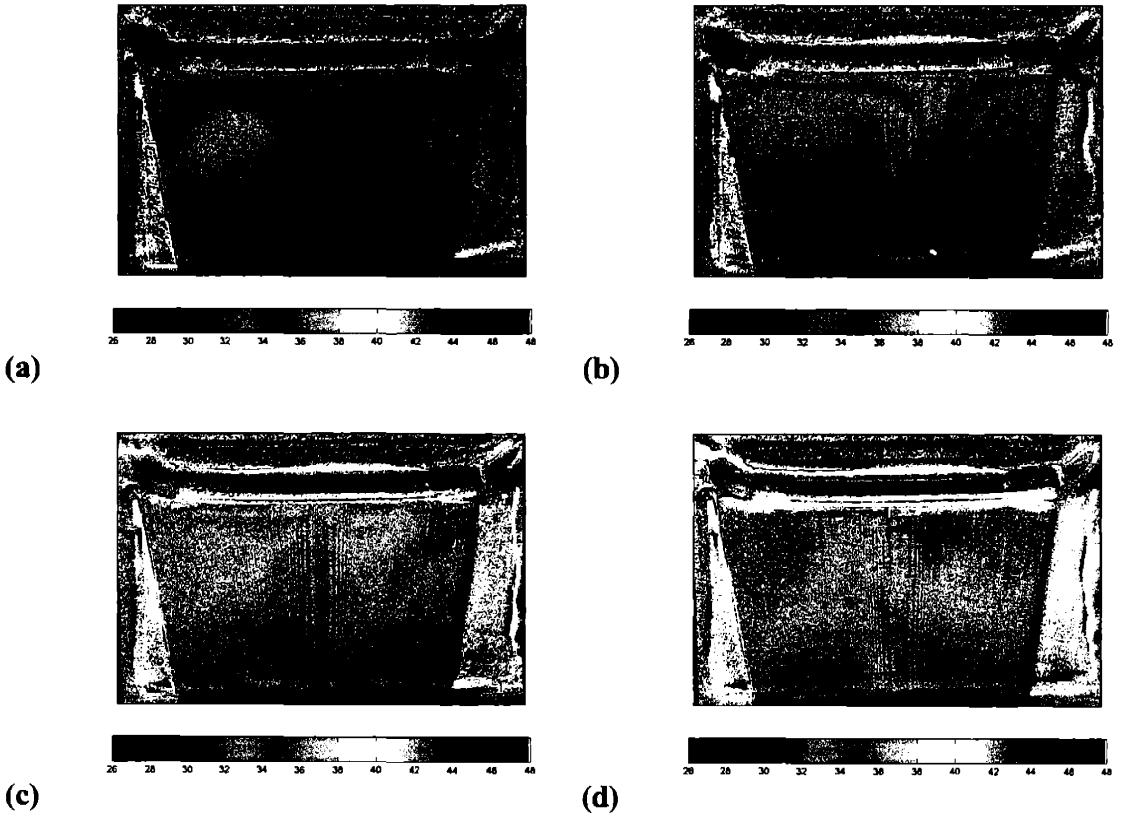

Figure 72: Results from microwave heating of pure water at different times (a) 2.5 seconds, (b) 3.5 seconds, (c) 5 seconds, and (d) 7.5 seconds.

Figure 72a shows the temperature distribution 2.5 seconds after the microwave generator had been started. The heating profile features two initial regions of heating, or nodes, and these nodes are roughly static until natural convection moves them upwards. This quasi-static structure is the closest approximation to the electric field distribution at the onset of heating by the microwave. Both leading and trailing heating nodes then rise, split, and spill over into a mushroom-like structure as seen in Figure 72b. This is followed by a mixing process in Figure 72c which moved towards a more uniform distribution in Figure 72d. The mixing process stalls after the initial convection pattern forms and thereafter conduction is the dominate form of heat transfer. After 25 seconds of heating, the cell is still not uniformly mixed as shown in Figure 73.

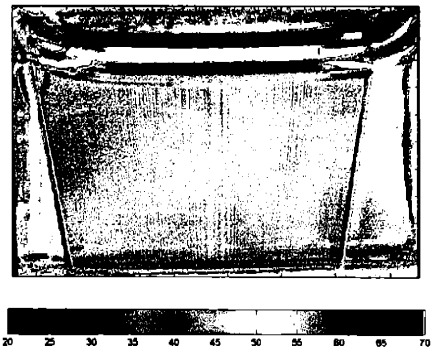

Figure 73: Results from microwave heating of pure water after 25 seconds of heating.

The results of the experiment in water demonstrate the volumetric heating behavior of microwaves and convection patterns that formed as a result of the localized heating spots. The challenge of uniformly heating a sample with microwaves is clearly shown in the final images where, after 30 seconds of heating, large temperature differences still exist in the temperature profile.

0.05 M Salt Water

The results for microwave heating of a solution of 0.05 M salt solution are shown in Figure 74.

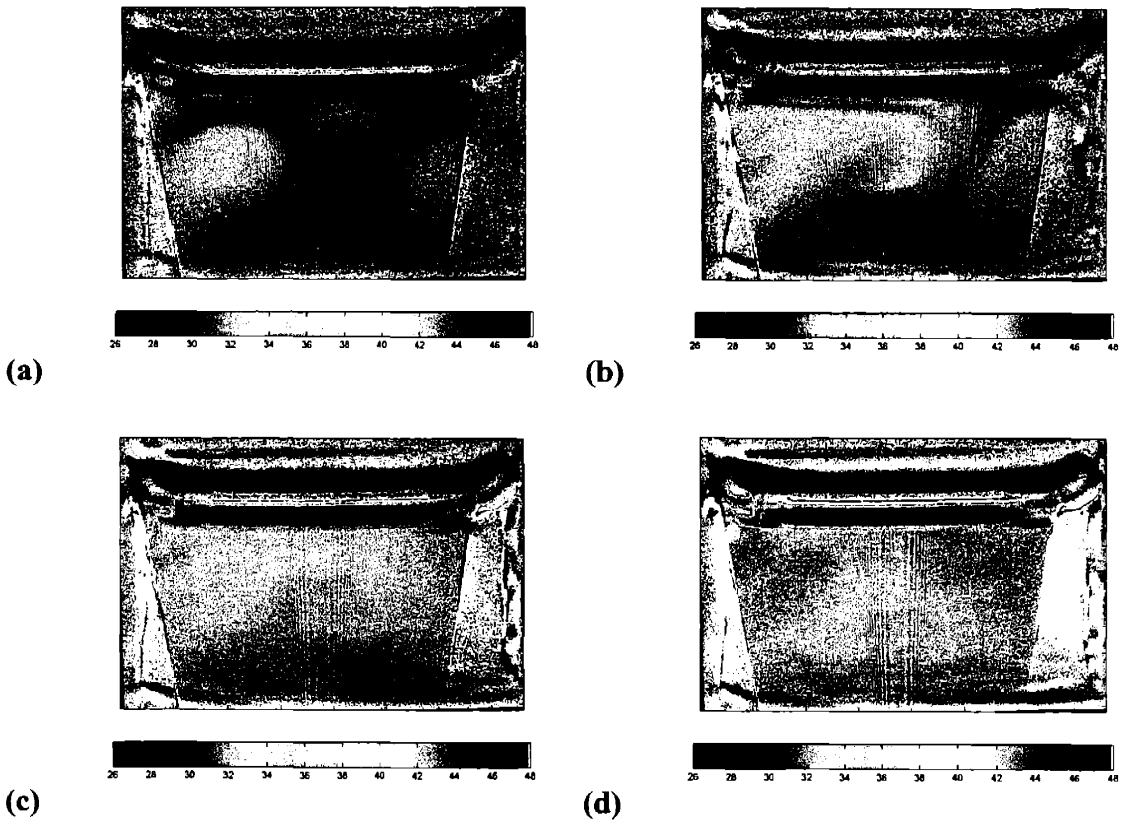

Figure 74: Results from microwave heating of a 0.05 M salt solution at different times (a) 2.5 seconds, (b) 3.5 seconds, (c) 5 seconds, and (d) 7.5 seconds.

The lowest salt concentration solution evolved in a similar fashion to that of pure water. The most significant difference can be seen in Figure 74a, where the heating node at the leading edge grew relative to the trailing node when compared to the water case.

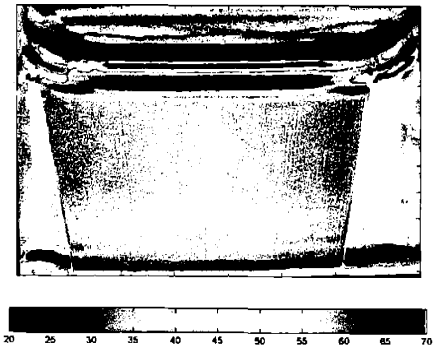

Figure 75: Results from microwave heating of a 0.05 M salt solution after 25 seconds of heating.

The shift in heating towards the leading edge removed the mushroom formation in the trailing edge. The mixing followed the mushroom formation and the subsequent images were similar to those seen in the water system. As with the water case, the convective mixing stalls, and the final solution is not uniform in temperature. (Figure 75) A thermocouple was inserted into the cell after heating to provide a qualitative check on the temperature in the sample cell. The temperature measurements were taken in the centerline of the sample cell at the top of the cell and near the bottom. The results were 58.7 °C in the upper region and 53.2 °C in the lower region. Although there is considerable error in this measurement from mixing caused by the thermocouple and the time difference between the image in Figure 75 and the thermocouple measurements, the temperature difference does confirm the existence of the cooler region in the bottom center region of the cell.

0.1 M Salt Solution

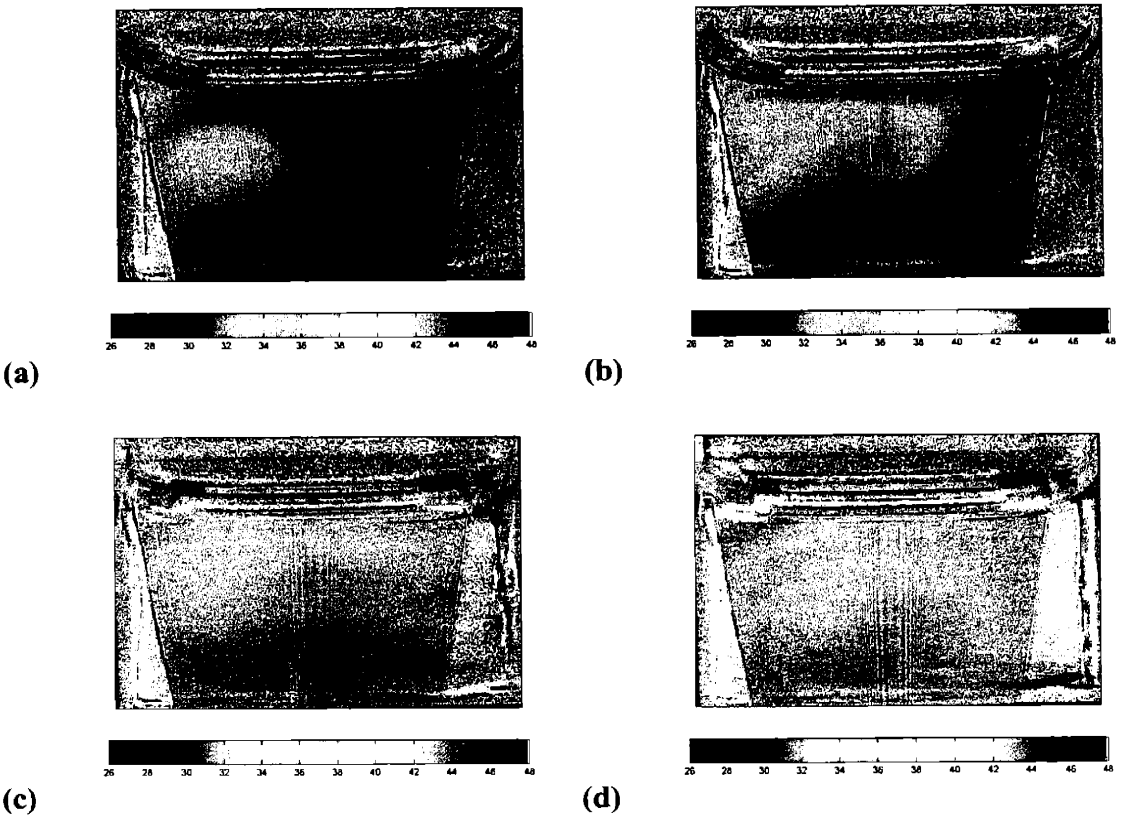

Figure 76: Results from microwave heating of a 0.1 M salt solution at different times (a) 2.5 seconds, (b) 3.5 seconds, (c) 5 seconds, and (d) 7.5 seconds.

The 0.1 M salt solution images continue the trend seen in 0.05 M salt solution of the shift in heating to the leading edge. The images captured for the 0.1 M system are shown in Figure 76. In the 0.1 M solution, the only prominent heating was seen in the leading edge heating node. There is some indication that heating is occurring in the corners of the cell at the leading edge. The mushroom forms, elongates and spreads across the upper portion of the cell. The convective flows begin, but stall and the final stages of heat transfer observed are due to conduction. The final image again shows a non-uniform final temperature profile after 25 seconds of heating. (Figure 77)

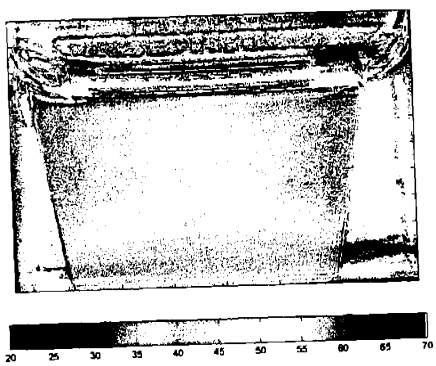

Figure 77: Results from microwave heating of a 0.1 M salt solution after 25 seconds of heating.

0.2 M Salt Solution

The 0.2 M solution experiments complete the pattern of heating that is concentrated on the leading edge. The results of 0.2 M are shown in Figure 78. The heating process now forms a bullet shape that rises and proceeds across the upper region of the cell before hitting the opposite wall. This result is similar to the simulation results by Ayappa[4] on oil inside a square cavity where one dominant interior heating node existed. Although the quantitative data cannot be extracted from the regions outside of the laser illumination, qualitatively we can observe the flow pattern as the bullet hits the far wall. Once the bullet form comes in contact with the wall it drops down and begins the mixing process. In Figure 78c a small vestige of the mushroom edge can be seen.

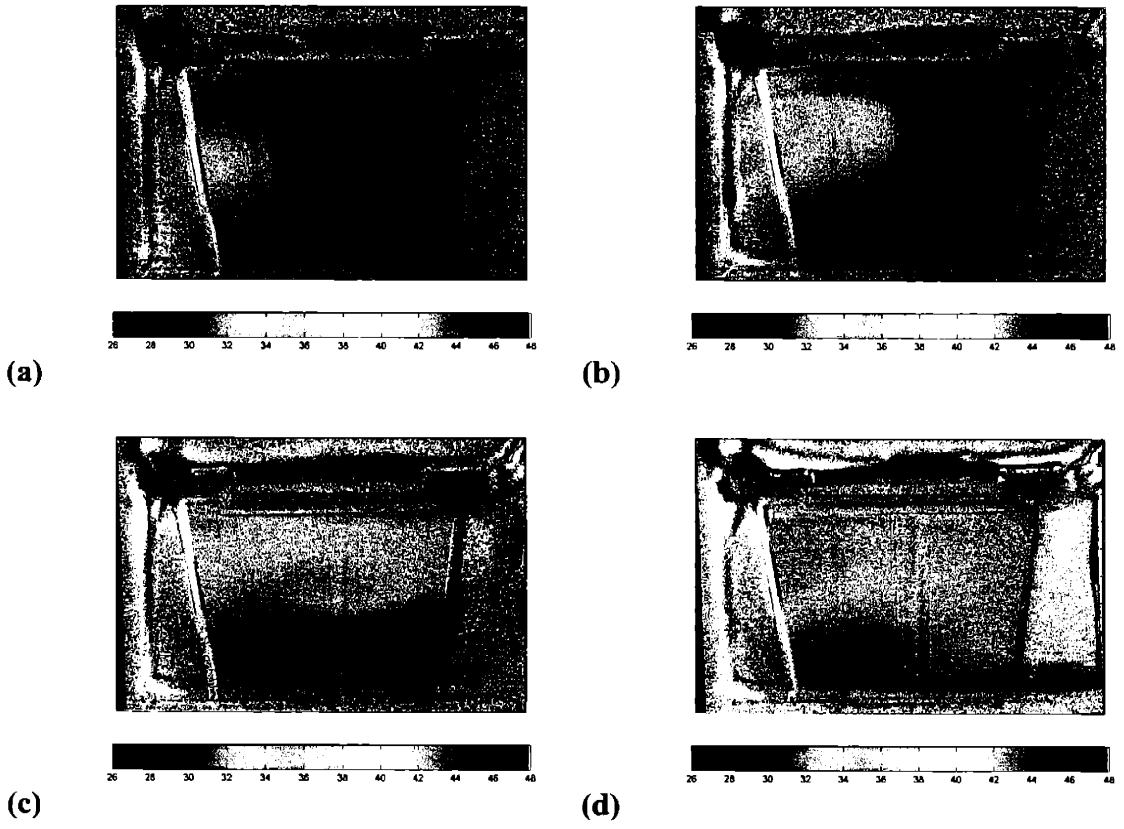

Figure 78: Results from microwave heating of a 0.2 M salt solution at different times (a) 2.5 seconds, (b) 3.5 seconds, (c) 5 seconds, and (d) 7.5 seconds.

The final image of the 0.2 M salt solution heating shows a significantly more uniform temperature profile than the previous concentrations of salt. (Figure 79) However, there is still a characteristic lower temperature zone in the middle of the sample cell.

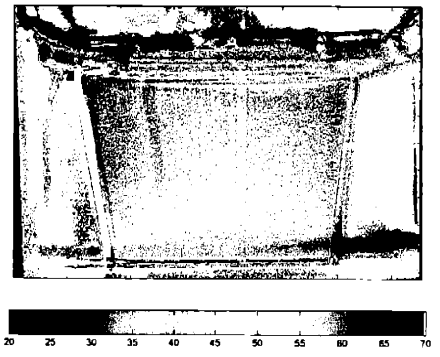

Figure 79: Results from microwave heating of a 0.2 M salt solution after 25 seconds of heating.

0.5 M Salt Solution

At the highest concentration tested, 0.5 M NaCl, there is no evidence of the mushroom formation. The image sequence is shown in Figure 80.

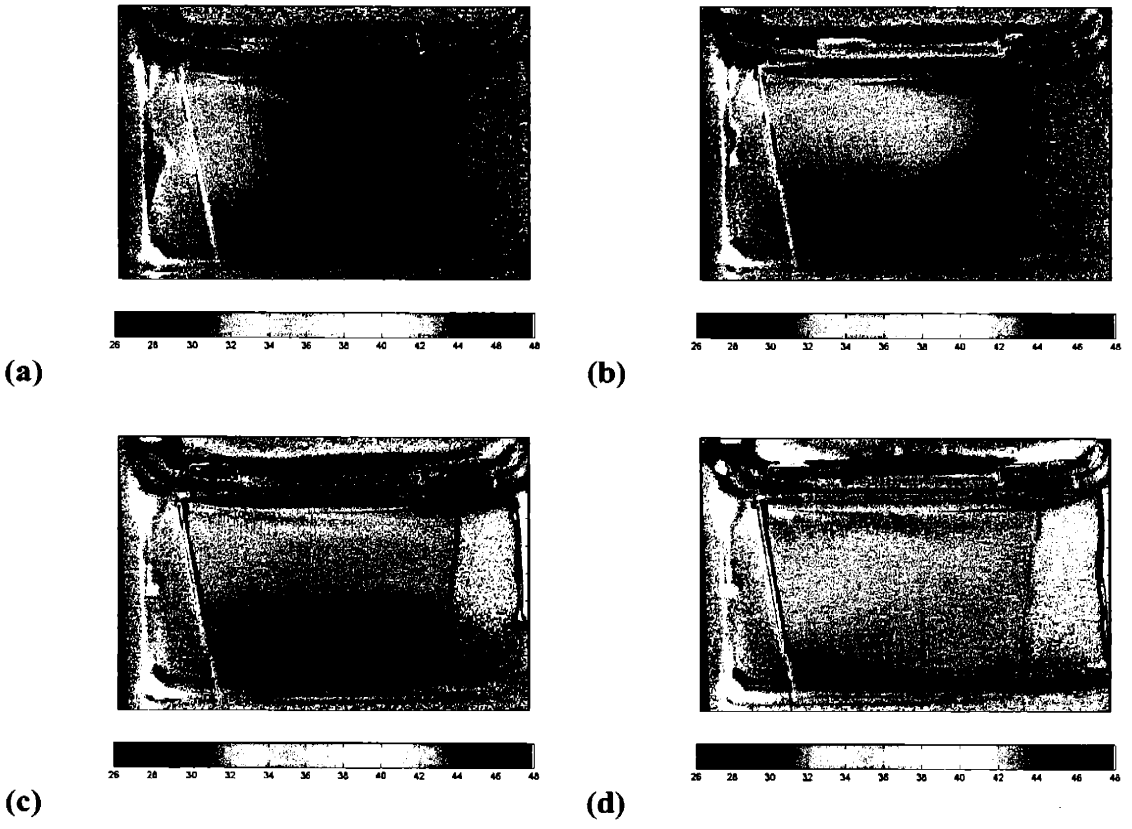

Figure 80: Results from microwave heating of a 0.5 M salt solution at different times (a) 2.5 seconds, (b) 3.5 seconds, (c) 5 seconds, and (d) 7.5 seconds.

With 0.5 M of salt, the heating is firmly fixed in the leading edge as seen in Figure 80a. The heated region rises and drives across the upper portion of the cell in the form of a bullet. As in the 0.2 M case, the plume hits the far wall, beyond the laser illuminated region, and then moves down and begins mixing. The final image after 25 seconds of heating of the 0.5 M salt solution shows a substantially different temperature profile from the pervious salt concentrations. (Figure 81) The mean temperature is lower than the other salt solutions and the higher temperature regions are at the perimeter of the cell. This suggests that the high salt concentration is shielding the interior of the cell from heating.

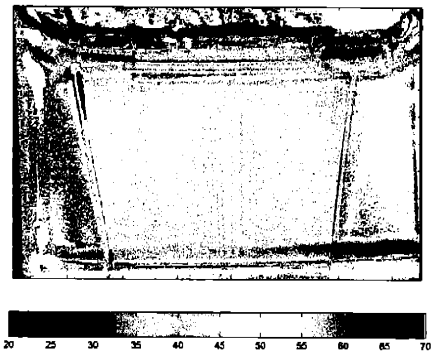

Figure 81: Results from microwave heating of a 0.5 M salt solution after 25 seconds of heating.

The trend in the salt solutions is a shift of heating from the interior towards the leading edge of the sample cell. This observation makes sense in light of the increase in conductivity of the solution with an increase in salt concentration. The higher conductivity solutions act more like the walls in the microwave applicator, reflecting microwaves and allowing less penetration into the solution. In addition, the increased dielectric loss of salt water solution would decrease the penetration depth of microwaves. The result of the property changes is a reduction of the interior heating nodes, which changes the convection patterns observed.

Dextran Solution

Microwave heating and the subsequent mixing process occur on a fast time scale. A potential approach to study microwave heating in depth is to use solutions that have higher viscosity. Increasing the viscosity of the system will slow the effects of convection and allow more detailed observations to be made of the heating and flow patterns. Dextran was chosen to increase viscosity because the Rhodamine B probe molecule is already bonded to a Dextran polymer. This avoids any issues of chemical compatibility and changes to the temperature response of the probe. The results in Figure 82 are for 10% by weight of 100,000-200,000 MW Dextran polymer in water. These results clearly show how the increased viscosity slows the entire mixing process. In Figure 86b the restricted movement results in an increased holding time near the initial heating regions. This greatly increased the heating of the sample at the node locations.

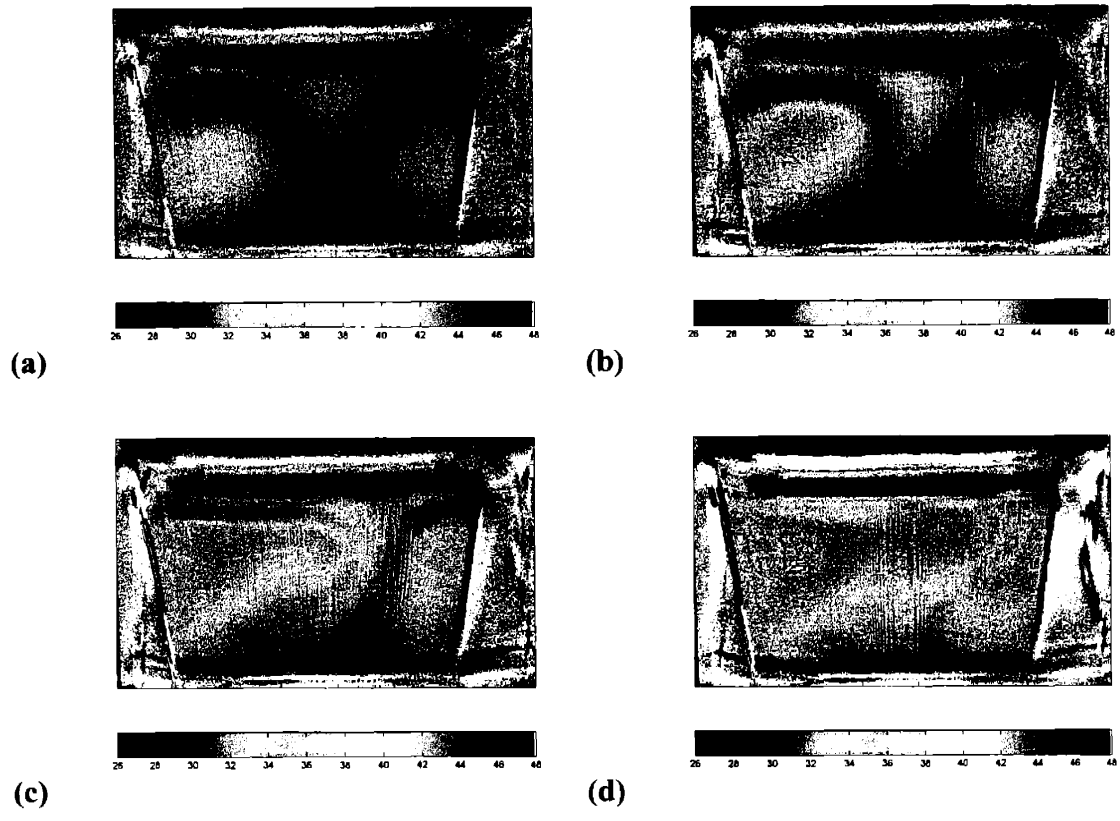

Figure 82: Results from microwave heating of a dextran solution (10% by weight) at different times (a) 2.5 seconds, (b) 3.5 seconds, (c) 5 seconds, and (d) 7.5 seconds.

The center-top node has a more prominent effect than witnessed in the other systems, persisting even after 5 seconds of heating (Figure 82c). The convection patterns observed in the dextran sample are a hybrid of the patterns observed in the other systems.

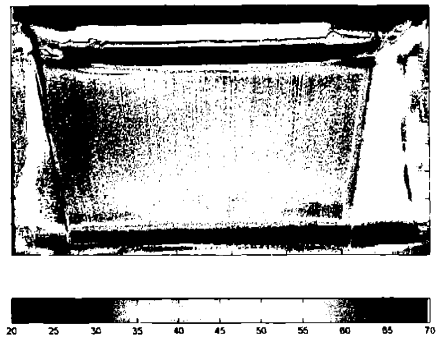

Figure 83: Results from microwave heating of a 10 wt% Dextran solution after 30 seconds of heating.

The characteristic mushroom formation begins in Figure 82c but then transitions into a bullet pattern in Figure 82d. The results after 25 seconds of heating are shown in Figure 83. This final image gives some insight as to how microwave heating proceeds. The leading edge shows the highest temperatures, suggesting that microwave heating continues to be strongest there, while the trailing edge shows lower heating rates and the lowest rates are observed at the bottom center of the sample cell.

The experiments were successful in capturing the dynamic process of microwave heating for water and salt solutions. Microwave heating in the cavity was observed to concentrate in distinct nodes. The interior nodes were observed to fade as the salt concentration increased and nodes at the leading edge appeared to grow in strength with the increase in salt concentration. The conclusions are consistent with expectations that the increase in salt would increase conductivity and dielectric loss, blocking microwaves from the interior regions. The experiment with a higher viscosity solution was observed to increase spot heating by reducing the speed of convection and create a unique initial convection pattern that is consistent with that observed in the lower viscosity systems.

5.5 Simulation of 2D Experiments

5.5.1 Theoretical Background

Microwave heating is governed by Equation 5-1 which is derived from the Poynting theorem.[12]

$$Q = \frac{1}{2}\omega\varepsilon'' E \cdot E^* \qquad (5\text{-}1)$$

Here, ω is the angular frequency of the microwaves, ε'' is the dielectric loss of the heated material and E is the electric field. From this equation we see that microwave heating only depends on the electric field component of the electromagnetic wave. The electric field is computed by solving Maxwell's equations:

$$\nabla \times \mathbf{E} = -\frac{\partial \mathbf{B}}{\partial t} \tag{5-2}$$

$$\nabla \times \mathbf{H} = \mathbf{J} + \frac{\partial \mathbf{D}}{\partial t} \tag{5-3}$$

$$\nabla \cdot \mathbf{D} = \rho \tag{5-4}$$

$$\nabla \cdot \mathbf{B} = 0 \tag{5-5}$$

for the regions both inside the sample and outside the sample. The boundary conditions for the interface between the interior and exterior of the sample are given by the following equations: [12]

$$\mathbf{n} \cdot \left(\varepsilon_1^* \overline{\mathbf{E}}_1 - \varepsilon_2^* \overline{\mathbf{E}}_2\right) \tag{5-6}$$

$$\mathbf{n} \times \left(\overline{\mathbf{E}}_1 - \overline{\mathbf{E}}_2\right) \tag{5-7}$$

$$\mathbf{n} \cdot \left(\overline{\mathbf{H}}_1 - \overline{\mathbf{H}}_2\right) \tag{5-8}$$

$$\mathbf{n} \times \left(\overline{\mathbf{H}}_1 - \overline{\mathbf{H}}_2\right) \tag{5-9}$$

where **n** is the unit normal vector from sample to exterior, ε^* is the complex dielectric constant and **H** is the magnetic field. The subscript 1 refers the outside of the sample and the subscript 2 represents the interior of the sample. The solution of Maxwell's equations is usually performed using a finite element solver. A full solution of microwave heating requires coupling Maxwell's equations with the heat-transfer equations.[13] With temperature independent dielectric properties, the electric field is solved and the microwave heating enters the heat-transfer equations using Equation 5-1 as a volumetric heat source. However, the dielectric constant changes significantly with temperature for many materials, which couples Maxwell's equations with the heat-transfer equations, greatly increasing the difficulty of the problem.

5.5.2 Simulation of Salt Solutions

Our primary interest was in the initial heating patterns prior to the onset of convection and this simplifies the model greatly by allowing us to ignore heat-transfer. The model is further simplified by assuming a homogeneous dielectric constant and performing the computations only in 2D. A commercial CFD package, FemLab, was employed to solve Maxwell's equation and determine the electric field strength. The microwaves were modeled as waves that have the magnetic field component in the plane of the simulation and the electric field component normal to the plane of the simulation. Because of the assumptions in the model of initial heating, we

were only interested in the relative power intensity distribution, as given by Equation 5-1, for the different experiments that were performed. Simulations were performed for water and the four experimental salt solutions (0.05 M, 0.1 M, 0.2 M, 0.5 M). The dielectric properties of salt water solutions have been studied extensively in the literature, [5-9] and the conductivity and dielectric properties were computed using relations developed by Stogryn.[10] (Table 2)

	Real Relative Dielectric Constant (ε')	Conductivity (σ) (S/m)	Relaxation Time (τ) (ps)
Water	78.34	0.002	8.1
0.05 M Salt	77.36	0.514	8.1
0.1 M Salt	76.39	1.016	8.1
0.2 M Salt	74.51	1.989	8.1
0.5 M Salt	69.3	4.68	8.0

Table 2: Material properties used in 2D FemLab model of the microwave cavity

The effective dielectric loss (ε''), contains the conductivity and is given by the following equation:

$$\varepsilon''_{effective} = \frac{(\varepsilon'_L - \varepsilon'_H)\omega\tau}{1+\omega^2\tau^2} + \frac{\sigma}{\varepsilon_0\omega} \qquad (5\text{-}10)$$

where ε'_L is the low-frequency real relative dielectric constant, ε'_H is the high frequency limit real relative dielectric constant and ε_0 is the permittivity of free space. The value of ε'_H is suggest by Stogryn[10] to be 4.9 and that value is used throughout all the simulations. The dielectric loss was entered into FemLab as part of the complex dielectric constant and the walls of the waveguide were treated as perfect conductors.

It has been shown by Zhao that the relative power intensity is a good indicator of the relative heating rates throughout a microwave heated sample.[14] In Figure 84, the relative power intensity is shown for each sample from the simulation is shown next to the corresponding experiment. The experimental results were chosen at a point in time before significant motion of the heating nodes was observed, which allowed for maximum visibility of heated areas without significant convection effects. The time that was chosen for all images was 2.5 seconds of heating.

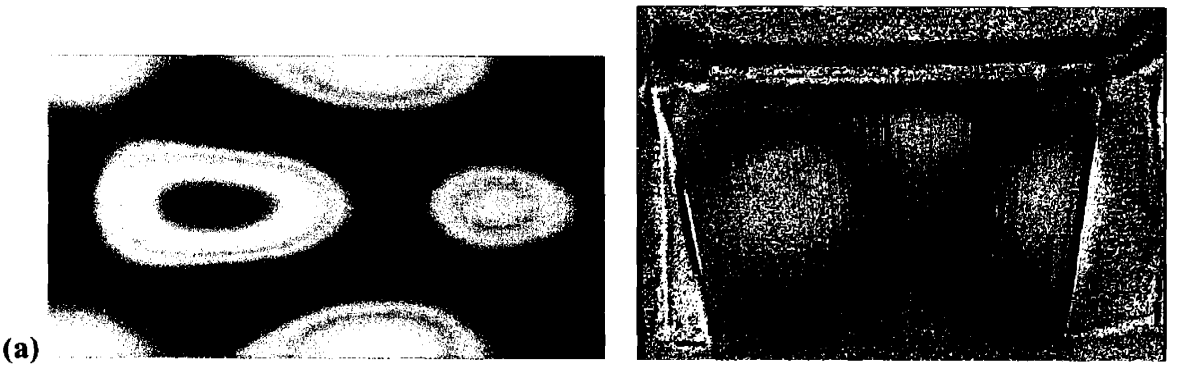

(a)

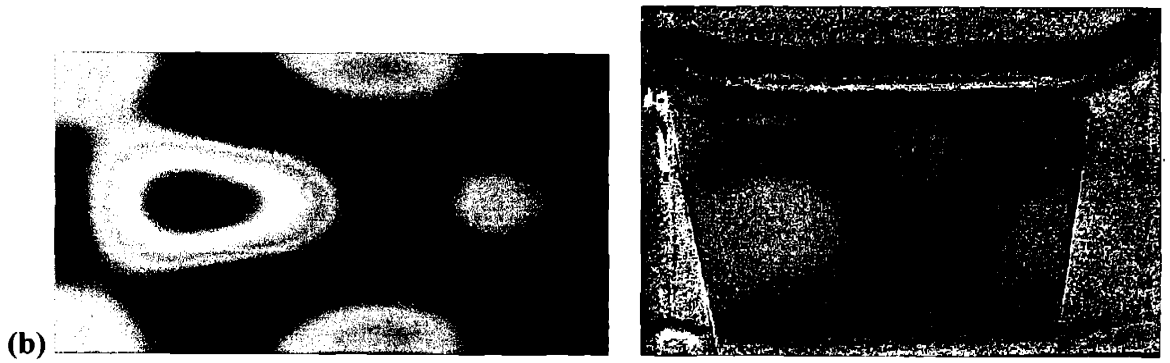

(b)

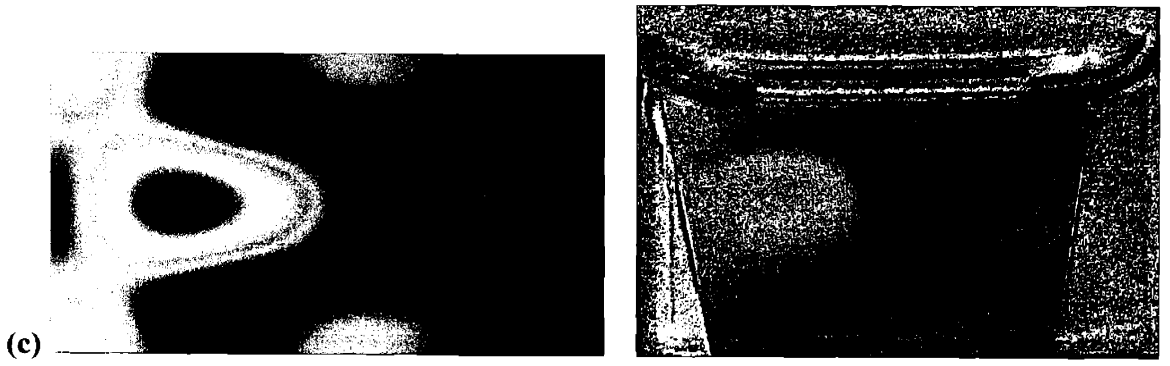

(c)

(d)

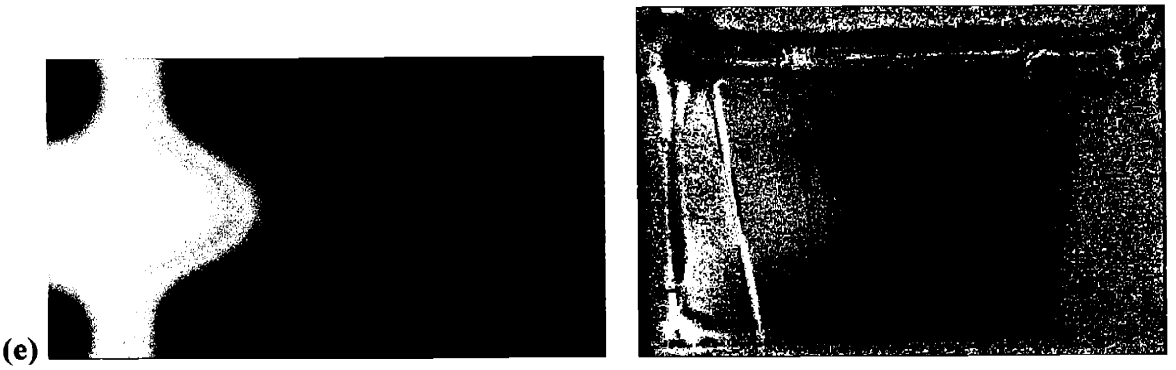

Figure 84: Model relative microwave heating rates (left column) compared with experimental results after 2.5 seconds of heating (right column). (a) water, (b) 0.05 M salt, (c) 0.1 M salt, (d) 0.2 M salt, (e) 0.5 M salt.

For the water case in Figure 84a, the model predictions show two major heating nodes in the interior, two other nodes at the top and bottom in the center of the cell and two minor nodes at the corners of the cell on the leading edge. The experimental result is in good agreement with the model, with the interior, side, and one corner node accounted for. The remaining corner node is outside of the laser illumination area and thus beyond the observation region. The dual interior heating nodes in the water experiment is similar to one seen in finite-difference time-domain simulation of a resonant microwave cavity by Liu[15], while corner heating is commonly expected in microwave heating.[3]

The change in dielectric properties of a lossy material in a microwave field has a substantial effect on the electric field and, by extension, the heating in the microwave cavity. The positions and intensity of heating nodes formed in the sample have been shown through simulations by Dibben to vary greatly with the dielectric properties.[16] The effect of an increase in salt concentration on the remaining model images is shown in Figure 84(b-e). In general, the salt solution images depict a gradual loss of power in the trailing interior, top and bottom nodes compared to pure water. In contrast the corner nodes at the leading edge of the sample cell increase in power, while the leading interior node maintains its intensity until the highest salt concentrations. The shift to the leading edge is likely the result of the higher conductivity of solutions as the salt concentration increases, which shields the interior regions from microwaves. While most of the activity of the corner nodes lies outside of the observable area, in Figure 84b

and Figure 84c the upper corner node is visible and clearly shows in increase from 0.05 M to 0.1 M salt concentration as predicted in the model.

2D simulations were performed in FemLab to model the electric field distribution in the microwave cavity and thus the heating pattern. The model was simplified to have no temperature dependent parameters, which captured the essential features of the electric field in the microwave cavity at the initial heating phase. The experimental results for water and each salt solution were found to be in close agreement with the model, showing growing prominence of the leading edge nodes and decreasing prominence of interior nodes with the increase in salt concentration.

5.6 3D Experiments

Although 2D experiments are an essential step in understanding microwave heating, 3D experiments are needed to verify models of microwave heating. The fluorescence thermometry instrument was built to provide some 3D capabilities.

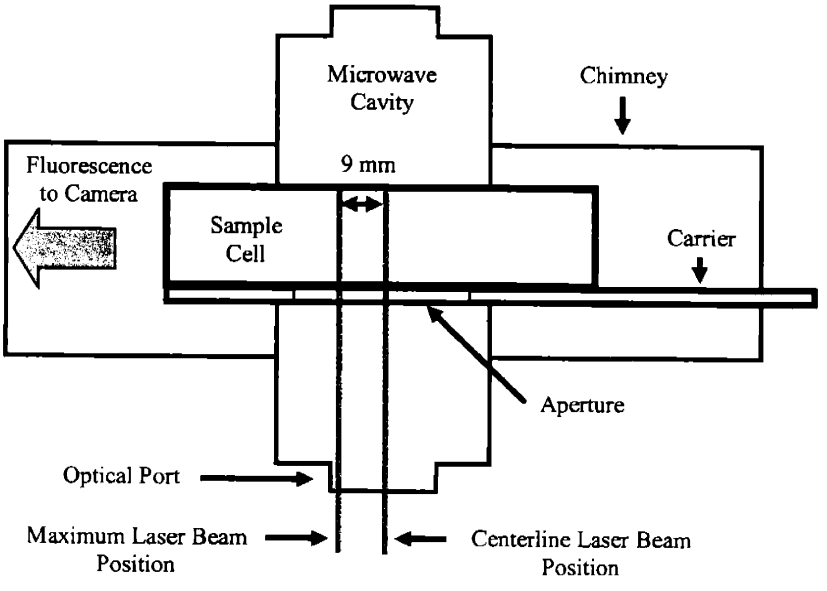

Figure 85: Schematic of 3D imaging in the microwave cavity

The same technique as in the original test instrument was used, where the cameras and dichroic filter are mounted on a motorized stage. This stage was coupled with the final mirror and positive lens of the laser expansion optical system. By moving the stage, both the cameras and the laser sheet are moved to a new position along the z-axis. Due to the high speed of microwave heating, a 3D image cannot be generated using a single experiment with this equipment. Instead, a sequence of experiments was performed at the same starting conditions, but at different positions along the z-axis. A total of five positions were explored for the water system and the 0.1 M salt solution. A drawing of the two end positions in the z-axis is shown in Figure 85. The cavity is symmetric and the electric field in the cavity was expected to be symmetric as well, so measurements were made only on half of the cavity. The size of the optical port on the microwave cavity restricts the locations that can be sampled within the cavity. The half width of the microwave cavity is 2 cm, however the length of the optical port allowed us to measure temperature only in the region 9 mm or less from the centerline. The final 5 sampling positions for 3D imaging range from the edge of the optical port to a point 3 mm beyond the centerline in 3 mm increments.

The experimental procedures followed for the 3D experiments were identical to the 2D procedures with the exception of moving the stage to different positions. Because there was no temperature control for the sample, there was some variation in the starting temperature of each sample. Additionally, the microwave start and imaging start are activated manually, so there was some timing uncertainty between samples. These sources of error may account for any absolute differences in the images for different 3D planes.

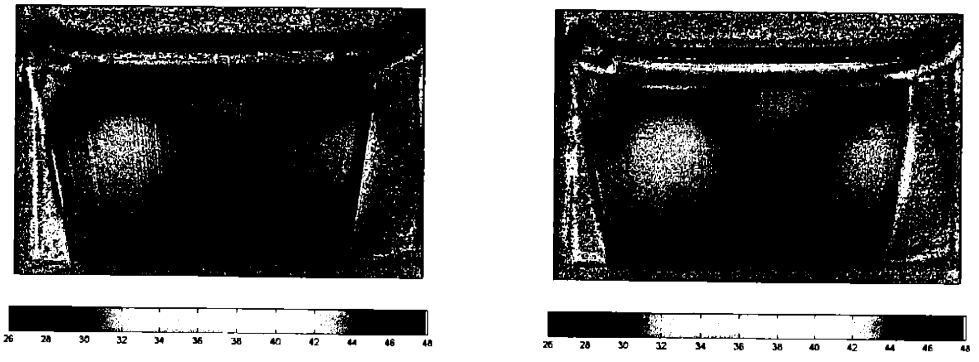

(a)

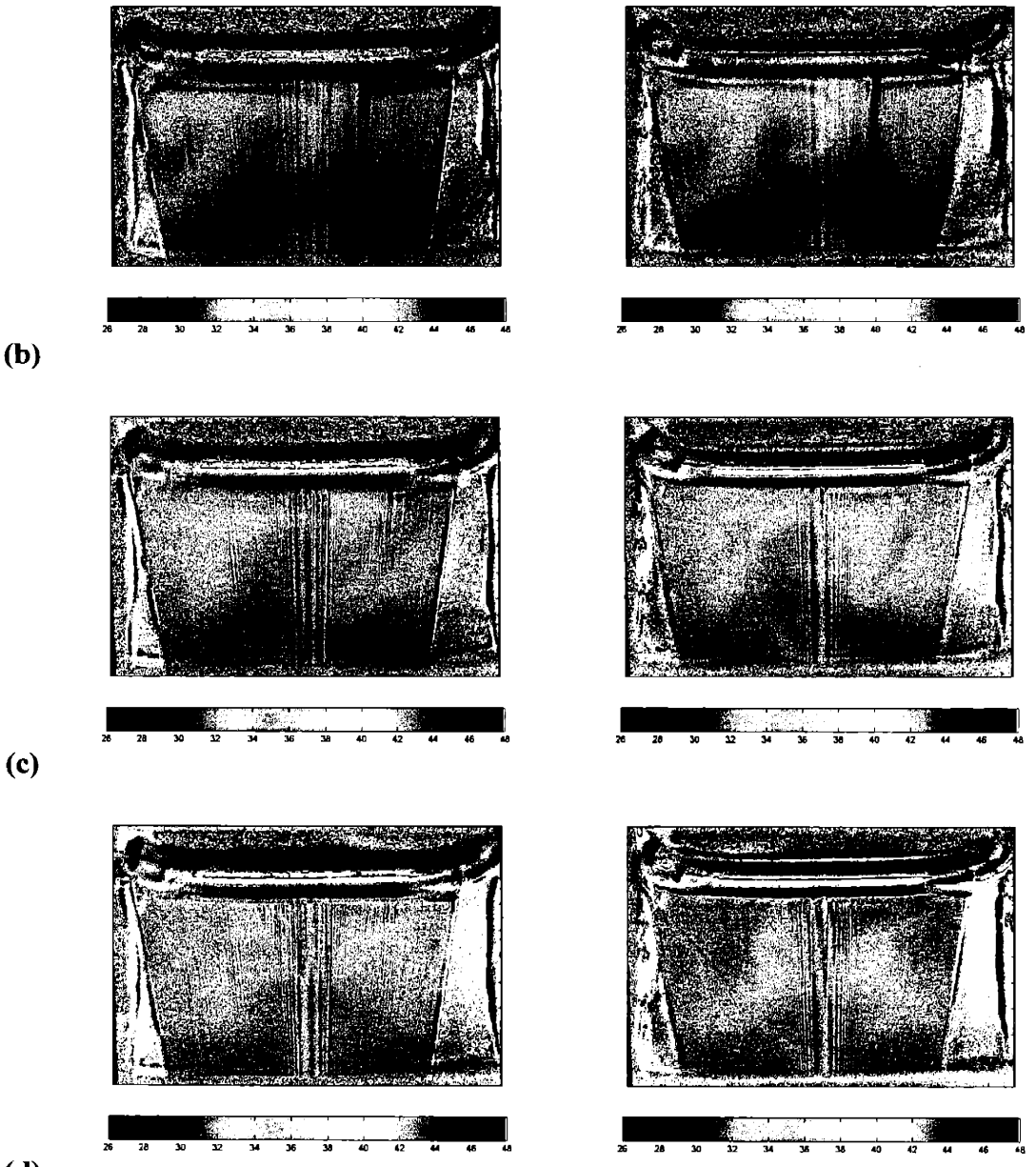

Figure 86: Results from microwave heating of a water solution at different times and positions (a) 2.5 seconds, (b) 3.5 seconds, (c) 5 seconds, and (d) 7.5 seconds. The images in the left column are near the centerline of the cavity and the images in the right column are 9 mm away.

The results for the water system are shown in Figure 86, with the left column of images showing the time evolution at the centerline of the cavity and the right column a position 9 mm closer to the camera. The heating patterns in the images are almost identical, time for time. The

mismatch in absolute temperature was possibly due to differences in timing of the measurements, but could reflect differences in heating rates in the cavity. Future upgrades to computer control of the experiment timing could resolve this question.

An identical 3D experiment was performed for a 0.1 M salt solution. The 3D images for positions near the centerline (left column) and 9mm away (right column) are shown in Figure 87.

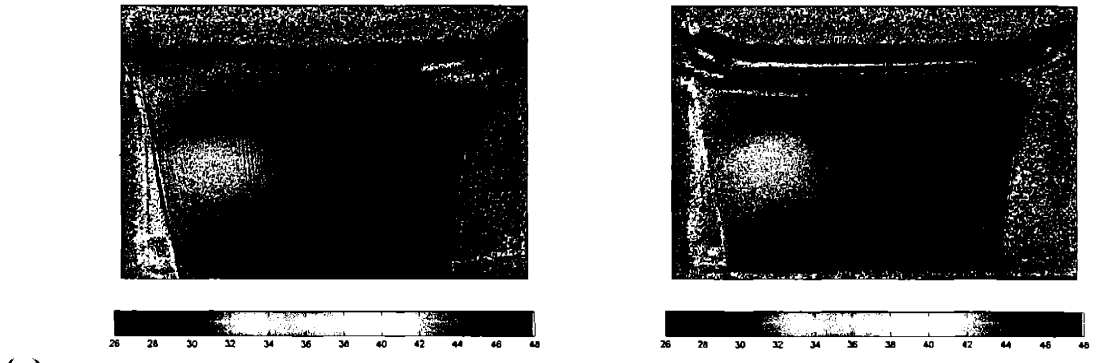

(a)

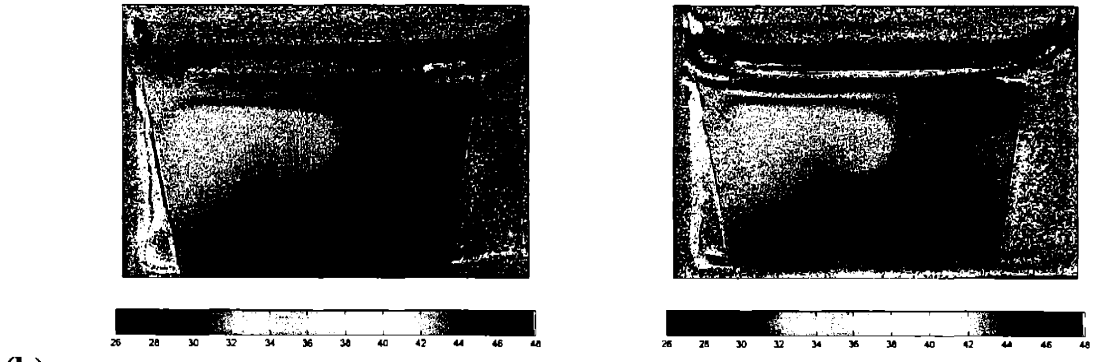

(b)

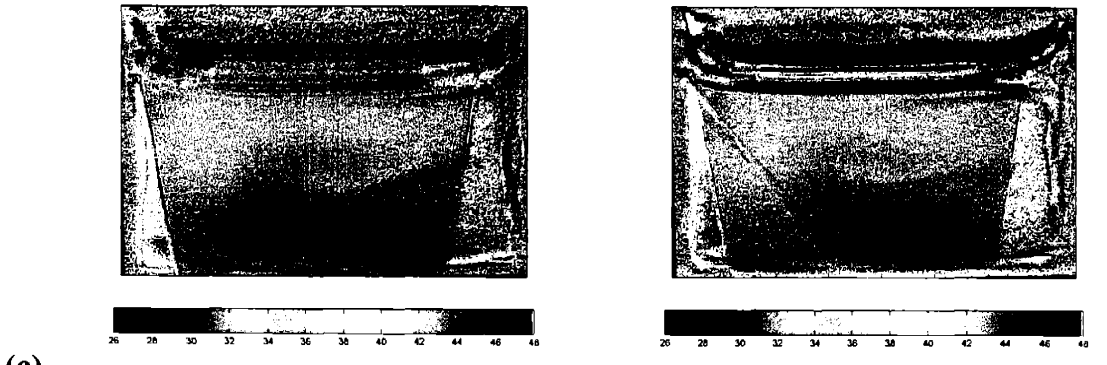

(c)

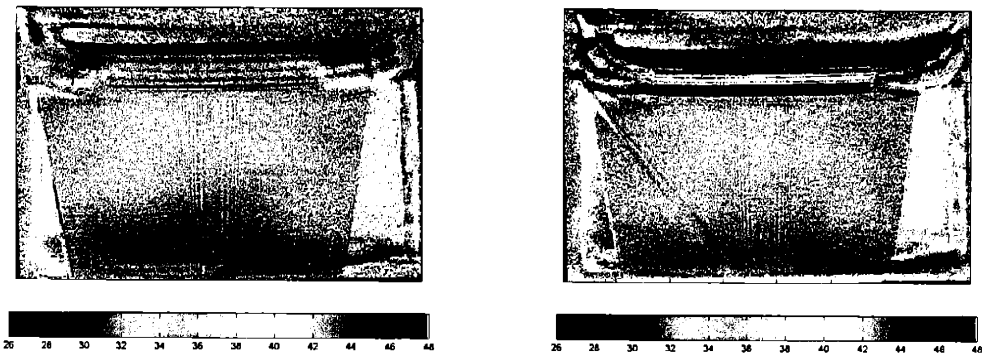

(d)

Figure 87: Results from microwave heating of a 0.1 M salt solution at different times and positions (a) 2.5 seconds, (b) 3.5 seconds, (c) 5 seconds, and (d) 7.5 seconds. The images in the left column are near the centerline of the cavity and the images in the right column are 9 mm away.

The salt solution images are almost structurally identical, like the water case. The absolute temperature differences are smaller than those observed in the water case. In Figure 87a, there was a slight difference in the position of the main node. One of the nodes has already begun to rise from buoyancy effects, indicating a timing mismatch in the start of the microwave heating. This suggests that the uniformity of heating in these positions was a real phenomenon and that the timing of the microwave start or imaging start could explain the difference in absolute temperatures.

The 3D images captured during microwave heating of both water and 0.1 M salt solution show remarkable similarity at each time increment. Although there was some difference in the absolute temperatures, this could be the result of differences in timing of the experiments and variations in the starting temperature. The lack of differences in the 3D images over the range of measurement positions was not entirely unexpected. The electric fields in the waveguide are in the TE_{10} mode and have their peak intensity near the center line and terminate to zero at the walls. Figure 88 shows the electric field strength in the x-y plane at different points inside the microwave cavity. However, the z-direction in the vicinity of the sample does not have a wall. In this region the chimney, as seen in Figure 89, is present and there will be some electric field penetration into the length of the port. This extended region for the electric field is likely to

broaden the electric field peak and result in a more uniform electric field in the z-axis. This uniform field in the z-axis would explain the small change in heating observed in the 3D images.

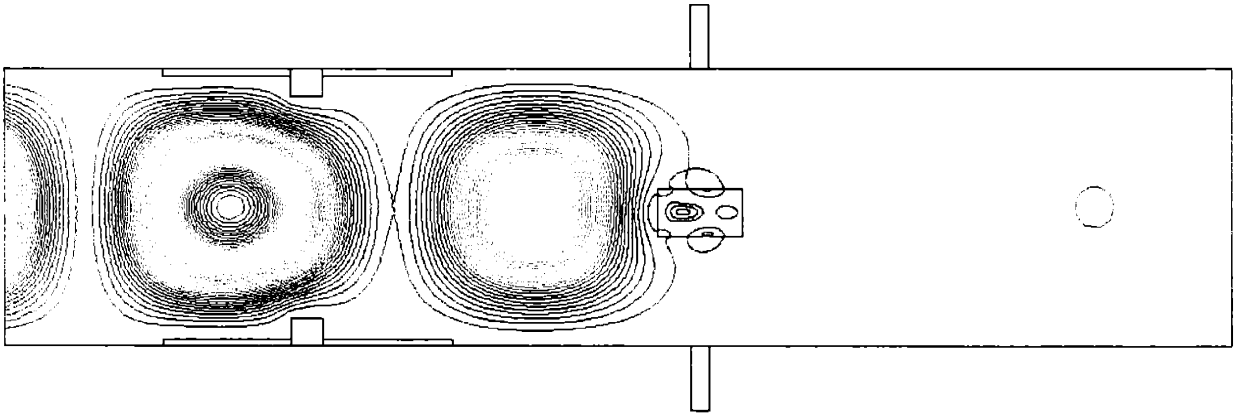

Figure 88: Contour plot of the calculated electric field ($E \cdot E^*$) strength in the waveguide.

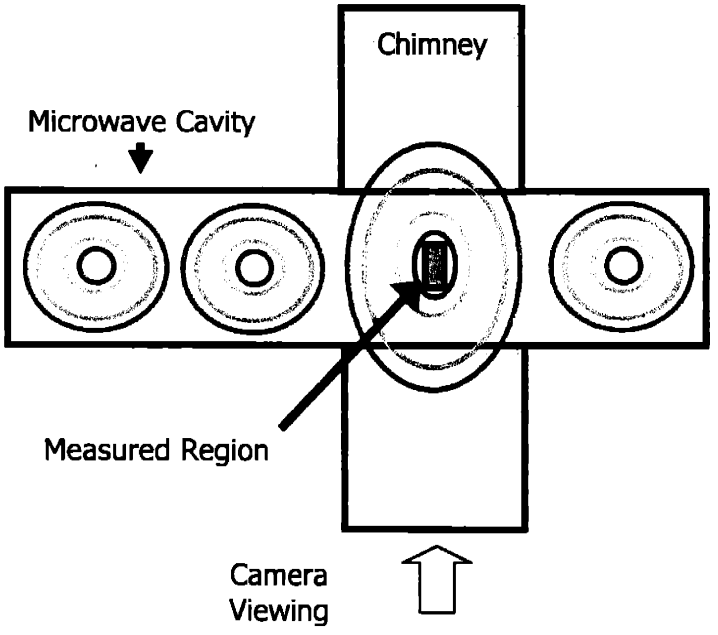

Figure 89: Expansion of the electric field into the chimney, resulting in a uniform field distribution in the region of 3D measurement.

5.7 Conclusions

In this chapter we have shown the successful application of the fluorescence thermometry instrument developed in preceding chapters to the task of measuring temperature in microwave heated sample. A microwave plasma applicator was successfully adapted for use with the fluorescence thermometry instrument. Investigations were performed into the dynamics of microwave heated water and salt concentrations from 0.05 to 0.5 M. 2D simulations were developed using FemLab to model the electric field in the microwave for the initial heating. These models were found to be well correlated to the experimental results. Finally 3D experiments were performed in the cavity and found little variation in z-axis along the observable sections of the cavity. This could be explained by a broadening of the electric field at the sample position, caused by the presence of the chimney ports needed by the camera to observe the fluorescence response of the molecular temperature probes.

References:

1. Hill, J.M. and T.R. Marchant, *Modelling Microwave Heating.* Applied Mathematical Modelling, 1996. **20**(1): p. 3-15.
2. Zhao, H. and I.W. Turner, *The Use of a Coupled Computational Model for Studying the Microwave Heating of Wood.* Applied Mathematical Modelling, 2000. **24**(3): p. 183-197.
3. Ayappa, K.G., H.T. Davis, E.A. Davis, and J. Gordon, *Two-Dimensional Finite Element Analysis of Microwave Heating.* AIChE Journal, 1992. **38**(10): p. 1577-1592.
4. Ayappa, K.G., S. Brandon, J.J. Derby, H.T. Davis, and E.A. Davis, *Microwave Driven Convection in a Square Cavity.* AIChE Journal, 1994. **40**(7): p. 1268-1272.
5. English, N.J. and J.M.D. MacElroy, *Molecular Dynamics Simulations of Microwave Heating of Water.* Journal of Chemical Physics, 2003. **118**(4): p. 1589-1592.
6. Zasetsky, A.Y. and I.M. Svishchev, *Dielectric Response of Concentrated Nacl Aqueous Solutions: Molecular Dynamics Simulations.* Journal of Chemical Physics, 2001. **115**(3): p. 1448-1454.
7. Buchner, R., G.T. Hefter, and P.M. May, *Dielectric Relaxation of Aqueous Nacl Solutions.* Journal of Physical Chemistry A, 1999. **103**(1): p. 1-9.
8. Nortemann, K., J. Hilland, and U. Kaatze, *Dielectric Properties of Aqueous Nacl Solutions at Microwave Frequencies.* Journal of Physical Chemistry A, 1997. **101**(37): p. 6864-6869.
9. Stogryn, A. and G.J. Desargant, *The Dielectric-Properties of Brine in Sea Ice at Microwave-Frequencies.* Ieee Transactions on Antennas and Propagation, 1985. **33**(5): p. 523-532.
10. Stogryn, A., *Equations for Calculating the Dielectric Constant of Saline Water.* IEEE Transactions on Microwave Theory and Techniques, 1971. **MTT-19**: p. 733-736.
11. Wu, X., J.R. Thomas, and W.A. Davis, *Control of Thermal Runaway in Microwave Resonant Cavities.* Journal of Applied Physics, 2002. **92**(6): p. 3374-3380.
12. Ayappa, K.G., *Modelling Transport Processes During Microwave Heating: A Review.* Reviews in Chemical Engineering, 1997. **13**(2): p. 1-69.
13. Ratanadecho, P., K. Aoki, and M. Akahori, *A Numerical and Experimental Investigation of the Modeling of Microwave Heating for Liquid Layers Using a Rectangular Wave Guide (Effects of Natural Convection and Dielectric Properties).* Applied Mathematical Modelling, 2002. **26**(3): p. 449-472.
14. Zhao, H. and I.W. Turner, *An Analysis of the Finite-Difference Time-Domain Method for Modeling the Microwave Heating of Dielectric Materials within a Three-Dimensional Cavity System.* Journal of Microwave Power and Electromagnetic Energy, 1996. **31**(4): p. 199-214.
15. Liu, F., I. Turner, and M. Bialkowski, *A Finite-Difference Time-Domain Simulation of Power-Density Distribution in a Dielectric-Loaded Microwave Cavity.* Journal of Microwave Power and Electromagnetic Energy, 1994. **29**(3): p. 138-148.
16. Dibben, D.C. and A.C. Metaxas, *Finite Element Time Domain Analysis of Multimode Applicators Using Edge Elements.* Journal of Microwave Power and Electromagnetic Energy, 1994. **29**(4): p. 242-251.

Chapter 6: Concluding Remarks

6.1 Summary

Microwave heating technology has been established in the home and commercial food processing as a means of bringing rapid heating and precise power control to the preparation of food. However its use in other industries is negligible. Among the largest challenges facing the application of microwave heating to other industrial processes is an incomplete understanding of the temperature distributions formed in a microwave cavity. Most standard methods of temperature measurements, such as thermocouples, are incompatible with a microwave field, and additionally provide only single point information on temperature. Optical methods of temperature measurement show promise as a method of investigating the entire 3D temperature field in a microwave cavity.

In this work we have described the development of a 3D fluorescence thermometry instrument for making temperature measurements in a microwave heated sample. The instrument design is based on the ratiometric PLIF measurement of two molecular probes. Dextran labeled with Rhodamine B was used as a molecular temperature probe while Rhodamine 110 was used as a reference probe. The final temperature resolution of +/-1.6 °C (2 standard deviations, 95% confidence) with spatial resolutions of 0.2 mm in the x-y plane and 5 mm in the z plane were achieved in the test instrument.

A modified version of the test instrument was also constructed for use with a microwave cavity. Water and salt-water solutions were investigated through experimental measurements and 2D simulations. A high degree of correlation was found between the experiments and simulations of the microwave cavity for initial heating profiles. The dynamics of microwave heating at different salt concentrations in water were also observed. The presence of large apertures for optical observation is believed to elongate the electric field in the z-axis near the

sample, reducing z-axis variation. 3D experiments were performed for water and 0.1 M salt solutions and showed little variation in the observable z-axis of the microwave cavity.

This thesis has shown the successful application of 3D fluorescence-based measurement of temperature in a microwave heated sample. The experimental results were confirmed through calculations of the electric field in the microwave cavity. Experiments performed with this instrument coupled with more detailed simulations show great promise of increasing our understanding of the microwave heating process, which will lead to better utilization of microwave heating technology in the future.

6.2 Future Direction of Research

The bulk of work in this thesis was directed towards the design and implementation of the fluorescence thermometry instrument and only a small subset of the vast range of possible experiments in microwave heating was explored. In this thesis work we have studied the heating of salt-water solutions while varying the concentration of salt to modify the dielectric properties. The dielectric properties of the solution are only one part of microwave heating. The electric field distribution is another important factor and its distribution is tightly coupled with the cavity tuning and the dielectric properties. The microwave cavity in this work can be adjusted in a multitude of ways to affect the electric field, including cavity length, initial aperture size, and tuning by the 3-stub tuner. In addition, the sample cell could be modified to present a very different dielectric load to the microwave cavity. The work in this thesis has focused on the initial heating profiles and observations were made regarding the dynamics. A full understanding of the dynamics of the microwave heating process will require additions to the model including incorporation of material data on the temperature dependence of the dielectric properties of the sample and fully coupled electromagnetic and heat transfer equations in 2D and 3D.

Specific improvements to the instrument can help refine the results seen in this thesis as well as open new avenues to research. The temporal resolution of the system will be increased by adding computer control for operating the microwave generator and coupling this with the

camera trigger. This will ensure that all experiments start at the same moment and make more detailed examination of subtle changes in the flow field possible. In addition, recording of the reflected power from the microwave cavity will add more information into a simulation of the dynamics of microwave heating. The 3D procedure, as currently implemented, is a start towards a real-time 3D scanner. Future modifications should include enhancements to speed and automate 3D capture. There are many general improvements that can be made to the thermometry instrument including, but not limited to increasing accuracy, increasing precision, and increasing resolution. Finally, the design of a new microwave cavity with larger optical ports that still contain microwaves will greatly increase the flexibility of illuminating the sample and allow measurements of the entire 3D cross-section of the microwave cavity.

The ultimate goal of understanding microwave heating better is to enhance the safety of current applications of microwave heating and open doors to new applications. To do this, we need validated models of the microwave heating process to aid in the design of new microwave cavities and determine which applications show promise. The instrument developed in this thesis can provide the experimental data to validate models of microwave heating. However, in this thesis only a basic model of calculating the electric field for a static system is presented for simulating microwave heating. Future models should provide more in-depth understanding of microwave heating by calculating heat and mass transfer effects, such as conduction and convection, and coupling them with calculations of the electric field through Maxwell's equations. In addition to coupling these equations, future models should consider how material properties, such as viscosity and dielectric constants, vary with temperature and how that affects the simulation.